

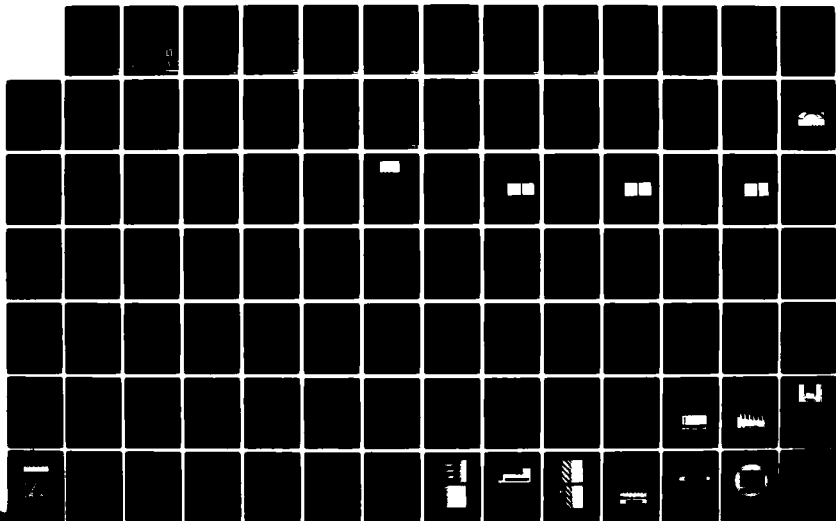
AD-A128 894

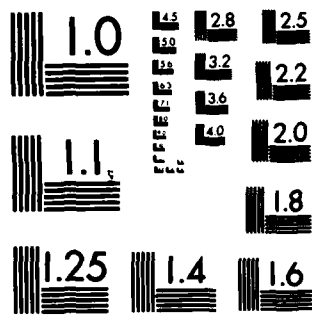
SOLID STATE RESEARCH(U) MASSACHUSETTS INST OF TECH
LEXINGTON LINCOLN LAB A L MCWHORTER 15 FEB 83 1983:1
ESD-TR-83-001 F19628-80-C-0002

1/2

UNCLASSIFIED

F/G 5/1 . NL

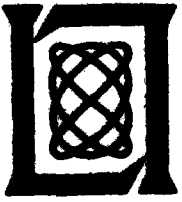




MICROCOPY RESOLUTION TEST CHART
NATIONAL BUREAU OF STANDARDS-1963-A

0

DA 128894

	1
<p style="text-align: center;">Solid State Research</p>	<p style="text-align: center;">1983</p>
<p style="text-align: center;">Prepared under Electronic Systems Division Contract F19628-80-C-0002 by</p> <p style="text-align: center;">Lincoln Laboratory</p> <p style="text-align: center;">MASSACHUSETTS INSTITUTE OF TECHNOLOGY</p> <p style="text-align: center;">LEXINGTON, MASSACHUSETTS</p>	

DTIC FILE COPY

Approved for public release; distribution unlimited.

DTIC
ELECTE
S JUN 6 1983
A

The work reported in this document was performed at Lincoln Laboratory, a center for research operated by Massachusetts Institute of Technology, with the support of the Department of the Air Force under Contract F19629-69-C-0002.

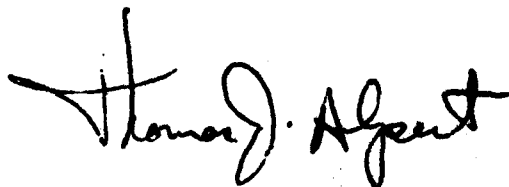
This report may be reproduced to satisfy needs of U.S. Government agencies.

The views and conclusions contained in this document are those of the contractor and should not be interpreted as necessarily representing the official policies, either expressed or implied, of the United States Government.

The Public Affairs Office has reviewed this report, and it is releasable to the National Technical Information Service, where it will be available to the general public, including foreign nationals.

This technical report has been reviewed and is approved for publication.

FOR THE COMMANDER



Thomas J. Alpert, Major, USAF
Chief, ESD Lincoln Laboratory Project Office

Non-Lincoln Recipients

PLEASE DO NOT RETURN

Permission is given to destroy this document
when it is no longer needed.

**MASSACHUSETTS INSTITUTE OF TECHNOLOGY
LINCOLN LABORATORY**

SOLID STATE RESEARCH

QUARTERLY TECHNICAL SUMMARY REPORT

1 NOVEMBER 1982 — 31 JANUARY 1983

ISSUED 22 APRIL 1983

Approved for public release; distribution unlimited.

LEXINGTON

MASSACHUSETTS

TABLE OF CONTENTS

Abstract	111
List of Illustrations	vii
List of Tables	xii
Summary	xiii
Reports on Solid State Research Organization	xvii xxiii
1. SOLID STATE DEVICE RESEARCH	1
1.1 New Developments in Mass-Transported GaInAsP/InP Buried-Heterostructure Lasers	1
1.2 Integrated Optics Wavefront Measurement Sensor	7
1.3 Three-Guide Optical Couplers in GaAs	11
2. QUANTUM ELECTRONICS	21
2.1 Search for New V^{2+} Hosts	21
2.2 Linewidth of (GaAl)As Diode Lasers with High-Reflectivity Coatings	23
2.3 Enhanced Raman Scattering from Small Si Structures	28
2.4 Surface Photoacoustic Wave Spectroscopy	31
2.5 Photodeposition of Ti and Application to Direct-Writing of Ti:LiNbO ₃ Waveguides	34
2.6 UV-Laser-Initiated Formation of Si ₃ N ₄	37
3. MATERIALS RESEARCH	43
3.1 Total-Dose Radiation Effects on SOI/CMOS Inverters Fabricated in Zone-Melting- Recrystallized Si Films	43
3.2 Double-Crystal X-Ray Diffractometry for Characterizing III-V Materials	48
3.3 Hole Traps in Tungsten-Doped GaAs Grown by Molecular-Beam Epitaxy	53

4. MICROELECTRONICS	59
4.1 Fabrication of Submicrometer-Size Structures in Si Using SiCl_4/O_2 Reactive-Ion Etching	59
4.2 The Effect of Chamber Configuration and Bias Voltage on Damage Induced in Si by Reactive-Ion Etching	63
4.3 High-Resolution Ion-Beam Lithography at Large Gaps Using Stencil Masks	67
4.4 Electron-Beam Programmable 128-kbit Wafer-Scale EPROM	75
4.5 Tunneling in Quantum-Well Structures	78
5. ANALOG DEVICE TECHNOLOGY	83
5.1 Superconductive Pulse Compressor	83
5.2 Superconductive Convolver	89

LIST OF ILLUSTRATIONS

<u>Fig. No.</u>		<u>Page</u>
1-1	Fabrication Procedure of GaInAsP/InP BH Laser with Deep Zn-Diffusion	2
1-2	SEM Photograph of a Stained Cross Section of BH After Deep Zn-Diffusion. In This Sample, Active Region Is 0.7 μm Wide.	3
1-3	L-I Characteristics of BH Lasers (a) Without and (b) with Deep Zn-Diffusion	4
1-4	Schematic Representation of Wavefront Measurement Sensor Illustrating Interferometer Array Coupled into a CCD Imager	6
1-5	Experimental Arrangement to Tilt Planar Wavefront and Maintain Its Position on LiNbO_3 Sample Containing Interferometer Under Test	8
1-6	Experimental Data Points $P_\phi / (P_1 + P_2)$, Normalized So That Maximum Value of Ratio Is Unity, Are Compared with Theoretical Curve $\cos^2(\phi/2)$. Phase Angle ϕ for Experimental Points Has Been Adjusted by a Constant for Each Interferometer for Best Fit.	9
1-7	(a) Photomicrograph of Cleaved Cross Section of GaAs Three-Guide Coupler. Sample Has Been Treated with a Stain/Etchant to Reveal $n^- - n^+$ Interface. Scale on Photomicrograph Is 1 $\mu\text{m}/\text{div}$. (b) Schematic Cross Section of Three-Guide Coupler with Rectangular Ribs of a Width Equal to Average Width (Same Cross-Sectional Area) of Actual Guides. Regions I and II Are Modeled as Slab Waveguides to Determine Effective Guide Index in Different Portions of n^- -Layer.	10
1-8	(a) Relative Output Power Out of Each Guide as a Function of Length for a Three-Guide Coupler with Input Power into Center Guide. (b) Outputs Obtained on Oscilloscope and TV Monitor for a Length of 3.2 mm.	12
1-9	(a) Relative Output Power Out of Each Guide as a Function of Length for a Three-Guide Coupler with Input Power into One of Outside Guides. (b) Outputs Obtained on Oscilloscope and TV Monitor for a Length of 6.5 mm.	14

<u>Fig. No.</u>		<u>Page</u>
1-10	(a) Relative Output Power of Each Guide as a Function of Length for a Two-Guide Coupler. (b) Outputs Obtained on Oscilloscope and TV Monitor for a Length of 4.9 mm.	16
2-1	${}^4T_2 \rightarrow {}^4A_2$ Fluorescence Lifetime Vs Temperature in Three Different Host Crystals	22
2-2	Spectrum of ${}^4T_2 \rightarrow {}^4A_2$ Fluorescence from V:KMgF ₃ at 300 K	24
2-3	Single-Sided Output Power Vs Injection Current for CSP-(GaAl)As Diode Laser Before and After High-Reflectivity Coating Was Applied	25
2-4	Laser Linewidth as a Function of Inverse Output Power Before and After High-Reflectivity Coating Was Applied	26
2-5	Elastic Scattering Efficiency Factor Q_{sca} and Absorption Efficiency Factor Q_{abs} as a Function of Sphere Diameter for Light of Wavelength 0.488 μm Incident on Si Spheres (Refractive Index $n = 4.2 - 0.053i$)	30
2-6	Surface Photoacoustic Spectrum of an Approximately Monolayer Thick Rhodamine 590 Dye Film on a Crystal Quartz Substrate	32
2-7	SAW Signal Vs Time for a Rhodamine 590 Dye Film on a Quartz Substrate. Decay Is Due to Laser-Induced Desorption. Energy Density Was 0.1 J/cm ² at 520 nm, and Pulse Repetition Rate Was 10 Hz.	33
2-8	Nomarski Optical Micrograph of a Photodeposited Waveguide in LiNbO ₃ After Indiffusion. Small-Scale Divisions Are Separated by 2 μm .	36
3-1	Schematic Structure of SOI/CMOS Inverter Fabricated in Zone-Melting-Recrystallized Si Film on SiO ₂ -Coated Si Substrate	45
3-2	Subthreshold Characteristics of n- and p-Channel Devices Biased with $V_{IN} = 0$ V and $V_B = -5$ V Before and After Irradiation of SOI/CMOS Inverters	46
3-3	Subthreshold Characteristics of n- and p-Channel Devices with $V_{IN} = 5$ V and $V_B = -5$ V Before and After Irradiation	46

<u>Fig. No.</u>		<u>Page</u>
3-4	Threshold Voltage of n- and p-Channel Devices as a Function of Ionizing Dose	47
3-5	Rocking Curves for CuK (400) Peak Obtained by Double-Crystal Diffractometry for an InP Crystal Before and After Thermal Annealing	49
3-6	Rocking Curve for CuK (400) Peak Obtained by Double-Crystal Diffractometry for a Sample Prepared by LPE Growth of a GaInAsP Layer on an InP Substrate	50
3-7	CuK ₁ and CuK ₂ (600) Peaks Obtained by Single-Crystal Diffractometry for GaInAsP/InP Sample of Fig. 3-6	52
3-8	Transient Capacitance Vs Temperature Spectra Taken for MBE GaAs Layers with Emission Time of 21.7 ms. (a) DLTS Trace for Control Sample, Showing Electron Traps; (b) Optical DLTS Traces, Showing Mainly Hole Traps.	54
3-9	Reciprocal of Electron Mobility at 77 K as a Function of Hole Trap Density for MBE GaAs Layers	56
4-1	3200-Å-Period Grating Reactive Ion Etched in 1:1 SiCl ₄ /O ₂	59
4-2	Al-Masked, 3200-Å-Period Grating Reactive Ion Etched in 1:1 SiCl ₄ /O ₂ . Redeposition on Al Mask Caused Widening of Base. Etched Surface Is Clean and Smooth.	60
4-3	2-μm-Wide Line Reactive Ion Etched in 1:1 SiCl ₄ /O ₂ . SiO ₂ Layer and Al Mask Still Intact.	61
4-4	3200-Å-Period Grating Reactive Ion Etched in 1:1 SiCl ₄ /O ₂ with Cr Mask on 1500-Å SiO ₂ on n ⁺ -Type Si. Cr Mask Is Gone, and SiO ₂ Layer Is Rounded at Edges.	62
4-5	4-μm-Period Grating Reactive Ion Etched in 1:1 SiCl ₄ /O ₂ with SiO ₂ Mask on 1500-Å SiO ₂ on ~1-μm n ⁺ -on-n-type Si. Undercut of n ⁺ Layer Occurs.	62
4-6	(a) Schematic Diagram of Reactive-Ion Etching Chamber Which Consists of Stainless Steel with a Quartz Plate on Powered Electrode (20-cm Diameter). (b) Powered Electrode Covered by Si and Reduced to 10-cm Diameter by Placing a Grounded Aluminum Annulus on Top.	64

<u>Fig. No.</u>		<u>Page</u>
4-7	Number of Interface States Induced as a Function of Etching Voltage in CF_4 , SiF_4 , and $SiCl_4$	65
4-8	Low-Frequency C-V Curves Showing Difference in Interface-State Generation for Samples Etched in a Stainless-Steel Chamber and in a Coated Chamber. Samples Were Etched in CF_4 at 600 V.	66
4-9	Schematic Illustration of a Section of a Si_3N_4 - SiO_2 - Si_3N_4 (N-O-N) Ion Lithography Stencil Mask	68
4-10	SEM Micrographs of 320-nm-Period Grating Etched by RIE into Ion Lithography Stencil Mask Materials: (a) a SiN Structure Produced by CF_4 RIE, (b) an N-O-N Structure Produced by CHF_3 RIE	69
4-11	SEM Micrograph of a Cleaved Section of a Completed N-O-N Stencil Mask. Mask Is 1 μm Thick, Period of Grating Is 320 nm, and Period of Support Structure Is 12 μm .	70
4-12	SEM Micrographs of PMMA Structures Resulting from 100-keV Proton Exposures Through a SiN Stencil Mask at a Dose of $3 \times 10^{13} H^+/cm^2$: (a) at a 25- μm and (b) at a 275- μm Mask-to-Sample Gap	71
4-13	SEM Micrograph of a PMMA Structure Where PMMA Has Acted as a Negative Resist. Exposure Was Done with 100-keV Protons Through a SiN Stencil Mask at a Dose of $5 \times 10^{14} H^+/cm^2$.	72
4-14	SEM Micrograph of a Double Exposure Through Type of Mask Depicted in Fig. 4-9. Exposures Were Done at 100 keV at a Dose of $3 \times 10^{13} H^+/cm^2$ with an ≈ 60 - μm Gap Between Mask and Substrate. Between Exposures, Mask and Sample Remained Clamped While They Were Tilted 6° with Respect to Ion Beam in a Direction Parallel to 320-nm-Period Grating.	73
4-15	A 128-kbit EBPRAM. Eight Rows in Center of Wafer Are 16K Modules. Each 16K Module Consists of Sixteen 1K Subsystems Which Are Interconnected by Metal Lines Running Across Wafer. Bonding Pads Are Located on Left Edge of Memory Array. Test Chips Surround Memory System.	74
4-16	Block Diagram of 1-kbit Subsystem. A 10-Bit Address Provides Row (R_0 to R_4) and Column (C_0 to C_4) Selection. Each Row or Column Selector, Shown as a Rectangular Box, Contains 5 Programmable Links. Output of Memory, if Enabled by Chip Select, Can Pull a Wafer-Scale Output Bus to Ground.	76

<u>Fig. No.</u>		<u>Page</u>
4-17	Computed Conversion Efficiency of a Quantum-Well Structure as a Function of Bias Voltage. Local Oscillator Frequency Is 5 THz at a Power of 10 μ W. Note Spikes Which Are Separated in Voltage Corresponding to Photon Steps $h\nu/e$.	79
5-1	Chirp Filter Formed by Cascading Backward-Wave Couplers	83
5-2	Photograph of a Superconductive Tapped Delay Line Just Prior to Final Assembly	84
5-3	Pulse Expansion and Compression with Superconductive Tapped Delay Line of Fig. 5-2. (a) Upper Trace: Expanded Down-Chirp Pulse; Lower Trace: Compressed Pulse Output of Up-Chirp End of Device After Application of Expanded Pulse. (b) Enlarged View of Compressed Pulse Output, Clearly Demonstrating 2.6-GHz Bandwidth.	86
5-4	(a) Predicted and Measured Amplitude Response of Tapped Delay Line of Fig. 5-2. (b) Predicted and Measured Deviations from Quadratic Phase for This Device.	88
5-5	Measured and Predicted Compressed-Pulse Response Envelopes, Obtained by Multiplying Up- and Down-Chirp Frequency Responses and Fourier Transforming	89
5-6	Schematic of a Superconductive Convolver	90
5-7	Output of Superconductive Convolver. (a) Upper Traces: Envelopes of Gated-CW Input Pulses; Lowest Trace: Real-Time Output, Horizontal Scale 20 ns/div. (b) Output Envelope After Signal Averaging, Horizontal Scale 10 ns/div.	91
5-8	Output Power of Convolver as a Function of Signal Level	93

LIST OF TABLES

<u>Table No.</u>		<u>Page</u>
2-1	Properties of Laser-Deposited Si_3N_4 Films as a Function of Substrate Temperature and $\text{SiH}_4:\text{NH}_3$ Ratio	38
3-1	Growth Conditions and Mobilities for MBE GaAs Layers	55
5-1	Convolver Parameters	94

SUMMARY

1. SOLID STATE DEVICE RESEARCH

GaInAsP/InP buried-heterostructure lasers formed by thermally transported InP have resulted in low threshold, high efficiency, and high device yield. Zinc diffusion has been utilized to improve the light-current linearity and reduce the threshold temperature dependence.

Experimental results have been obtained which demonstrate the feasibility of using an integrated-optics array of Mach-Zehnder dielectric-waveguide interferometers to measure the phase and amplitude across an optical wavefront. The excellent agreement between experiment and theory over a number of interferometers suggests that accuracy of the wavefront measurement sensor is limited only by signal statistics and noise considerations.

Three-guide optical couplers consisting of slab-coupled rib-type guides have been fabricated on GaAs. Their behavior closely approximates that predicted using an effective-index analytic method. Couplers of this type should prove useful as replacements for "Y"-type power dividers and combiners, especially in cases where waveguide bends would result in unacceptable losses.

2. QUANTUM ELECTRONICS

Crystals of V:KMgF₃ have been grown in a search for new V²⁺ laser systems. The fluorescence properties indicate that room-temperature operation of a tunable, 1- μ m wavelength V:KMgF₃ laser may be possible.

A high-reflectivity coating has been applied to the rear facet of a single-frequency diode laser in order to further test a recently developed theory of linewidth broadening. The experimental dependence of linewidth on reflectivity for constant output power is in agreement with theory, assuming that the contribution from refractive index fluctuations does not vary.

Enhanced Raman scattering intensities have been observed from a variety of Si structures having submicrometer dimensions. Calculations suggest that the enhancement is due to electromagnetic structure resonances.

Surface photoacoustic wave spectroscopy, a new technique for measuring the optical absorption spectra of thin films, has been demonstrated to have submonolayer sensitivities. Both absorption spectra and laser desorption cross sections have been measured.

Ti films have been deposited by laser photodeposition on LiNbO_3 to form, after diffusion, 4- μm -wide single-mode channel waveguides of comparable quality to conventionally fabricated Ti-indiffused guides. The technique introduces new design flexibility into waveguide fabrication, permitting controlled gradations in the diffused index change and the lateral width along the guide.

Si_3N_4 films have been deposited on Si by using 193-nm ArF excimer laser radiation to initiate the reaction of SiH_4 and NH_3 at substrate temperatures between 200° to 600°C. These films are stoichiometric, and their physical and optical properties are comparable with those produced using low-pressure chemical-vapor deposition.

3. MATERIALS RESEARCH

The effects of ionizing radiation on SOI/CMOS devices fabricated in zone-melting-recrystallized Si films on SiO_2 -coated Si substrates have been studied as a function of the negative bias applied to the substrates during irradiation and measurement. Best results were obtained with a substrate bias of -5 V, which greatly increases the radiation hardness of n-channel devices without significantly impairing the operation of p-channel devices.

Rocking curve measurements made with a double-crystal x-ray diffractometer are being used to characterize III-V compounds and alloys. These measurements have shown that the present procedure for preparing InP substrates results in severe surface damage, which can be removed by thermal annealing. The minimum lattice mismatch between an epilayer and its substrate (e.g., GaInAsP on InP) that can be detected by the double-crystal

technique is about 0.01 percent, compared with several tenths of a percent for conventional single-crystal diffractometry.

As a first step in determining whether the performance of permeable-base transistors is being degraded by W doping of the GaAs epilayer grown over the W base grid, a study has been made of the electrical properties of GaAs films grown by molecular-beam epitaxy in the presence of a W flux produced by evaporation from a heated filament. Optical deep-level transient capacitance measurements on three such films have shown that they contain much higher concentrations of two different hole traps than an undoped film, although these concentrations are not completely correlated with filament temperature.

4. MICROELECTRONICS

Submicrometer-size structures have been reactive-ion etched in Si with SiCl_4/O_2 gas mixtures. Selective redeposition of Si-O-Al material on Al used as an etch mask gives enhanced masking capabilities. Problems caused by mask widening due to redeposition and by variations in the etch rates of n^+ - and n -type Si have been encountered.

Surface damage in Si substrates created by reactive-ion etching with CF_4 , CHF_3 , Cl_2 , SiCl_4 , or SiF_4 has been investigated. Interface states generated by these dry-etching processes were strongly dependent on the etching gas and the bias voltage, and carbon-based gases (CF_4 and CHF_3) induced more interface states than those without carbon. A significant amount of damage was found to originate from nonvolatile compounds sputtered from the walls of the vacuum chamber during etching.

High-resolution, masked, ion-beam lithography (MIBL) has been demonstrated at large mask-to-sample gaps using two types of membrane stencil masks - a single-layer, Si-rich silicon nitride (SiN) membrane, and a Si_3N_4 - SiO_2 - Si_3N_4 sandwich structure membrane. Lines and spaces of 160 nm have been exposed in 0.5- μm PMMA at gaps as large as 275 μm using 100-keV protons. The results suggest that MIBL can be an extremely high-resolution proximity printing technique.

The feasibility of using an electron beam to customize and repair a wafer-scale nMOS system has been demonstrated. A 128-kbit read-only memory which uses electron-beam programmable floating-gate links for data bits and address decodes was fabricated as a test vehicle. Because of the small link size, high programming speed, absence of debris, and ability to program without disturbing the integrity of the passivation, the electron-beam programmable links may provide an attractive alternative to laser or fusible-link repair and customization techniques.

Quantum-well structures have been analyzed theoretically to evaluate their response to far-infrared illumination. They are predicted to be sensitive detectors and mixers at these high frequencies.

5. ANALOG DEVICE TECHNOLOGY

By using tapped superconductive striplines, linear-frequency-modulated dispersive delay lines (chirp filters) having a bandwidth of 2.6 GHz centered at 4 GHz and a dispersion time of 35 ns have been constructed. Measured characteristics closely match the predictions of a theoretical model.

The operation of a superconductive convolver has been tested at 3 GHz by obtaining a triangular convolution output envelope for rectangular signal and reference input envelopes. The preliminary convolver lacks sufficient dynamic range because of both low mixer saturation and undesired mixer products, but this limitation will be removed by use of multiple-junction rings as balanced mixing elements.

REPORTS ON SOLID STATE RESEARCH

15 November 1982 through 15 February 1983

PUBLISHED REPORTS

Journal Articles

<u>JA No.</u>			
5059	Stoichiometric Lasers	S.R. Chinn	In CRC Handbook of Laser Science and Technology, Volume I. Lasers and Masers, M.J. Weber, Ed. (CRC Press, Boca Raton, Florida, 1982), pp. 147-169
5124	Paramagnetic Ion Lasers	P.F. Moulton	In CRC Handbook of Laser Science and Technology, Volume I. Lasers and Masers, M.J. Weber, Ed. (CRC Press, Boca Raton, Florida, 1982), pp. 21-146
5267	Laser Microchemistry - Local Nucleation Mechanisms for Photodeposition	D.J. Ehrlich R.H. Osgood, Jr.	Thin Solid Films <u>90</u> , 287 (1982)
5321	Fabrication of Through-Wafer Via Conductors in Si by Laser Photochemical Processing	D.J. Ehrlich D.J. Silversmith R.W. Mountain J. Tsao	IEEE Trans. Components, Hybrids, and Manufacturing Technology <u>CHMT-5</u> , 520 (1982)
5363	Wide-Band Monolithic Acoustoelectric Memory Correlators	R.A. Becker R.W. Ralston P.V. Wright	IEEE Trans. Sonics Ultrason. <u>SU-29</u> , 289 (1982)
5365	Simultaneous Formation of a Shallow Silicon p-n Junction and a Shallow Silicide/Silicon Ohmic Contact by an Ion Implantation Technique	B-Y. Tsaur C.H. Anderson	Appl. Phys. Lett. <u>41</u> , 877 (1982)
5367	Zone-Melting Recrystallization of Si Films with a Moveable-Strip-Heater Oven	M.W. Geis H.I. Smith* B-Y. Tsaur J.C.C. Fan D.J. Silversmith R.W. Mountain	J. Electrochem. Soc. <u>129</u> , 2812 (1982)
5390	Transmission Electron Microscopy of GaAs Grown over Submicrometer-Period Tungsten Gratings	B.A. Vojak J.P. Salerno	Appl. Phys. Lett. <u>41</u> , 1151 (1982)
5407	SOI/CMOS Circuits Fabricated in Zone-Melting-Recrystallized Si Films on SiO ₂ -Coated Si Substrates	B-Y. Tsaur J.C.C. Fan R.L. Chapman M.W. Geis D.J. Silversmith R.W. Mountain	IEEE Electron Device Lett. <u>EDL-3</u> , 398 (1982)

*Author not at Lincoln Laboratory.

JA No.

- | | | | |
|------|---------------------------------------------------------------------------------------------------------|--------------------------------------------|----------------------------------------------------------|
| 5413 | Amplified Surface Plasma Wave Scattering: A New Mechanism for the Generation of Surface Microstructures | D.J. Ehrlich
S.R.J. Brueck
J.Y. Tsao | AIP Physics News in 1982, P.F. Schewe, Ed. (1982), p. 87 |
| 5414 | Titanium-Doped Sapphire: A New Tunable Solid State Laser | P.F. Moulton | AIP Physics News in 1982, P.F. Schewe, Ed. (1982), p. 89 |
| 5430 | Low-Loss LiNbO ₃ Waveguide Bends with Coherent Coupling | L.M. Johnson
F.J. Leonberger | Opt. Lett. <u>8</u> , 111 (1983) |

Meeting Speeches

MS No.

- | | | | |
|-------|------------------------------------------------------------------------------------------------------|------------------------------------------------------------------------------------------------------------------------------------------------------------------------------------------------------------------------|---------------------------------------------------------------------------------------------------------------------------------------|
| 5609B | Advances in Divalent Transition-Metal Lasers | P.F. Moulton | <u>Proceedings of the International Conference on Lasers '81</u> , edited by C.B. Collins (STS Press, McLean, Virginia, 1981), p. 359 |
| 5806 | Some Surprising Results in Studies of Transition-Metal-Doped Crystals | P.F. Moulton | <u>Proceedings of the International Conference on Lasers '81</u> , edited by C.B. Collins (STS Press, McLean, Virginia, 1981), p. 789 |
| 5883A | Performance Characteristics of a 4-Bit 828-Megasamples/sec Electro-Optic Analog-to-Digital Converter | F.J. Leonberger
R.A. Becker | <u>Future Trends in Fiber Optic Communications</u> , C.W. Kleekamp, Ed., Proc. SPIE <u>340</u> , 66 (1982) |
| 6017 | Millimeter-Wavelength GaAs Permeable Base Transistors | G.D. Alley
C.O. Boxler
N.P. Economou
D.C. Flanders
M.W. Geis
G.A. Lincoln
W.T. Lindley
R.W. McClelland
R.A. Murphy
K.B. Nichols
W.J. Piacentini
S. Rabe
J.P. Salerno
B.A. Vojak | IEEE Trans. Electron Devices <u>ED-29</u> , 1708 (1982) |
| 6028 | High-Speed, Single Chip Signal Processing Devices for Radar and Sonar | A.M. Chiang
C.M. Rader | Digest of Papers, Government Microcircuit Applications Conf., Orlando, Florida, 2-4 November 1982, p. 222 |
| 6065 | Fabrication of GaAs CCDs for High-Speed Spatial Light Modulators | B.E. Burke
K.B. Nichols
J.T. Kelliher
R.A. Murphy | Proc. GaAs IC '82 Symp., New Orleans, Louisiana, 9-11 November 1982, p. 45 |

MS No.

6107	The Microwave Silicon Permeable Base Transistor	D.D. Rathman N.F. Economou D.J. Silversmith R.W. Mountain S.M. Cabral	Proc. Intl. Electron Devices Mtg., San Francisco, 13-15 December 1982, p. 650
------	-------------------------------------------------	-----------------------------------------------------------------------------------	-------------------------------------------------------------------------------

* * * * *

UNPUBLISHED REPORTS

Journal Articles

JA No.

5381	Reflectometric Spectroscopy of Adsorbed Molecular Layers	V. Daneu D.J. Ehrlich R.M. Osgood*	Accepted by Opt. Lett.
5396	High Resolution Ion Beam Lithography at Large Gaps Using Stencil Masks	J.N. Randall D.C. Flanders N.F. Economou J.P. Donnelly E.I. Browley	Accepted by Appl. Phys. Lett.
5402	Solidification-Front Modulation to Entrain Subboundaries in Zone-Melting Recrystallisation of Si on SiO ₂	M.W. Geis H.I. Smith* D.J. Silversmith R.W. Mountain	Accepted by J. Electrochem. Soc.
5403	Experimental Comparison of Heterodyne and Direct Detection Pulsed Differential Absorption CO ₂ LIDAR	D.K. Killinger N. Manyuk W.E. DeFeo	Accepted by Appl. Opt.
5405	Transmission Electron Microscopy of GaAs Permeable Base Transistor Structures Grown by Vapor Phase Epitaxy	B.A. Vojak J.P. Salerno D.C. Flanders G.D. Alley C.O. Bosler K.B. Nichols R.W. McClelland N.F. Economou G.A. Lincoln R.A. Murphy W.E. Lindley G.D. Johnson	Accepted by J. Appl. Phys.
5412	A Slow Selective Etch for GaInAsP Grown on InP	G.A. Ferrante J.P. Donnelly C.A. Armiento	Accepted by J. Electrochem. Soc.
5426	Photodeposition of Ti and Application to Direct-Writing of Ti:LiNbO ₃ Waveguides	J.Y. Tsao R.A. Becker D.J. Ehrlich F.J. Leonberger	Accepted by Appl. Phys. Lett.
5431	Broadband Guided-Wave Optical Frequency Translator using an Electro-Optical Bragg Array	R.H. Kingston R.A. Becker F.J. Leonberger	Accepted by Appl. Phys. Lett.
5435	Developing a Technology Base for Advanced Devices and Circuits	N.F. Economou	Accepted by Proc. IEEE

*Author not at Lincoln Laboratory.

JA No.

5439	Integrated Optics Wavefront Measurement Sensor	R.H. Rediker T.A. Lind F.J. Leonberger	Accepted by Appl. Phys. Lett.
5443	Submicrometer Periodicity Gratings as Artificial Anisotropic Dielectrics	D.C. Flanders	Accepted by Appl. Phys. Lett.
5447	An Investigation of GaAs Films Grown by MBE at Low Substrate Temperatures and Growth Rates	G.H. Metz A.R. Calawa J.G. Navroides	Accepted by J. Vac. Sci. Technol.
5448	Monolithic Circuits for Millimeter-Wave Systems	A. Chu W.E. Courtney L.J. Mahoney	Accepted by Microwave J.
5463	Integrated Optics: A New Textbook and Thoughts on Future Directions	F.J. Leonberger	Accepted by Laser Focus

Meeting Speeches*

MS No.

5626A	Growth of Laser-Quality MgF ₂ Crystals Doped with W, Co, or V	R.R. Fahey P.F. Moulton	American Association for Crystal Growth, Lexington, Massachusetts, 8 December 1982
6007B	Electrooptical Devices for GHz Sampling and A/D Conversion	F.J. Leonberger	Seminar, Johns Hopkins University, Baltimore, Maryland, 4 November 1982
6012	Solar Photovoltaic Cells	J.C.C. Fan	First U.S.-China Conf. of Energy Resources and Environment, Beijing (Peking) People's Republic of China, 7-12 November 1982
6060	Superconductive Convolver	S.A. Reible A.C. Anderson P.V. Wright R.S. Withers R.W. Ralston	1982 Applied Superconductivity Conf., Knoxville, Tennessee, 30 November - 3 December 1982
6061	Superconductive Tapped Delay Lines for Microwave Analog Signal Processing	R.S. Withers A.C. Anderson P.V. Wright S.A. Reible	
6063	Substrates for Superconductive Analog Signal Processing Devices	A.C. Anderson R.S. Withers S.A. Reible	
6073	Electronic Properties of Grain Boundaries in GaAs: A Study of Oriented Bicrystals Prepared by Epitaxial Lateral Overgrowth	J.P. Salerno R.W. McClelland J.C. Navroides J.C.C. Fan A.F. Witt†	Materials Research Society Annual Mtg., Boston, 1-4 November 1982

*Titles of Meeting Speeches are listed for information only. No copies are available for distribution.

†Author not at Lincoln Laboratory.

MS No.

6076	Electrical Characteristics of Zone-Melting-Recrystallized Si Films on Insulators	B-Y. Teaur J.C.C. Fan M.W. Geis R.L. Chapman S.R.J. Brueck D.J. Silvermith R.W. Mountain	
6077	Ion Implantation Technique for Simultaneous Formation of Shallow Silicon p-n Junction and Shallow Silicide/Silicon Ohmic Contact	B-Y. Teaur C.H. Anderson	Materials Research Society Annual Mtg., Boston, 1-4 November 1982
6082	Zone Melting Recrystallization of Semiconductor Films	M.W. Geis M.I. Smith* B-Y. Teaur J.C.C. Fan D.J. Silvermith R.W. Mountain R.L. Chapman	
6090	Laser-Induced Fluorescence Diagnostics of CF_4/O_2 Plasma Etching	S. Pang S.R.J. Brueck	
6111	Advances in Tunable Transition-Metal Lasers	P.F. Moulton	Lasers '82 Conf., New Orleans, Louisiana, 13-17 December 1982
6147A	Spectral Properties of Tunable Lasers	A. Mooradian	XI Intl. Conf. on Laser and Nonlinear Optics, Yerevan, USSR, 22-25 November 1982
6150	Direct-Write Laser Fabrication	R.N. Osgood* D.J. Ehrlich T.F. Deutsch D.J. Silvermith A. Sanchez	To be published in Proc. NATO ARI, Microelectronics - Structures and Complexity Conf., Les Deux Alpes, France, 15-19 March 1982
6166	Comparison of Heterodyne and Direct Detection CO_2 DIAL Measurements	D.K. Killinger M. Menyuk W.E. DeFeo	OSA Topical Mtg. on Optical Techniques for Remote Probing of the Atmosphere, Lake Tahoe, California, 10-12 January 1983
6177	Effects of Differential-Reflectivity, Background Interference, and Signal Fluctuations on IR DIAL Measurement Accuracy	M. Menyuk D.K. Killinger	
6209	Laser Probing of Semiconductor Materials and Device Structures	S.R.J. Brueck	IEEE Quantum Electronics and Application Society Seminar, Waltham, Massachusetts, 18 January 1983
6214	A Precision Wide-Range Optical Gap Measurement Technique	D.C. Flanders T.N. Lyaszars	Workshop on Micrometer and Submicrometer Lithography, Palm Springs, California, 19-21 January 1983
6242	Spectral Properties of Semiconductor Diode Lasers	A. Mooradian	13th Winter Colloq. on Quantum Electronics, Snowbird, Utah, 12-14 January 1983

*Author not at Lincoln Laboratory.

ORGANIZATION

SOLID STATE DIVISION

A.L. McWhorter, Head
I. Melngailis, Associate Head
J.F. Goodwin, Assistant

P.E. Tannenwald, Senior Staff

QUANTUM ELECTRONICS

A. Mooradian, Leader
P.L. Kelley, Associate Leader

Barch, W.E.	Johnson, B.C.*
Belanger, L.J.	Killinger, D.K.
Brueck, S.R.J.	Lenth, W.
Burke, J.W.	Lovold, S.H.G.
Bushee, J.F., Jr.	Menyuk, N.
DeFeo, W.E.	Moulton, P.F.
Deutsch, T.F.	Murphy, D.V.
Ehrlich, D.J.	Sedlacek, J.H.C.
Feldman, B.	Sharpe, K.A.
Force, A.	Sullivan, D.J.
Hancock, R.C.	Tsao, J.Y.
Harrison, J.*	

ELECTRONIC MATERIALS

A.J. Strauss, Leader
J.C.C. Fan, Assistant Leader
J.G. Mavroides, Senior Staff
H.J. Zeiger, Senior Staff

Anderson, C.H., Jr.	Kolesar, D.F.
Branz, H.M.*	Krohn, L., Jr.
Button, M.J.	Mastromattei, E.L.
Chapman, R.L.	Metze, G.M.
Chen, C.K.	Nitishin, P.M.
Connors, M.K.	Palm, B.J.
Davis, F.M.	Pantano, J.V.
Delaney, E.J.	Tracy, D.M.
Fahey, R.E.	Tsaur, B-Y.
Finn, M.C.	Turner, G.W.
Gale, R.P.	Vohl, P.
Iseler, G.W.	Windhorn, T.H.
King, B.D.	

APPLIED PHYSICS

R.C. Williamson, Leader
F.J. Leonberger, Assistant Leader
T.C. Harman, Senior Staff
R.H. Kingston, Senior Staff
R.H. Rediker, Senior Staff

Armiento, C.A.*	Groves, S.H.	Paladino, A.E.
Becker, R.A.	Hakimi, F.*	Plonko, M.C.
Carter, F.B.	Hovey, D.L.	Schloss, R.P.*
Chinnock, C.B.	Johnson, L.M.	Spears, D.L.
Cox, C.H. III	Liau, Z.L.	Tsang, D.Z.
DeMeo, N.L., Jr.	Lind, T.A.	Walpole, J.N.
Diadiuk, V.	McBride, W.F.	Whitaker, N.*
Donnelly, J.P.	Molter-Orr, L.*	Woodhouse, J.D.
Ferrante, G.A.	O'Donnell, F.J.	Yap, D.*

* Research Assistant

ANALOG DEVICE TECHNOLOGY

E. Stern, Leader
J.H. Cafarella, Assistant Leader
R.W. Ralston, Assistant Leader

Anderson, A.C.	Gottschalk, P.G.†	Melngailis, J.§
Arsenault, D.R.	Green, J.B.	Oates, D.E.
Behrmann, G.J.	Hauser, E.M.	Reible, S.A.
Bouman, C.A.	Holtham, J.H.	Sage, J.P.
Brogan, W.T.	Kernan, W.C.	Slattery, R.L.
Dolat, V.S.	Lattes, A.L.	Withers, R.S.
Fischer, J.H.	Leung, I.	Yao, I.
Fitch, G.L.*	Macedo, E.M., Jr.	
Flynn, G.T.	Macropoulos, W.	

MICROELECTRONICS

W.T. Lindley, Leader
F.J. Bachner, Associate Leader
N.P. Economou, Assistant Leader
R.A. Murphy, Assistant Leader

Bozler, C.O.	Gatley, J.S.*	Parker, C.D.
Bromley, E.I.	Geis, M.W.	Peck, D.D.
Burke, B.E.	Goodhue, W.D.	Piacentini, W.J.
Cabral, S.M.	Gray, R.V.	Pichler, H.H.
Calawa, A.R.	Lax, B.§	Rabe, S.
Chen, C.L.	Lincoln, G.A., Jr.	Randall, J.N.
Chiang, A.M.	Lyszczarz, T.M.	Rathman, D.D.
Chu, A.	Mahoney, L.J.	Reinold, J.H., Jr.*
Clifton, B.J.	Manfra, M.J.	Shaver, D.C.
Daniels, P.J.	McClelland, R.W.	Silversmith, D.J.
DeGraff, P.D.	McGonagle, W.H.	Smythe, D.L., Jr.
Durant, G.L.	Mountain, R.W.	Sollner, T.C.L.G.
Efremow, N.N., Jr.	Mroczkowski, I.H.	Vojak, B.A.
Felton, B.J.	Nichols, K.B.	Wilde, R.E.
Flanders, D.C.	Pang, S.W.	

* Co-op Student

† Research Assistant

§ Part Time

1. SOLID STATE DEVICE RESEARCH

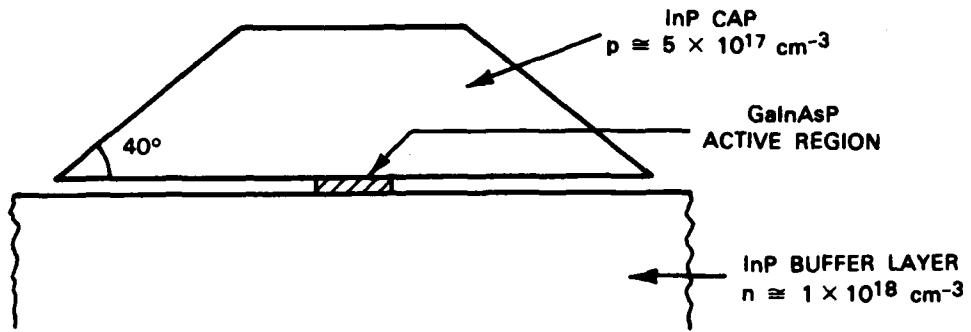
1.1 NEW DEVELOPMENTS IN MASS-TRANSPORTED GaInAsP/InP BURIED-HETEROSTRUCTURE LASERS

As a potentially very important class of sources in fiber optical communication and integrated optics, GaInAsP/InP buried-heterostructure (BH) lasers have received much attention in recent years. By using liquid-phase epitaxial (LPE) regrowth techniques^{1,2} or LPE growth on grooved substrates,³⁻⁶ many groups of researchers have obtained BH lasers with excellent characteristics, such as low-threshold, high efficiency, high power operation, and high device yield. In a recent publication,⁷ we reported promising preliminary results of a new BH laser in which thermally transported InP was used to form the burying sidewalls. This technique is simpler than the previously used techniques, and it opens up new possibilities for integrated optoelectronic devices. In this section we report further development of the technique which has resulted in thresholds as low as 5.5 mA and device yields as high as 80 percent. In addition, Zn diffusion has been performed after the transport of InP and has resulted in improved linearity of the light-current characteristics and a T_0 of 81 K.

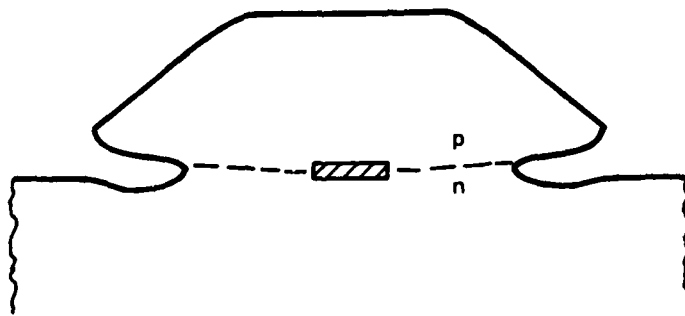
The fabrication procedure illustrated in Fig. 1-1 is essentially the same as described earlier⁷; only the new developments will be detailed in this report. Lasers parallel to either (011) or (0 $\bar{1}\bar{1}$) planes have been fabricated. Except for Wafer 513, lasers reported here are parallel to (011) planes. To form the structure shown in Fig. 1-1(a), two narrow stripes were etched to form a mesa for the laser with large unetched supporting mesas (not shown in Fig. 1-1) on each side. The supporting mesas served to mechanically protect the laser mesas. Improved dimensional control of the quaternary active region width has been achieved with yet another kind of mesa which was 1.5 μm narrower than, but otherwise identical to, the laser mesas. The quaternary etching was terminated when these mesas were completely etched through. By using this technique, GaInAsP active regions 0.5 to 2.5 μm in

(a) SELECTIVE CHEMICAL ETCHING

124820-N



(b) TRANSPORT OF InP



(c) Zn DIFFUSION

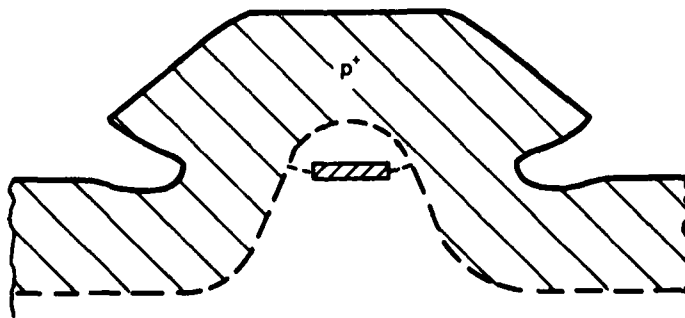


Fig. 1-1. Fabrication procedure of GaInAsP/InP BH laser with deep Zn-diffusion.

width were routinely obtained. The transport of InP was carried out at temperatures between 600° and 670°C, depending on the desired amount of transport. The wafer was then loaded into an ampoule along with some zinc-phosphide powder. Two different modes of Zn-diffusion have been used in different experiments. In the first mode, a Zn skin-diffusion was used to reduce contact resistance. The wafer was coated with phosphosilicate glass (PSG), photolithographically processed to form stripe openings on the mesa tops, and diffused at 600°C for 2.5 min. to form heavily doped regions in the stripe openings. In the second mode, a deep Zn-diffusion was used to modify the cap doping profile as illustrated in Fig. 1-1(c). The wafer was uncoated and was diffused first at 450°C for 160 to 196 min., and then at 600°C for 2.5 min. Figure 1-2 shows an SEM photograph of a stained cross section of a sample thus diffused. Except for the two most recent wafers (584 and 586), all other wafers reported here were only skin-diffused.

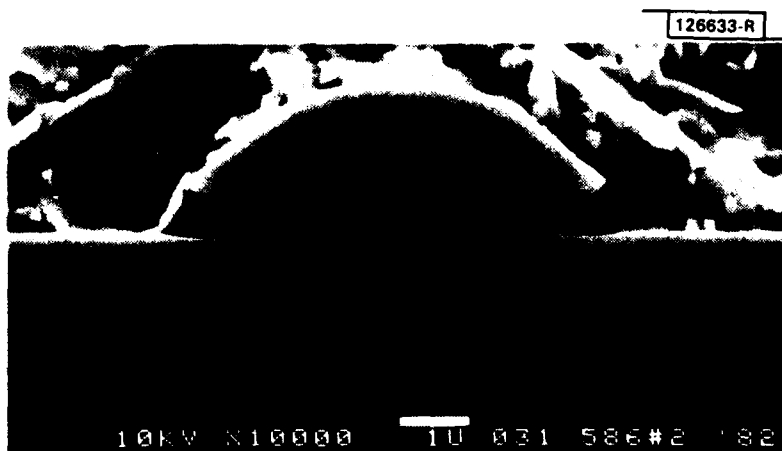


Fig. 1-2. SEM photograph of a stained cross section of BH after deep Zn-diffusion. In this sample, active region is 0.7 μm wide.

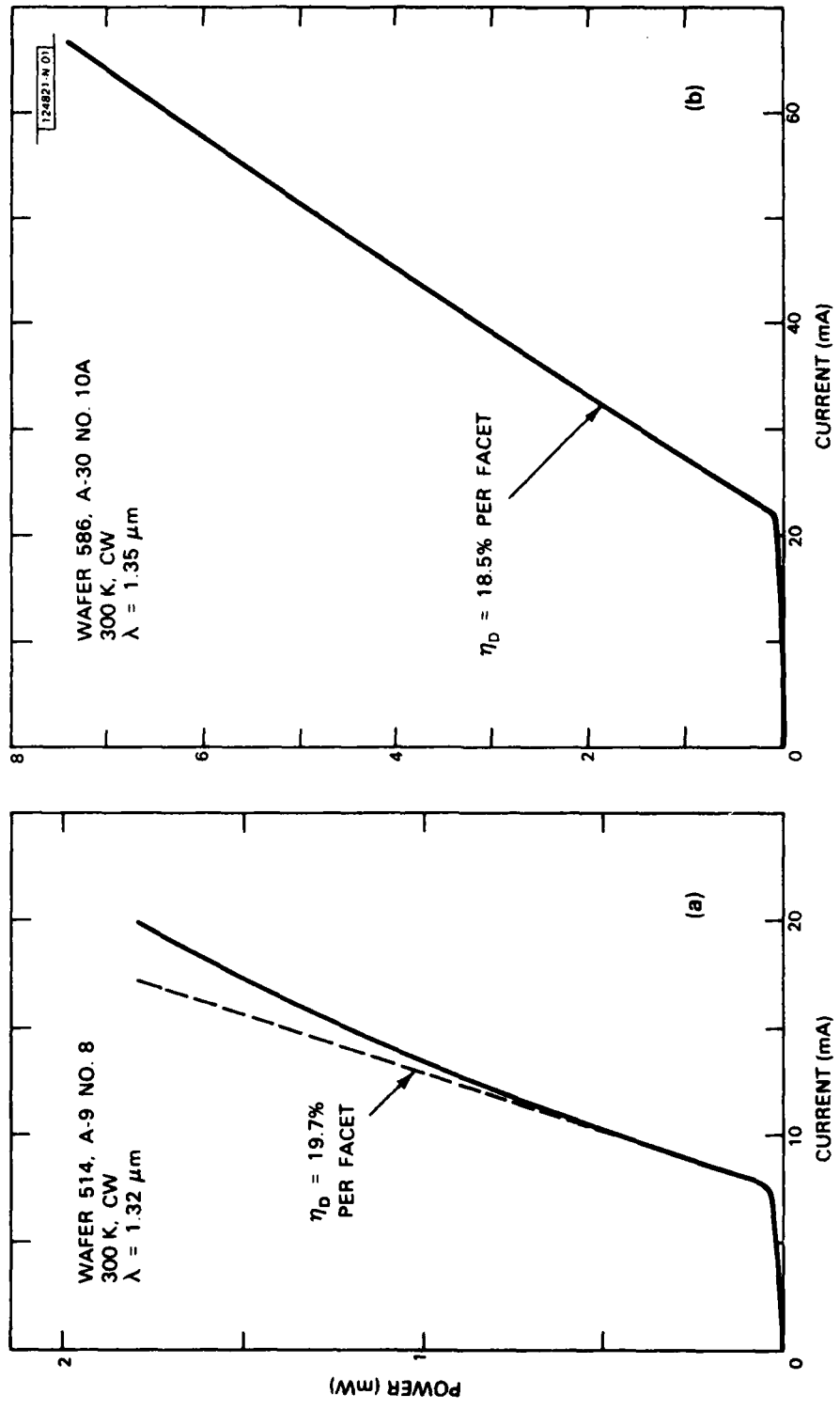


Fig. 1-3. L-I characteristics of BH lasers (a) without and (b) with deep Zn-diffusion.

Since the supporting mesas were first implemented, high device yield has been routinely obtained. For example, 80 percent of the 130 devices tested for Wafer 551 showed threshold currents between 10 and 30 mA. The lowest threshold was 5.5 mA, obtained for Wafer 514. The highest differential quantum efficiency was 27 percent per facet, obtained on a device of Wafer 513 with active regions of 3.0- to 3.6- μm width and a threshold current of 17 mA. The light-current (L-I) characteristics, however, typically exhibited deviations from linearity slightly above threshold, as shown in Fig. 1-3(a).

This deviation from linearity is presumably due to current leakage across the pn homojunctions, whose locations, based on SEM observations of stained cross sections, are shown in Fig. 1-1(b). The current leakage can be prevented either by increasing the conductivity of the p-type InP cap or by locating the pn homojunctions in low-voltage regions. In this work, both of the above-mentioned solutions were achieved by the deep Zn-diffusion as illustrated in Fig. 1-1(c). Since high Zn-concentration in or near the active region has been known to greatly increase the laser threshold,^{8,9} the deep Zn-diffusion in this work is designed so that a lightly doped core region is retained for laser action.

Two wafers with deep Zn-diffusion have been fabricated. Typical threshold currents were in the range of 12 to 30 mA. These devices showed significantly improved L-I linearity [Fig. 1-3(b)]. Improved temperature dependence of threshold current, $T_0 = 81$ K, was also obtained as compared with $T_0 = 46$ to 67 K without deep Zn-diffusion. The differential quantum efficiencies were typically 17 percent per facet, which is lower than the best obtained on devices without the deep diffusion and may be due to the stripe unevenness observed on these two wafers. Deep zinc-diffusion is a simple and effective method to improve the L-I linearity and T_0 in the mass-transported BH lasers without the use of reverse-biased junctions.

Z.L. Liao
J.N. Walpole
D.Z. Tsang

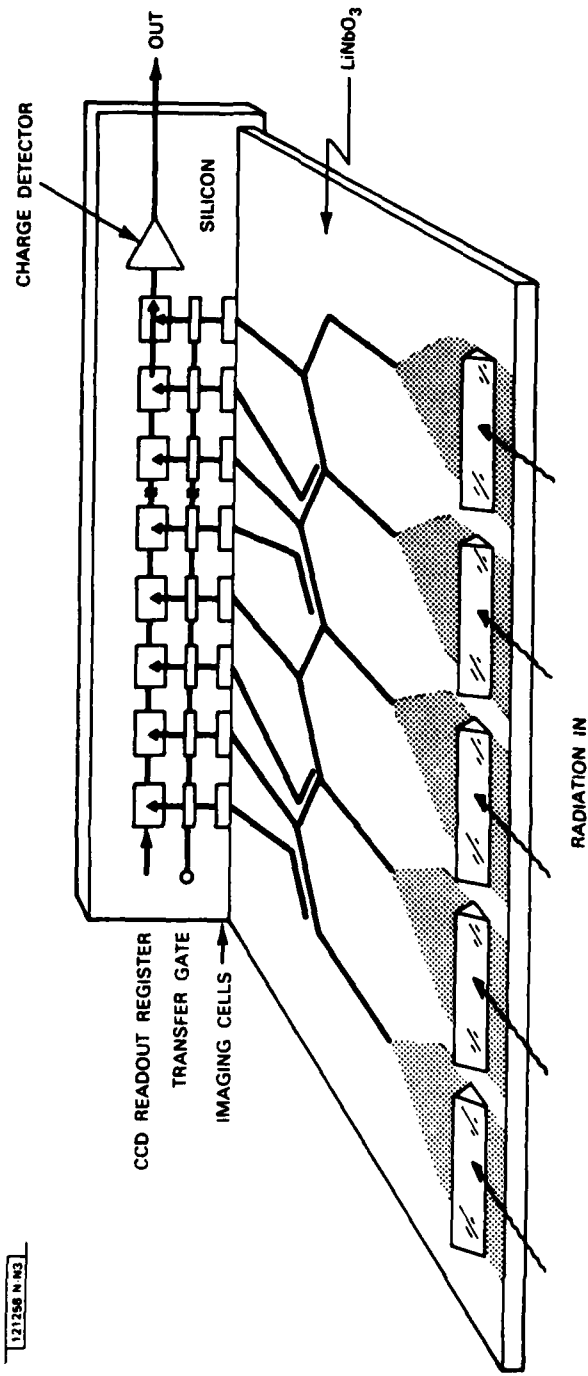


Fig. 1-4. Schematic representation of wavefront measurement sensor illustrating interferometer array coupled into a CCD imager.

121258 N 83

1.2 INTEGRATED OPTICS WAVEFRONT MEASUREMENT SENSOR

Integrated circuits incorporating arrays of Mach-Zehnder interferometers have been developed for high-speed signal processing.^{10,11} Here, we describe the use of a guided-wave interferometer array to measure the phase and amplitude across an optical wavefront. This represents the first use of integrated optics for analog processing of optical wavefronts. This new technique for measuring a spatially varying optical wavefront has advantages over conventional bulk optics techniques. For tilted 0.84- μm plane waves incident on the array, it is found that the phase determined by the interferometer outputs agrees to $<3^\circ$ with theory [3° corresponds to an optical path difference (OPD) of $\lambda/120$]. The phase variation between devices separated by 3.1 mm is $<20^\circ$ (corresponding to an OPD of $\lambda/18$).

The wavefront measurement sensor is presented schematically in Fig. 1-4 where prism-horn inputs are shown as examples of receiving antennas for the single-mode dielectric guides of the interferometer as well as directional couplers to determine the intensity of the radiation incident on the antennas. The output of each interferometer gives a measure of the phase difference between the waves incident on adjacent antennas. The input beam is scanned in the plane perpendicular to that of the array. The phase profile of the incident radiation is constructed from the measured phase differences. Figure 1-4 also shows a CCD imager and readout as the output of this all-solid-state wavefront measurement sensor.

Results are presented on the performance of the interferometer. Theory predicts that, for equal arm lengths, the power in the output guide of the Mach-Zehnder interferometer P_ϕ is related to powers in the directional coupler waveguides, denoted by P_1 or P_2 , by

$$P_\phi = 1/2 [(P_1^{1/2} - P_2^{1/2})^2 + 4P_1^{1/2}P_2^{1/2} \cos^2 \frac{\phi}{2}] B \quad (1-1)$$

where ϕ is the phase difference between the optical waves incident on the two arms of the interferometer, and the factor B takes into account the coupling and losses.

For equal illumination of the waveguides, $P_1 = P_2 = P$, and

$$P_\phi = [2P \cos^2 \frac{\phi}{2}] B \quad (1-2)$$

To evaluate the interferometric array, the technique shown in Fig. 1-5 was used. With the two-mirror system shown, an incident planar wavefront could be tilted and yet maintained on the same position on the LiNbO_3 sample, and in this manner the phase difference ϕ incident on the interferometer could be varied. The incident radiation was at 840 nm and was produced by a collimated GaAs laser beam. While Fig. 1-5 only shows one interferometer on the LiNbO_3 wafer, in fact there are 18 such interferometers on one wafer.

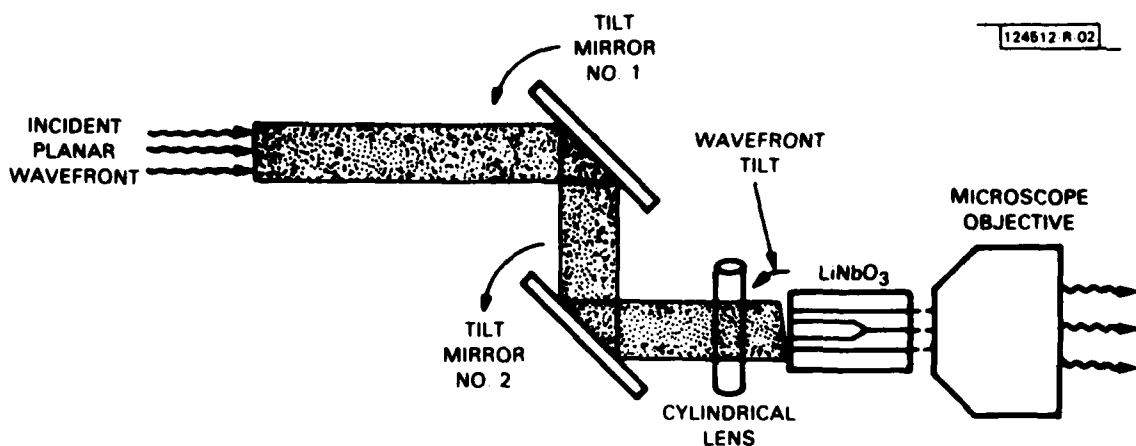


Fig. 1-5. Experimental arrangement to tilt planar wavefront and maintain its position on LiNbO_3 sample containing interferometer under test.

Figure 1-6 shows the comparison of experimental results with the theory predicted by Eq. (1-2). As previously stated, the agreement between theory and experiment was within 3° for each device. The curves for two of the interferometers have been shifted by a constant phase 20° for clarity. This small shift (which corresponds to a path difference <math><25\text{ nm}</math> in LiNbO_3) indicates the degree of uniformity among devices separated by 3 mm. A shift of this magnitude could be electrooptically compensated.

The results presented show that, because of the excellent fit to theory and excellent uniformity of Mach-Zehnder dielectric-waveguide interferometers in LiNbO_3 , these components should not limit the accuracy of the wavefront measurement sensor. Theory predicts that the limitation to the accuracy, which is due to signal statistics and noise, is for most cases of interest more severe than that experimentally determined above for the interferometers.

R.H. Rediker
T.A. Lind
F.J. Leonberger

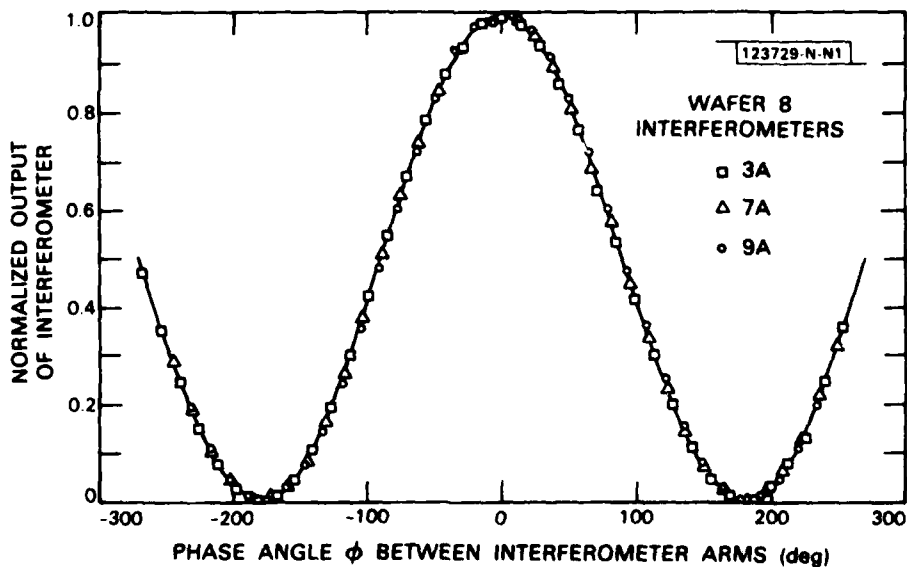
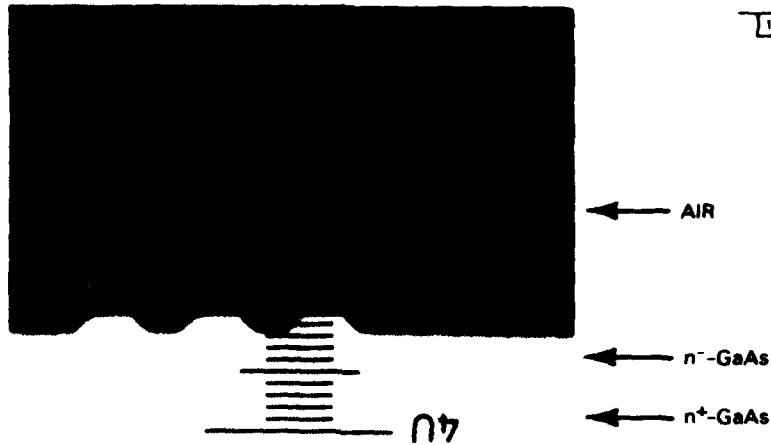
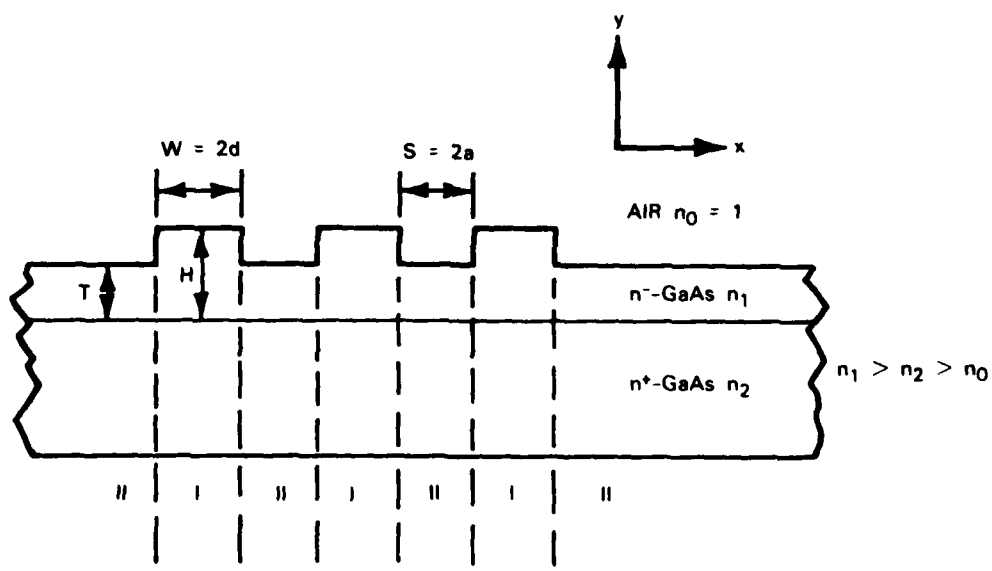


Fig. 1-6. Experimental data points $P_\phi / (P_1 + P_2)$, normalized so that maximum value of ratio is unity, are compared with theoretical curve $\cos^2(\phi/2)$. Phase angle ϕ for experimental points has been adjusted by a constant for each interferometer for best fit.



(a)



(b)

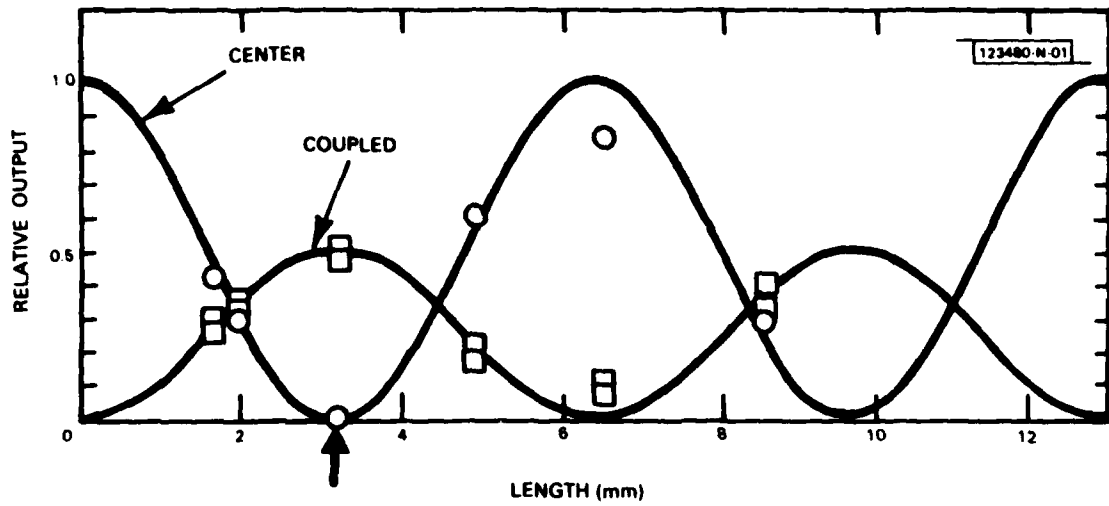
Fig. 1-7. (a) Photomicrograph of cleaved cross section of GaAs three-guide coupler. Sample has been treated with a stain/etchant to reveal n⁻-n⁺ interface. Scale on photomicrograph is 1 μm/div. (b) Schematic cross section of three-guide coupler with rectangular ribs of a width equal to average width (same cross-sectional area) of actual guides. Regions I and II are modeled as slab waveguides to determine effective guide index in different portions of n⁻-layer.

1.3 THREE-GUIDE OPTICAL COUPLERS IN GaAs

Optical couplers are an important component of almost all integrated optical circuit concepts. There have been a number of reports on two-guide optical couplers including experimental results on couplers fabricated on GaAs (Refs. 12 through 20), InP (Ref. 21), and GaInAsP (Ref. 22). Work reported to date on three-guide couplers has been theoretical.^{23,24} When used to couple power from one outside guide to the other outside guide, the three-guide coupler has sharper transfer characteristics than a similar two-guide coupler and it has been proposed to use this feature for improved sampling and filtering.²⁴ Another possible application of three-guide couplers is their use as symmetrical power dividers and combiners.

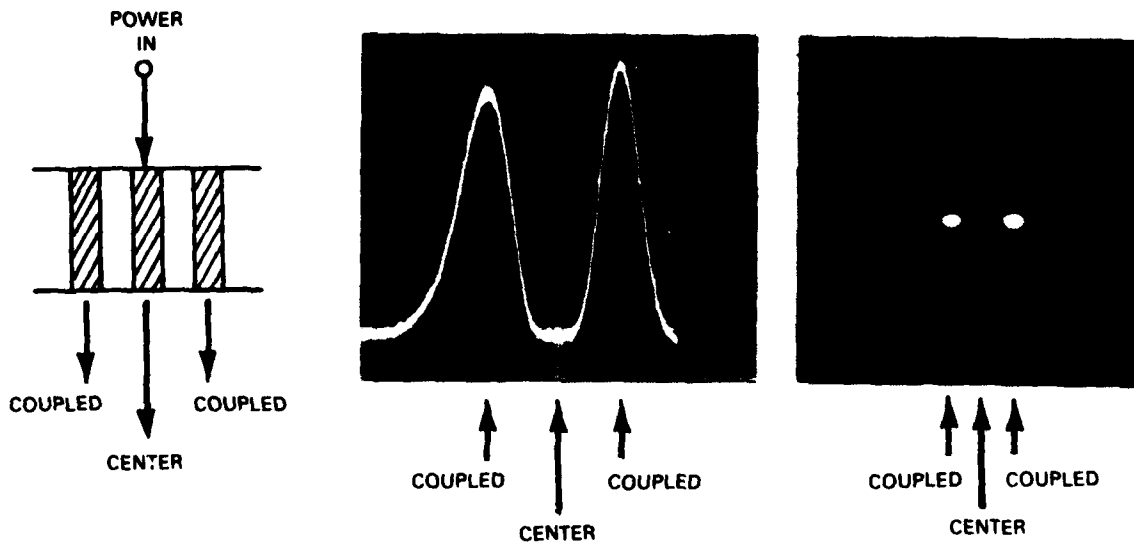
The symmetrical three-guide couplers used in these experiments are composed of three slab-coupled rib-waveguides in close proximity as shown in Fig. 1-7(a). The individual waveguides were designed to be single mode²⁵ and consist of a rib etched in a normally undoped n^- -GaAs epitaxial layer grown on a (100)-oriented $2 \times 10^{18} \text{ cm}^{-3} n^+$ -GaAs substrate. The epitaxial layer was n-type with a carrier concentration of $1 \times 10^{15} \text{ cm}^{-3}$ and had a thickness of 4.2 μm . Details of the fabrication can be found in Ref. 26. Note that, because of an orientation-dependent etch rate, the ribs in Fig. 1-7(a) are actually trapezoidal in shape. The mean width of a rib is 4.75 μm , and the mean spacing or separation between ribs is 4.25 μm . The height of the rib is 1.5 μm . After the ends were cleaved, the sample was mounted on a high-performance translation-rotary stage for optical evaluation. Following evaluation at one length, the sample was cleaved to a shorter length and the evaluation repeated.

Optical measurements were made using an end-fired coupling scheme.¹⁵ Radiation from a single-mode CW GaInAsP/InP double-heterojunction laser operating at 1.28 μm was collimated, passed through a polarizer, aperture and neutral density filter, and focused on the cleaved input face of the waveguide sample using a microscope objective. The electric field of the input light was polarized parallel to the plane of the slab. The input from



(a)

FOR 3.2-mm LENGTH:



(b)

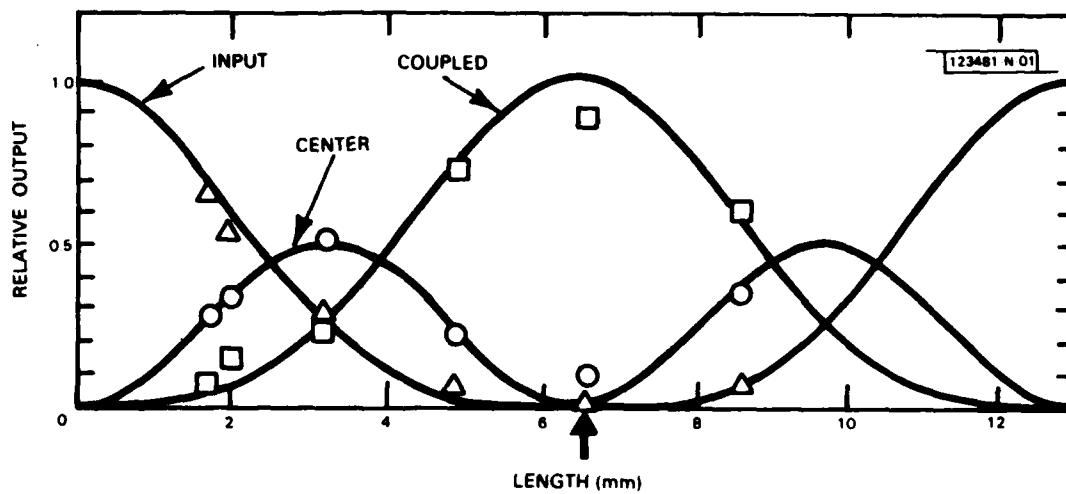
Fig. 1-8. (a) Relative output power out of each guide as a function of length for a three-guide coupler with input power into center guide. (b) Outputs obtained on oscilloscope and TV monitor for a length of 3.2 mm.

the waveguide sample was focused by a beam-splitting microscope into two images. One output image went to an infrared TV camera system and the other image was passed through a pinhole aperture onto a Ge photodiode. The output image could either be scanned across the pinhole aperture using a scanning mirror, or the aperture could be precisely translated across the image. When the scanning mirror was used, the output of the Ge detector could be displayed on an oscilloscope as a function of effective position. For comparison purposes, single isolated guides, three- and two-guide couplers were evaluated.

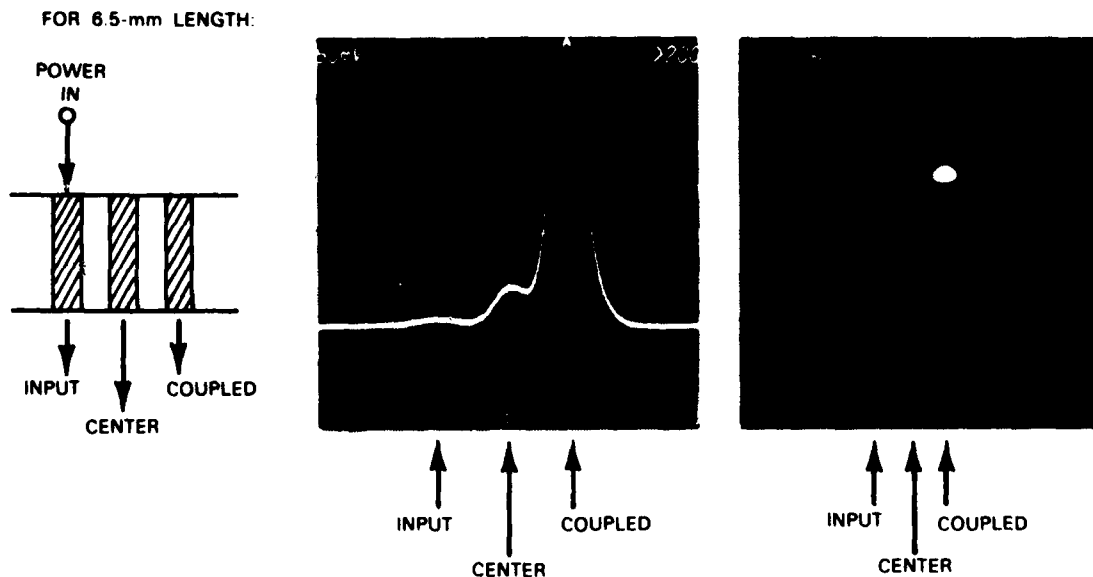
Since an exact analysis of these three-guide couplers is not possible, an extension of the effective index method^{27,28} was used to obtain an approximate analytic solution and some insight into device behavior. Details of this analysis can be found in Ref. 27. In the limit of loose coupling between guides,^{23,24} power input into the center guide will be symmetrically transferred to the two outside guides in a coupling length, $L_{CT \rightarrow O}$. This coupling length is $\sqrt{2}$ times larger than that of a similar two-guide coupler. For power into an outside guide of the three-guide coupler, all the power is transferred to the other outside guide in a distance $L_{O1 \rightarrow O2}$, which is twice as long as that needed to symmetrically couple power from the center guide to the two outside guides.

For the isolated single guides, a single intensity maximum was observed under the rib as expected, and the outputs of the two- and three-guide couplers as a function of length were in good agreement with that expected from theory.

The best fit to the experimental data gave a coupling length for symmetrically transferring power from the center guide of a three-guide coupler to the two outside guides, $L_{CT \rightarrow O}$, of ≈ 3.2 mm. Figure 1-8(a) shows the relative power out of each guide of a three-guide coupler vs length for power input into the center guide. Shown in Fig. 1-8(b) is an oscilloscope and TV output obtained for a length of 3.2 mm. Most of the asymmetry in the oscilloscope photograph is due to the scanning optics. The solid curves in Fig. 1-8(a) are plots of the results expected from loose-coupling theory



(a)



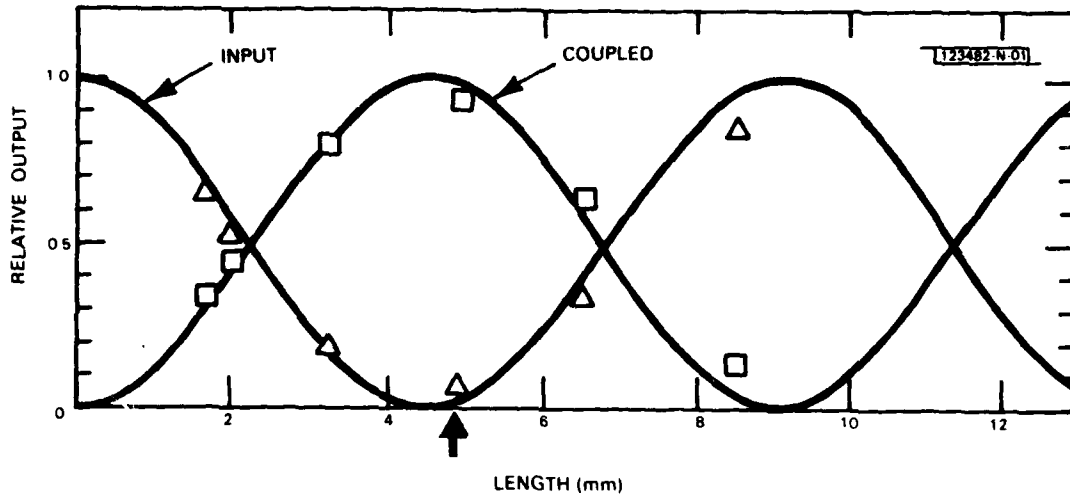
(b)

Fig. I-9. (a) Relative output power out of each guide as a function of length for a three-guide coupler with input power into one of outside guides. (b) Outputs obtained on oscilloscope and TV monitor for a length of 6.5 mm.

using a coupling length of 3.2 mm. The relative power output of all three guides is a reasonably good fit to the approximate power-division equations. At a length of 3.2 mm, the power input to the center guide is divided between the two outside guides, with minimal power (<1 percent) remaining in the center guide.

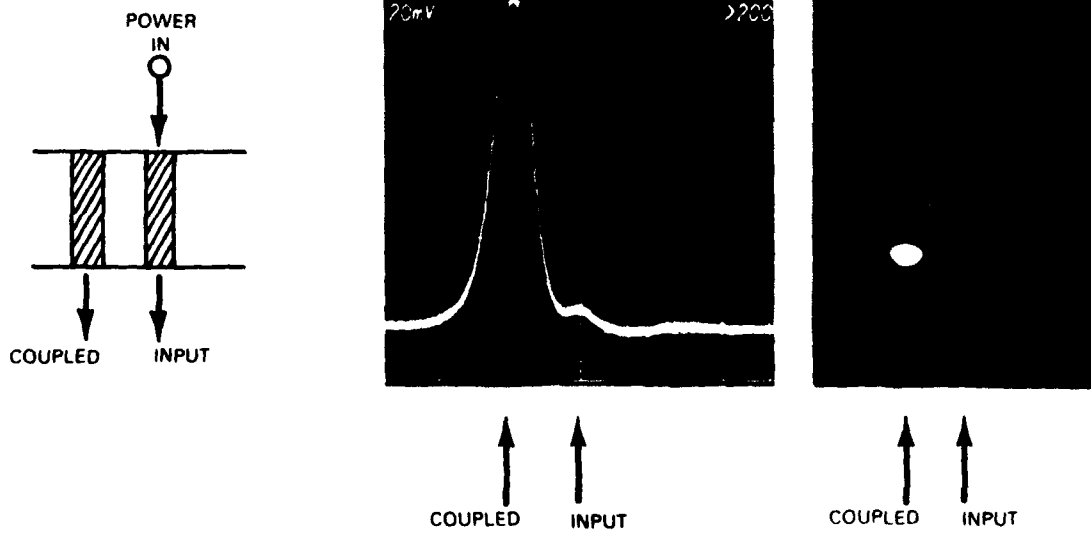
With the effective guide index method, the coupling length to transfer power from the center guide to the two outside guides (L_{CT+0}) was calculated to be 2.85 mm using the loose-coupling approximation, and 2.79 mm using the actual eigenmode equations to calculate the propagation constants of the modes of the three-guide coupler. In these calculations, the average width of the trapezoidal ribs (4.75 μm) and average spacing (4.25 μm) were used.²⁵ The effective index of the epitaxial layer n_1 was taken²⁹ as 3.43, and the usual free carrier effect on index was used to determine the index of the n^+ -substrate n_2 . The agreement between the calculated and experimental coupling lengths is quite good (~12.5-percent difference). It is not clear how much of the difference is due to inherent limitations in the effective guide index calculation and how much is due to the use of inaccurate waveguide parameters.

Figure 1-9(a) shows the relative power out of each guide of the same three-guide coupler vs length for power into an outside guide. The oscilloscope and TV outputs at a length of 6.5 mm are shown in Fig. 1-9(b). The solid lines in Fig. 1-9(a) are plots of the results expected from loose-coupling theory with a coupling length (L_{O1+O2}) twice as long as that used in Fig. 1-8. The coupling length in the loose-coupling approximation for complete power transfer from one outside guide to the other should be 6.4 mm. The data obtained at a length of 6.5 mm, which is slightly longer, show most of the power in the coupled outside guide (~86 percent), a small amount in the center guide (~11.5 percent), and only ~2.5 percent in the input outside guide. Since in this case there are three modes whose phase velocities are not related to each other in a simple way (only an approximation for loose coupling), the beats between these modes and therefore the power transfer are not expected to be as good as in the case where the power input was into the center guides. Although it is not clear why there is so much residual power



(a)

FOR 4.9-mm LENGTH:



(b)

Fig. 1-10. (a) Relative output power of each guide as a function of length for a two-guide coupler. (b) Outputs obtained on oscilloscope and TV monitor for a length of 4.9 mm.

in the center guide at a length of 6.5 mm, there is fairly good overall agreement between the measured relative powers and those expected from the coupling theory.

For comparison, Fig. 1-10(a) shows the relative output of each guide of a two-guide coupler vs length, and Fig. 1-10(b) shows the oscilloscope and TV outputs at a length of 4.9 mm. The solid line represents the power-division equations of a two-guide coupler with a coupling length $\sqrt{2}$ times larger than that of a three-guide coupler with power input into the center guide. At a length of 4.9 mm, which is somewhat longer than the 4.5-mm coupling length, there is still almost complete power transfer from one guide to another.

In summary, symmetrical three-guide couplers, whose behavior closely approximates that predicted using an effective-index analytical method, have been fabricated in GaAs.

J.P. Donnelly
N.L. DeMeo
G.A. Ferrante

REFERENCES

1. M. Hirao, A. Doi, S. Tsuji, M. Nakamura, and K. Aiki, J. Appl. Phys. 51, 4539 (1980).
2. I. Mito, M. Kitamura, Ke. Kobayashi, and Ko. Kobayashi, Electron. Lett. 18, 953 (1982).
3. K.L. Yu, U. Koren, T.R. Chen, and A. Yariv, IEEE J. Quantum Electron. QE-18, 817 (1982).
4. H. Namizaki, R. Hirano, H. Higuchi, E. Oomura, Y. Sakakibara, and W. Susaki, Electron. Lett. 18, 703 (1982).
5. R.A. Logan, J.P. van der Ziel, H. Temkin, and C.H. Henry, Electron. Lett. 18, 895 (1982).
6. H. Ishikawa, H. Imai, T. Tanahashi, K. Hori, and K. Takahei, IEEE J. Quantum Electron. QE-18, 1704 (1982).
7. Z.L. Liao and J.N. Walpole, Appl. Phys. Lett. 40, 568 (1982), DTIC AD-A121779.
8. Y. Itaya, Y. Suemetsu, S. Katayama, K. Kishino, and S. Arai, Jpn. J. Appl. Phys. 18, 1795 (1979).
9. W. Ng and Y.Z. Liu, Electron. Lett. 16, 693 (1980).
10. R.A. Becker and F.J. Leonberger, IEEE J. Quantum Electron. QE-18, 1411 (1982).
11. M. Izutsu, S. Shikama, and T. Sueta, IEEE J. Quantum Electron. QE-17, 2275 (1981).
12. S. Somekh, E. Garmire, A. Yariv, H.L. Garvin, and R.G. Hunsperger, Appl. Phys. Lett. 22, 46 (1973).
13. S. Somekh, E. Garmire, A. Yariv, H.L. Garvin, and R.G. Hunsperger, Appl. Opt. 13, 327 (1974).
14. J.C. Campbell, F.A. Blum, D.W. Shaw, and K.L. Lawley, Appl. Phys. Lett. 27, 202 (1975).
15. F.J. Leonberger, J.P. Donnelly, and C.O. Bozler, Appl. Phys. Lett. 29, 652 (1976), DDC AD-A037627/7.

16. F.J. Leonberger, J.P. Donnelly, and C.O. Bozler, Appl. Opt. 17, 2250 (1978), DDC AD-A060932/1.
17. J.C. Shelton, F.K. Reinhart, and R.A. Logan, Appl. Opt. 17, 2548 (1978).
18. J.C. Shelton, F.K. Reinhart, and R.A. Logan, J. Appl. Phys. 50, 6675 (1979).
19. A. Carencio, L. Menigaux, and P.L. Delpuch, J. Appl. Phys. 50, 5139 (1979).
20. A. Carencio and L. Menigaux, J. Appl. Phys. 51, 1325 (1980).
21. A. Carencio, N.T. Linh, and L. Menigaux, Appl. Phys. Lett. 40, 653 (1982).
22. N.L. DeMeo, F.J. Leonberger, and S.H. Groves, Topical Meeting on Integrated and Guided-Wave Optics, Pacific Grove, California, 6-8 January 1982, Digest of Technical Papers, pp. WD7-1 - WD7-3.
23. K. Iwasaki, S. Kurazono, and K. Itakuna, Electronics and Communications in Japan 58-C, 100 (1975).
24. H.A. Haus and C.G. Fonstad, Jr., IEEE J. Quantum Electron. QE-17, 2321 (1981).
25. E.A.J. Marcatili, Bell Syst. Tech. J. 53, 645 (1974).
26. J.P. Donnelly, N.L. DeMeo, and G.A. Ferrante (to be published in IEEE J. Lightwave Tech.).
27. V. Ramaswamy, Bell Syst. Tech. J. 53, 697 (1974).
28. W.V. McLevige, T. Itoh, and R. Mittra, IEEE Trans. Microwave Theory Tech. MTT-23, 788 (1975).
29. D.T.F. Marple, J. Appl. Phys. 35, 124 (1964).

2. QUANTUM ELECTRONICS

2.1 SEARCH FOR NEW V^{2+} HOSTS

Analysis of the operation of the CW V:MgF₂ laser¹ shows that excited-state absorption (ESA) from the ${}^4T_2 \rightarrow {}^4T_1$ transition causes a considerable reduction in the effective laser-gain cross section. A value of $\sim 9 \times 10^{-22} \text{ cm}^2$ was found from measurement of the laser threshold, compared with the value of $\sim 5 \times 10^{-21} \text{ cm}^2$ deduced from spectroscopic techniques (which do not account for ESA). This small effective cross section precludes use of the V:MgF₂ laser for many applications, especially in flashlamp-pumped amplifier chains needed for fusion drivers.

The excellent match between the broad ${}^4A_2 \rightarrow {}^4T_2$ and ${}^4A_2 \rightarrow {}^4T_1$ absorption bands of the V^{2+} ion and the emission spectra of xenon lamps, which was one of the initial reasons for examining V:MgF₂, provides enough incentive to search for other host crystals with ligand fields sufficiently different from MgF₂ such that effects of ESA are reduced, if not eliminated. One crystal discussed previously¹ is MnF₂, which has a smaller ligand field than MgF₂. From the Tanabe-Sugano diagrams² for the V^{2+} ion, it appears, however, that crystals with somewhat larger values of Dq would be more likely to have a smaller ESA; from published spectroscopic data,³ one such crystal is the perovskite KMgF₃.

Large, crack-free crystals of V:KMgF₃ doped with 0.5 wt% VF₂ were grown by the vertical gradient-freeze technique described previously.⁴ The concentration appeared more uniform over the 7-cm length of the crystals than that observed for V:MgF₂. Considerable optical scattering throughout the material was evident; this is attributed to water present in the hygroscopic starting powder KF.

Observation of the fluorescence emission from V:KMgF₃ indicated one property significantly different from V:MgF₂: efficient ${}^4T_2 \rightarrow {}^4A_2$ fluorescence was observed at room temperature. Figure 2-1 shows the measured fluorescence lifetime from V^{2+} in KMgF₃, MgF₂, and MnF₂ as a function of

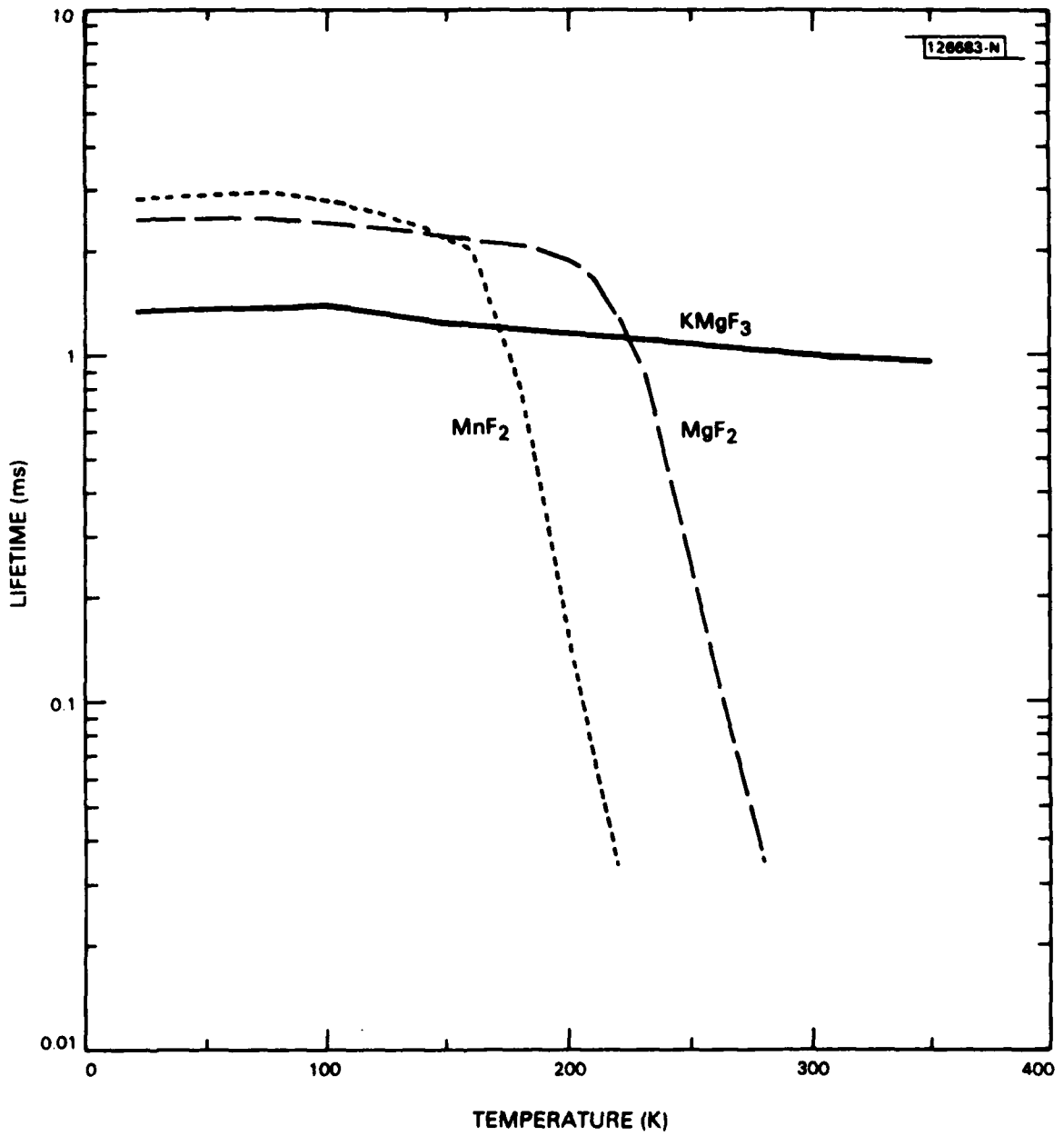


Fig. 2-1. ${}^4T_2 + {}^4A_2$ fluorescence lifetime vs temperature in three different host crystals.

temperature. The rapid reduction in lifetime with increasing temperature for MnF_2 and MgF_2 is due to the activation of a nonradiative channel for decay of the 4T_2 state. (Attempts at understanding the physical basis for this channel have not been successful.) In KMgF_3 , the lifetime reduction from 20 to 350 K is slight and may be accounted for entirely by a change in the radiative rate. Figure 2-2 plots the emission spectrum of V:KMgF_3 at 300 K, showing a peak emission wavelength of $1.03 \mu\text{m}$, as expected, shorter than the $1.12\text{-}\mu\text{m}$ peak of V:MgF_2 .

Current efforts include (1) measurement of gain in V:KMgF_3 to determine if ESA has been reduced from that in V:MgF_2 , and (2) attempts to remove water from the initial charge used for crystal growth in order to eliminate scattering. If there is reasonable gain in V:KMgF_3 , this system should allow construction of an efficient, tunable, room-temperature laser operating in the $1\text{-}\mu\text{m}$ wavelength region.

P.F. Moulton
R.E. Fahey

2.2 LINEWIDTH OF (GaAl)As DIODE LASERS WITH HIGH-REFLECTIVITY COATINGS

Recent investigations^{5,6} have shown that the linewidth of single-frequency (GaAl)As diode lasers is broadened by mechanisms which are not described by traditional laser theories. This additional linewidth broadening is a result of the strong coupling between the refractive index, the inversion density, and the laser field intensity in (GaAl)As diode lasers. The linewidth is found to depend linearly on the reciprocal output power, but varies with a slope which is approximately one-order-of-magnitude larger than predicted by the Schawlow-Townes formula. A recent model developed by Henry⁷ explains this anomalous behavior as being caused by changes in the imaginary part of the refractive index induced by spontaneous emission events via phase and intensity changes in the laser field. These changes are accompanied by changes in the real part of the refractive index, thus causing line broadening. These fundamental line-broadening mechanisms have direct implications for the applications of single-frequency diode

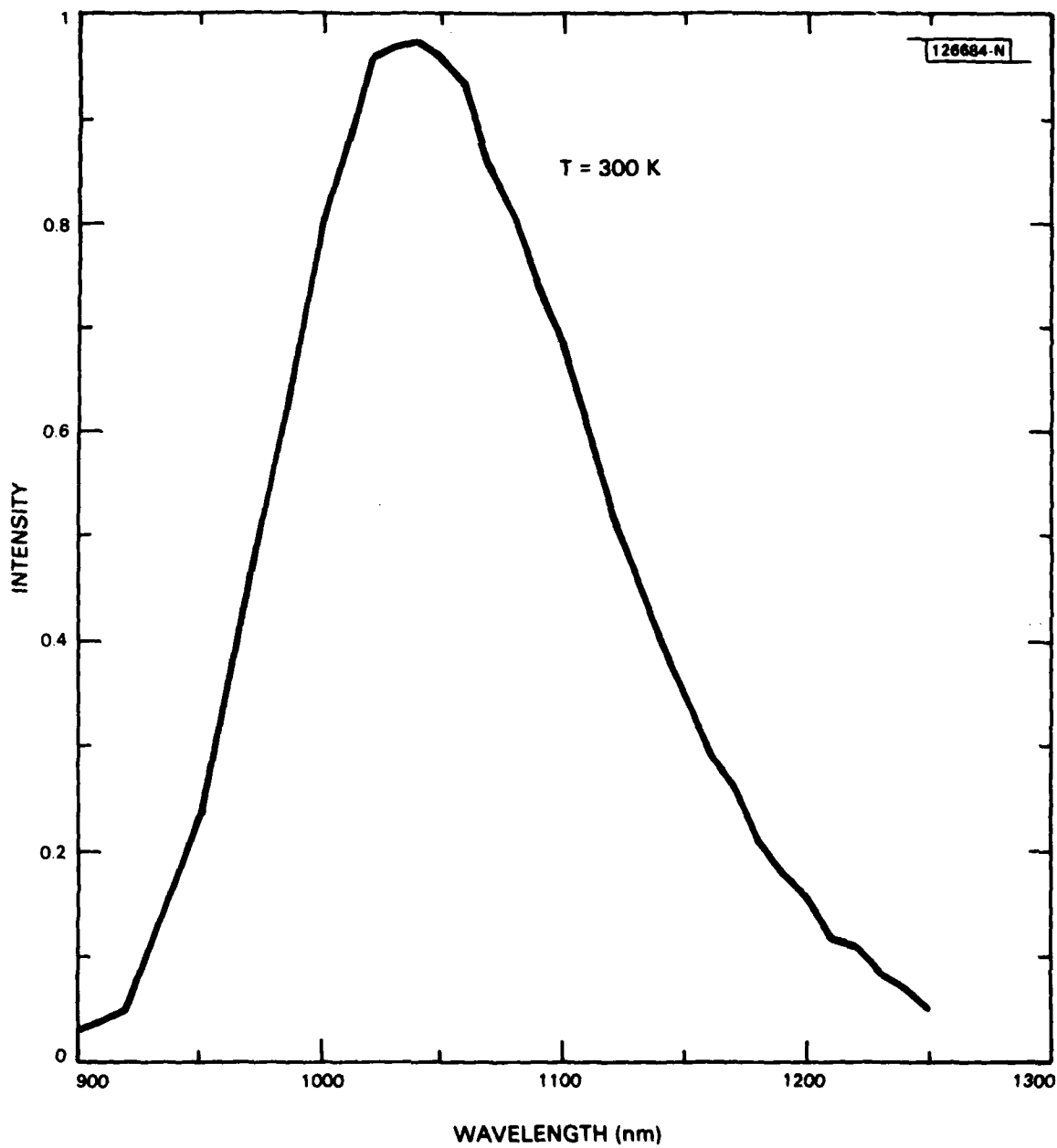


Fig. 2-2. Spectrum of ${}^4T_2 + {}^4A_2$ fluorescence from V:KMgF₃ at 300 K.

lasers since they limit the achievable frequency purity. The output power and temperature dependence of the linewidth have been studied previously. As a further test of laser linewidth theories, we have measured the linewidth of a (GaAl)As diode laser which had a high-reflectivity coating on one facet and thus a higher cavity Q-factor.

A set of experiments was performed with a single-frequency channel-substrate-planar (CSP) Hitachi diode laser. By means of CVD, a high-reflectivity Al-coating was applied onto the back facet of the diode after the diode had been covered with an initial layer of SiO_2 in order to prevent short circuiting the device. Figure 2-3 shows the single-sided output power of this diode laser as a function of the injection current before and after the coating was applied. If an unchanged loss coefficient of $\alpha = 45 \text{ cm}^{-1}$ is assumed, the observed change in the threshold current yields a reflectivity of 80 percent for the Al-coated back facet. The linewidth of the diode laser was measured with a scanning Fabry-Perot interferometer which had a

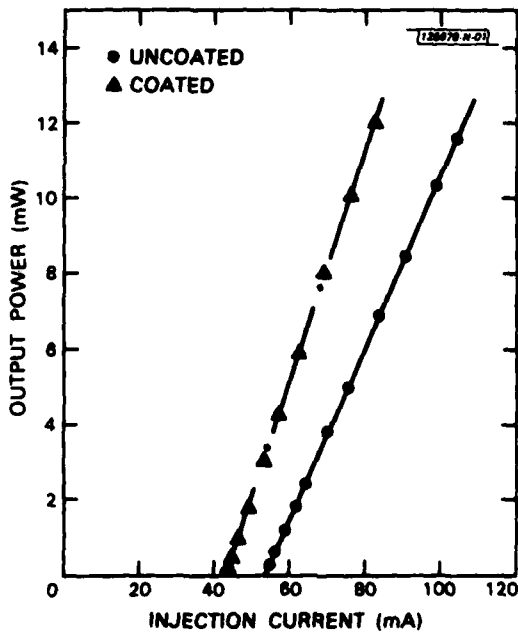


Fig. 2-3. Single-sided output power vs injection current for CSP-(GaAl)As diode laser before and after high-reflectivity coating was applied.

resolution of 3.5 MHz. A neutral density filter of 10^3 attenuation was placed immediately after the collimating lens in order to minimize optical-feedback effects. Figure 2-4 shows the linewidth of the laser diode as a function of the reciprocal single-sided output power. Each data point is the average of several Fabry-Perot scans. The laser output power was measured with a calibrated silicon photodiode. A 1-m Czerny-Turner spectrometer was used to verify single-frequency operation of the laser.

According to Henry's theory,⁷ the linewidth is given by

$$\Delta\nu = (h\nu/8\pi P_o) (C/nL)^2 (\ln R - \alpha L) \ln R n_{sp} (1 + \beta^2) \quad (2-1)$$

where n_{sp} is the spontaneous emission factor, and β is the ratio of the change in the real part to the change in the imaginary part of the refractive index due to spontaneous-emission events over the same period of time.

Without Henry's enhancement factor β , Eq. (2-1) is essentially the

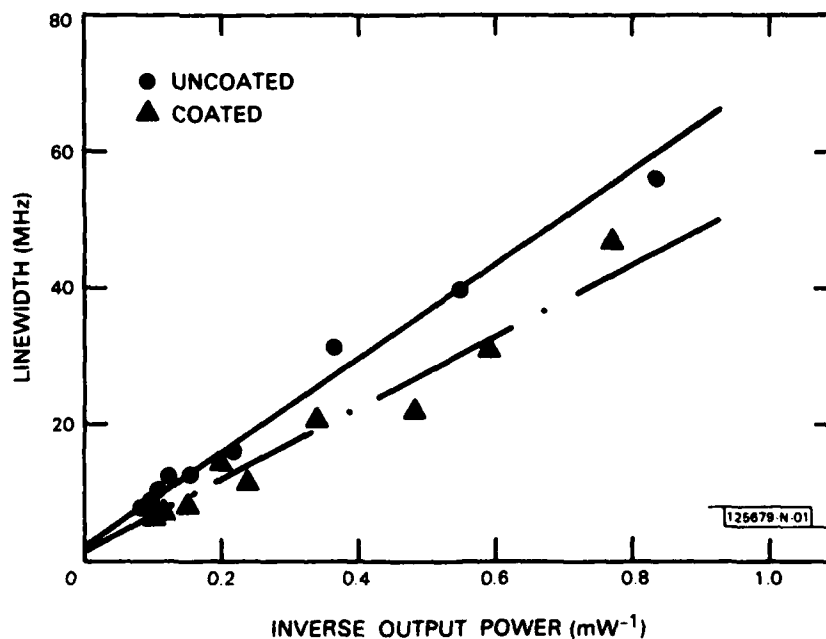


Fig. 2-4. Laser linewidth as a function of inverse output power before and after high-reflectivity coating was applied.

Schawlow-Townes linewidth formula, which predicts a value of 4.2 MHz mW for the slope in Fig. 2-4 (before coating) whereas the experimental result is 68 MHz mW. A value of $\beta = 3.9$ in Eq. (2-1) is necessary to explain this result, which compares with $\beta = 3.8$ found for a TJS Mitsubishi diode laser.

Comparing a standard diode laser with identical facet reflectivities R for both facets and a device which has an ideal high-reflectivity coating of $R = 1$ on the rear facet, one expects a decrease in the linewidth according to

$$\Delta\nu_{\text{coated}}(P_o) = 2 \times \Delta\nu_{\text{uncoated}}(P_o) \frac{(\ln\sqrt{R} - \alpha L) (\ln\sqrt{R})}{(\ln R - \alpha L) \ln R} \times \frac{(1 + \beta_{\text{coated}}^2)}{(1 + \beta_{\text{uncoated}}^2)} \quad (2-2)$$

where R is the reflectivity of the uncoated front facet, and $\Delta\nu_{\text{coated}}$ and $\Delta\nu_{\text{uncoated}}$ are normalized for the same single-sided output power P_o . The factor 2 in Eq. (2-2) accounts for the fact that line-broadening mechanisms depend on the internal laser power, which at the same single-sided output power P_o is twice as high in case of the standard device with light output from both facets.

Figure 2-4 shows that the high-reflectivity Al-coating reduces the linewidth of the laser diode by a factor of 1.28. Equation (2-2), which has been derived for a high-reflectivity coating of $R = 1$, holds well for our device with $R = 0.8$ and predicts a linewidth reduction of

$$1.3 \times \frac{(1 + \beta_{\text{coated}}^2)}{(1 + \beta_{\text{uncoated}}^2)} .$$

This comparison of the experimental behavior and Henry's linewidth theory suggests that the enhancement factor β is not significantly changed by the applied high-reflectivity coating. Further investigations of coated diode lasers are planned which will enable an independent determination of β . The

dependence of the linewidth on inverse power in Fig. 2-4 exhibits a positive intercept and suggests a power-independent contribution to the laser linewidth, as has been observed for uncoated TJS Mitsubishi lasers. Experiments are under way in order to study the influence of high-reflectivity coatings on this phenomenon.

In conclusion, the application of a high-reflectivity coating on the back facet of a (GaAl)As laser was found to cause a reduction in the threshold current and the laser linewidth. The dependence of linewidth on output power can be described with Henry's linewidth theory, and the experiments indicate that additional linewidth broadening due to spontaneous-emission-induced fluctuations of the imaginary part of the refractive index does not vary significantly with the facet reflectivity.

W. Lenth

2.3 ENHANCED RAMAN SCATTERING FROM SMALL SI STRUCTURES

We have observed enhancement of the intensity of spontaneous Raman scattering from roughened Si surfaces. Enhanced scattering has been observed from samples prepared in several different ways, but all exhibit surface structures with dimensions on the order of 0.1 to 0.2 μm . We attribute the observed enhancements to increased internal fields due to electromagnetic structure resonances in the medium at the incident and scattered wavelengths. Structure resonances of this type are well known in the case of elastic and inelastic scattering from small, low-index dielectric particles,^{8,9} but to our knowledge have not been observed before in high-index, lossy dielectrics like semiconductors.

Samples from which enhanced scattering has been observed include the rough edges of Si structures patterned by the complete island etch technique on silicon-on-insulator materials, ellipsoidal Si posts with $\sim 0.1\text{-}\mu\text{m}$ radii of curvature formed by etching a bulk Si wafer for several hours in a CF_4 plasma reactor, 0.1- to 0.2- μm diameter Si spheroids on a silica substrate formed by strip-heater annealing a CVD Si film, and a 0.32- μm -period rectangular grating cut $\sim 1.0\text{-}\mu\text{m}$ deep into a bulk Si substrate. The spectra from these samples are generally undistorted, i.e., Lorentzian lineshapes with widths

comparable to that of good-quality bulk Si, but observed signals are generally of the order of 4 to 20 times the scattering observed from bulk Si under identical experimental conditions. Actual enhancements may be larger, however, depending on the volume of the roughened Si responsible for the increased scattering. For example, the Si spheroids on a silica substrate were formed from a 500-Å-thick Si film and yielded intensities up to 10 times that from bulk Si in which the absorption depth is 0.75 μm . Therefore, the enhancement in Raman signal normalized to scattering volume is on the order of 100.

There are two major differences between this enhanced scattering and that observed in the case of surface-enhanced Raman scattering (SERS) from molecules adsorbed on roughened metallic surfaces.¹⁰ First, Raman scattering from Si is a bulk effect so that the entire Si volume, not just a thin surface layer, contributes to the Raman signal; and second, Si exhibits dielectric optical properties in the visible. Therefore, the large field enhancements associated with localized dipolar plasmon resonances in metallic structures with dimensions much less than a wavelength are not a factor in the present measurements.

Because of the high refractive index of Si, 0.1 μm corresponds to about an optical wavelength (0.488 μm) in the medium. In this case, the coupling between the internal and external electromagnetic fields can be greatly enhanced because of excitation of internal cavity-like modes in the Si structures. Preliminary verification of this picture can be obtained from standard Mie theory for elastic scattering from dielectric spheres.^{11,12} Figure 2-5 shows the elastic scattering efficiency factor (Q_{sca} = scattering cross section divided by the geometric cross section of the sphere) and the absorption efficiency factor (Q_{abs} = absorption cross section divided by the geometric cross section of the sphere) for Si spheres (complex refractive index, $n = 4.2 - 0.053i$) up to 1.0 μm in diameter for an incident wavelength of 0.488 μm . Peaks in the scattering efficiency indicate increased coupling of the incident and scattered fields with the Si particle. Although this calculation does not include inelastic scattering, the peaks in the absorption efficiency for particles of 0.1- to 0.2- μm diameter indicate

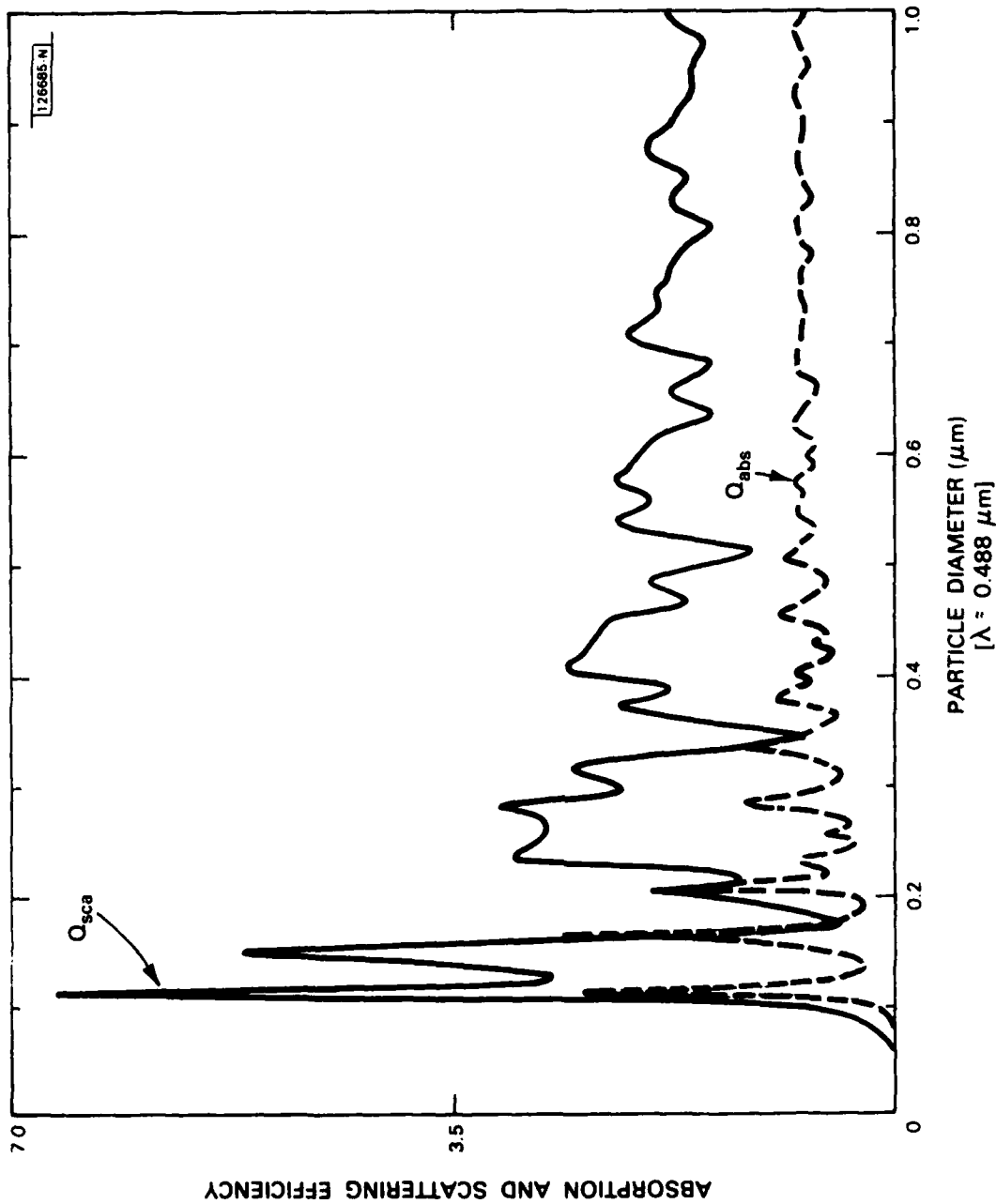


Fig. 2-5. Elastic scattering efficiency factor Q_{sca} and absorption efficiency factor Q_{abs} as a function of sphere diameter for light of wavelength 0.488 μm incident on Si spheres (refractive index $n = 4.2 - 0.053i$).

enhancement of the internal field that would lead to enhanced inelastic scattering.¹³ Because Si is relatively lossy in the visible, the resonances are broad enough to result in enhancement of both the coupling of the incident laser field ($\lambda = 0.488 \mu\text{m}$) into the particle and of the coupling of the Raman scattered field ($\lambda = 0.501 \mu\text{m}$) out of the particle.¹⁴ Additional calculations appropriate for scattering from two-dimensional structures, such as the Si grating, are currently under way.

D.V. Murphy
S.R.J. Brueck

2.4 SURFACE PHOTOACOUSTIC WAVE SPECTROSCOPY

Direct detection of the surface acoustic waves (SAWs) generated upon relaxation of energy optically absorbed in surface films has been used to measure surface absorption spectra. This technique is an extension of pulsed photoacoustic spectroscopy, which has been shown¹⁵ to provide a sensitive technique for measuring weak absorptions in bulk media, and is well suited to the study of surface effects since SAW detectors are relatively insensitive to bulk acoustic waves and the different velocities for the surface and bulk acoustic waves allow further discrimination against bulk effects.

The technique has been demonstrated by measuring the absorption spectra of monolayer-coverage Rhodamine 590 films on crystal quartz substrates using a pulsed dye laser as the excitation source and a broad-band edge-bonded LiNbO_3 transducer as the SAW detector.¹⁶ Submonolayer sensitivities have been obtained for sample areas smaller than $5 \times 10^{-4} \text{ cm}^{-2}$ at laser energies of less than $100 \mu\text{J/pulse}$. This corresponds to the detection of fewer than 10^{11} molecules which absorb less than 10^{-5} of the laser energy.

Figure 2-6 shows the measured surface photoacoustic spectrum for an approximately monolayer thick dye film on quartz. The film was fabricated by immersing the quartz substrate in a 10^{-4} molar Rhodamine 590 ethanol solution for approximately 1/2 hour and slowly pulling the substrate from the dye solution. The absorption of the dye film on a glass witness slide pulled at

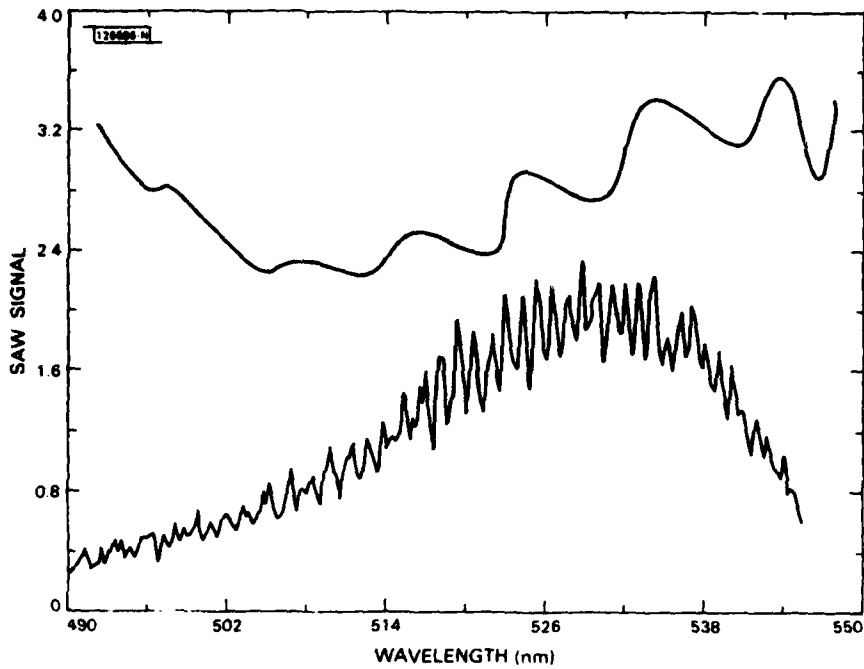


Fig. 2-6. Surface photoacoustic spectrum of an approximately monolayer thick Rhodamine 590 dye film on a crystal quartz substrate.

the same time was monitored in transmission. An absorbance of $\sim 3 \times 10^{-3}$ was measured at 535 nm, the peak of the Rhodamine 590 absorption band. This procedure has previously been reported to give nearly monolayer coverage films.¹⁷ The laser energy was limited to only $\sim 100 \mu\text{J}/\text{pulse}$ in order to avoid laser-induced desorption of the dye molecules. The sensitivity of the surface photoacoustic technique will be significantly higher for more tightly bound adsorbate-surface systems such as deposited films of metals and insulators.

The laser-induced desorption of the dye molecules can be studied by monitoring the decay of the SAW signal as a function of the number of laser pulses. Figure 2-7 shows the decay of the SAW signal measured at a laser wavelength of 520 nm, an energy intensity of $0.1 \text{ J}/\text{cm}^2$, and a 10-Hz repetition rate. The observed decay of the SAW signal is exponential and corresponds to a decay constant of $4 \times 10^{-2} \text{ s}^{-1}$ or to an effective desorption

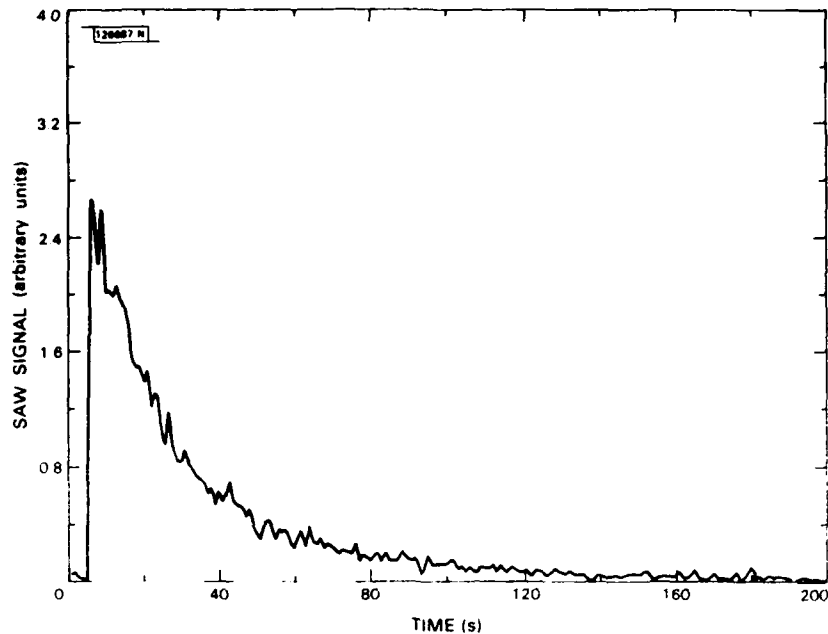


Fig. 2-7. SAW signal vs time for a Rhodamine 590 dye film on a quartz substrate. Decay is due to laser-induced desorption. Energy density was 0.1 J/cm^2 at 520 nm, and pulse repetition rate was 10 Hz.

cross section of $\sim 5 \times 10^{-21} \text{ cm}^2$, which should be compared with an absorption cross section of $\sim 4 \times 10^{-16} \text{ cm}^2$ (Ref. 18). Thus, the effective desorption probability for a dye molecule which absorbs a photon at 520 nm is $\sim 1 \times 10^{-5}$. This value of the desorption probability is highly dependent on the local conditions within the film, and is strongly affected by the presence of additional molecular species which can serve to more strongly bond the dye molecule to the surface. For example, adding a 10^{-4} molar concentration of polystyrene to the dye-ethanol solution causes the desorption probability to decrease by several orders of magnitude because of the polystyrene matrix encapsulating the dye molecules. Further work in measuring these desorption probabilities and spectra will add considerably to the present understanding of optical and thermal desorption of physisorbed adsorbate/substrate systems.

The extension of these measurements to nonlinear absorption, and specifically to surface vibrational spectroscopy by two-photon difference-frequency absorption, offers the potential of a sensitive surface vibrational spectroscopy that can be applied, at room temperature and in complex environments, to in situ measurement of a wide range of adsorbate-surface systems.

S.R.J. Brueck
T.F. Deutsch
D.E. Oates

2.5 PHOTODEPOSITION OF Ti AND APPLICATION TO DIRECT-WRITING OF Ti:LiNbO₃ WAVEGUIDES

In laser photodeposition, a tightly focused UV-laser beam can photodecompose metal- or semiconductor-bearing molecules at a surface, and thereby directly write a localized thin metal or semiconductor film.¹⁹⁻²¹ Here, the first application of this process to the fabrication of Ti-indiffused LiNbO₃ optical waveguides is described. For this application, the technique has been extended to photodeposition of Ti by surface-catalyzed photolysis of adsorbed TiCl₄. The mechanism of the photochemistry is more complex than found for previously studied metal-alkyl and metal-carbonyl cases. For integrated optics, the new fabrication procedure offers two significant advantages compared with lithographic techniques: the elimination of the time-consuming mask-generation step, and the ability to vary the thickness of the Ti film along the length of the waveguide. The latter capability introduces new design possibilities into fabricating graded-index guided-wave structures.

For the results reported here, the substrates were mounted in several-millimeter-pathlength windowed vacuum cells. In order both to suppress a competing gas-phase photochemical chain reaction as well as to minimize accumulated photodeposition on the front window, the TiCl₄ pressure was kept below 0.5 Torr. On the ~15-min. time scale for the deposition of long Ti lines, it was found difficult in a static cell to avoid modest degradation of the corrosive TiCl₄; to alleviate this problem, TiCl₄ vapor was flowed at

a very slow [~ 100 cc Torr/min.] rate past the entrance/exit orifice of the cell. The substrates were translated by a scanning microscope stage driven by $0.25\text{-}\mu\text{m}/\text{step}$ computer-controlled stepping motors. Positional feedback supplied by optical encoders allows the stage to be precisely scanned at speeds up to 2.5 mm/s.

In an initial application of Ti-indiffused LiNbO_3 channel waveguides, Ti lines of $4\text{-}\mu\text{m}$ width were drawn in the Y-direction across the 12-mm length of an X-cut LiNbO_3 substrate by uniformly translating the substrate across the focus of the UV-laser beam in $0.25\text{-}\mu\text{m}$ increments. Typical scan velocities of 11 $\mu\text{m}/\text{s}$ produced Ti of ~ 350 Å thickness. Because LiNbO_3 is opaque at 257.2 nm, the thicknesses were calibrated in self-transmission by photodeposition on one of the windows of the vacuum cell. After deposition, in order to desorb any TiCl_4 remaining on the substrate before exposure to room air, the substrates were baked under an $\sim 200\text{-Torr}$ hydrogen atmosphere at 300°C for 5 min. The Ti was then diffused into the LiNbO_3 at 1000°C for 4.5 h in argon, followed by 45 min. in oxygen. Both the argon and the oxygen were bubbled through water to compensate for the effects of Li_2O outdiffusion. After the 300°C heat treatment but before the diffusion, the Ti deposit consists of a granular film (1- to $2\text{-}\mu\text{m}$ grains). This granularity does not seem to affect the external optical quality of the waveguides; after the diffusion, the swelling characteristic of Ti-indiffused guides appears very smooth, as shown in Fig. 2-8.

Following the diffusion, the end faces of the LiNbO_3 were polished and guides tested by end-fire coupling probe-laser light into the channel waveguides. Waveguide modes were excited using 0.6328- and $0.82\text{-}\mu\text{m}$ wavelength light. The $4\text{-}\mu\text{m}$ -wide channel waveguides supported two TE and two TM modes at 0.6328 μm , and one TE and one TM mode at 0.82 μm . A direct comparison with our conventionally fabricated guides of the same dimensions showed comparably high mode confinement and low surface-scattering losses. No important differences in light-guiding properties between the photodeposited and conventional guides were detected at either probe wavelength.

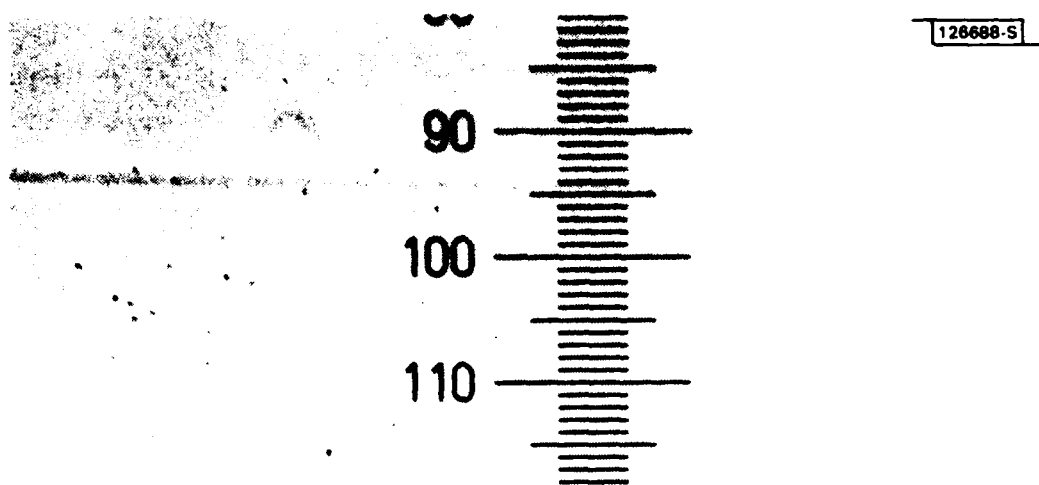


Fig. 2-8. Nomarski optical micrograph of a photodeposited waveguide in LiNbO_3 after indiffusion. Small-scale divisions are separated by $2 \mu\text{m}$.

As a potentially important extension, preliminary experiments have been made with smooth, functional variations of the laser exposure along the guides in order to fabricate graded-index structures. Such structures have several applications. For example, waveguide bend losses associated with guided-wave modulators and switches could be decreased considerably by increasing the mode confinement in the bend regions. In another example, the photodeposition technique allows one to optimize separately the guide parameters for both fiber-to-guide coupling and active device geometry by first optimizing the geometry of the active electrooptic devices and then gradually increasing both the Ti thickness and the channel width, such that at the LiNbO_3 sample edge the waveguide mode closely approximates that of the optical fiber.

J.Y. Tsao D.J. Ehrlich
R.A. Becker F.J. Leonberger

2.6 UV-LASER-INITIATED FORMATION OF Si_3N_4

The physical and electrical properties of silicon nitride grown by UV-laser-initiated deposition have been evaluated. An ArF excimer laser was used to initiate the reaction of SiH_4 and NH_3 to form Si_3N_4 .

The use of UV radiation to initiate photolytic reactions which deposit compound films at lower substrate temperatures than used with conventional chemical vapor deposition (CVD) has recently been investigated. Lamp sources have been used to deposit SiO_2 , Si_3N_4 , and other compounds on a variety of substrates.²² More recently, ArF-excimer-laser radiation has been used to deposit SiO_2 and Si_3N_4 on Si substrates.^{23,24} The ArF laser can provide several watts of power at 193 nm and thus makes possible much higher growth rates than can be obtained with lamp sources. Such low-temperature deposition has several advantages for semiconductor processing. It can reduce unwanted diffusion or chemical reactions on a semiconductor wafer, allowing deposition over metals that would react with parts of the substrate at higher temperatures. The Si_3N_4 films produced are already suitable for passivation or encapsulation purposes, but their electrical properties are not presently adequate for dielectric functions in active devices.

The ArF excimer laser was operated at 4 Hz and produced 10-ns-long pulses of ~60-mJ energy. A 40-cm focal-length BaF_2 cylindrical lens was used to focus the beam to a slit image ~2 cm wide and ~1 mm high. The beam passed less than 1 mm above the substrate used for deposition. The deposition chamber was a stainless-steel cross capable of accepting 2-in.-diam Si wafers and heating them to 600°C. Electronic-grade NH_3 and SiH_4 (10% SiH_4 in Ar) were used as reagent gases. Ultrapure Ar was used as a window purge. Mass-flow controllers were used to obtain typical gas flows of 11-sccm NH_3 , 8-sccm 10% SiH_4 in Ar, and 50- to 100-sccm Ar purge gas at a chamber pressure of ~7 Torr. The deposition rate on Si using an average 193-nm laser power of 0.2 W was ~50 Å/min. over ~7.5 cm² and was independent of temperature in the range 200° to 600°C. Films of silicon nitride grown by low-pressure chemical vapor deposition (LPCVD) at 780°C with $\text{SiH}_2\text{Cl}_2:\text{NH}_3$ (1:3) were used as comparison standards for measurements of etch rate, refractive index, and dielectric properties.

Table 2-1 shows the dependence of refractive index and etch rate on $\text{SiH}_4:\text{NH}_3$ ratio and substrate temperature. $\text{SiH}_4:\text{NH}_3$ ratios from 1:3 to 1:14 were examined; at a deposition temperature of 600°C , the refractive index varied from ~ 2.2 for the 1:3 mixes to 1.97 for the 1:14 mixes. At lower deposition temperatures, the refractive index decreased. The etch rate in 1:1 $\text{BHF}:\text{H}_2\text{O}$ for 600°C depositions compares favorably with the etch rate of 12 $\text{\AA}/\text{min.}$ obtained on 780°C LPCVD material. For lower deposition temperatures, the etch rate increases rapidly. The increase in etch rate is due to at least two factors - a decreased density, as indicated by the lower index, and increased chemical impurities, probably hydrogen, in the low-temperature material.

TABLE 2-1 PROPERTIES OF LASER-DEPOSITED Si_3N_4 FILMS AS A FUNCTION OF SUBSTRATE TEMPERATURE AND $\text{SiH}_4:\text{NH}_3$ RATIO			
Substrate Temperature ($^\circ\text{C}$)	$\text{SiH}_4:\text{NH}_3$ Ratio	Refractive Index	Etch Rate ($\text{\AA}/\text{min.}$) 1:1 $\text{BHF}^*:\text{H}_2\text{O}$
600	1:4	2.21	50
500	1:4	2.10	130
400	1:4	1.9 to 2.2	3200
780 (LPCVD)	-	2.003	12
600	1:14	2.00	90
505	1:14	1.93	380
400	1:14	1.94	5500
310	1:14	1.90	-

*1 vol. HF (49%) to 5 vol. NH_4F (40%)

The dielectric properties of the nitride were evaluated by performing capacitance-voltage (C-V) measurements on capacitors made by evaporating an Al film onto nitride films deposited on n-Si substrates and photolithographically patterning it into dots. The Al film was subsequently sintered at 400°C (15 min. in N₂).

The results of a number of C-V measurements on nitride deposited at 305° and 600°C indicated flatband voltages V_{FB} in excess of -24 V, and interface state densities Q_s in excess of $5.5 \times 10^{12} \text{ cm}^{-2}$. The large flatband voltage indicates a high density of fixed charge in the dielectric. In order to determine the role of the initial surface conditions on the dielectric properties of the material, two different surface preparation treatments were used. In one case, the native oxide was removed by an HF etch just before loading the sample into the deposition chamber; in the other, ~15 Å of oxide was grown on the wafer in order to simulate the surface oxide found to form on wafers during the initial portion of the low-pressure CVD growth process. No correlation between either V_{FB} or Q_s and either substrate temperature or initial surface condition was found. For comparison, C-V measurements on LPCVD material show V_{FB} in the range from 0 to 1 V and $Q_s = 1$ to $5 \times 10^{11} \text{ cm}^{-2}$. The large flatband voltage indicates a high density of fixed charge in the dielectric. Secondary ion mass spectrometry (SIMS) measurements indicated a mass 23 (Na) level, concentrated at the Si-Si₃N₄ interface, in the 600°C laser film at least ten times that in LPCVD material. This suggests that Na incorporated into the film during the deposition process may be responsible for the high levels of fixed charge observed in the material.

Measurements of breakdown strength for films deposited at temperatures of 500° and 600°C, made using an I-V curve tracer, gave breakdown values of 3.5 to 5 MV/cm, adequate for inter-level insulator applications.

UV-laser-initiated deposition of Si₃N₄ films can be used to produce films at temperatures lower than those used in LPCVD. Although the stoichiometry and physical properties of films can be comparable with those of LPCVD films, the dielectric properties of the material are presently not

adequate for device purposes. Nevertheless, the films may already be useful for low-temperature encapsulation or passivation of devices.

T.F. Deutsch
D.J. Silversmith
R.W. Mountain

REFERENCES

1. Solid State Research Report, Lincoln Laboratory, M.I.T. (1981:3), pp. 15-20, DTIC AD-A12696/0.
2. S. Sugano, Y. Tanabe, and H. Kamimura, Multiplets of Transition-Metal Ions In Crystals (Academic Press, New York, 1970).
3. M.D. Sturge et al., J. Chem. Phys. 54, 405 (1971).
4. Solid State Research Report, Lincoln Laboratory, M.I.T. (1981:3), p. 41, DTIC AD-A12696/0.
5. D. Welford and A. Mooradian, Appl. Phys. Lett. 40, 865 (1982).
6. _____, Appl. Phys. Lett. 40, 560 (1982), DTIC AD-A121778.
7. C.H. Henry, IEEE J. Quantum Electron. QE-18, 259 (1982).
8. A. Ashkin and J.M. Dziedzic, Phys. Rev. Lett. 38, 1351 (1977).
9. R.E. Benner, P.W. Barber, J.F. Owen, and R.K. Chang, Phys. Rev. Lett. 44, 475 (1980).
10. See, for example, Surface Enhanced Raman Scattering, R.K. Chang and T.E. Furtak, Eds. (Plenum Press, New York, 1982).
11. M. Kerker, The Scattering of Light and Other Electromagnetic Radiation (Academic Press, New York, 1969).
12. J.V. Dave, "Subroutines for Computing the Parameters of the Electromagnetic Radiation Scattered by a Sphere," IBM Report No. 320-3237 (1968).
13. G.J. Rosasco and H.S. Bennett, J. Opt. Soc. Am. 68, 1242 (1978).
14. H. Chew and D.-S. Wang, Phys. Rev. Lett. 49, 490 (1982).

15. C.K.N. Patel and A.C. Tam, Rev. Mod. Phys. 53, 517 (1981) and references therein.
16. D.E. Oates and R.A. Becker, Appl. Phys. Lett. 38, 761 (1981), DTIC AD-A103292/9.
17. G. Ritchie and E. Burstein, Phys. Rev. B 24, 4843 (1981).
18. K.H. Drexhage in Dye Lasers, F.P. Schafer, Ed. (Springer-Verlag, Berlin, 1973), p. 168.
19. D.J. Ehrlich, R.M. Osgood, Jr., and T.F. Deutsch, IEEE J. Quantum Electron. QE-16, 1233 (1980), DTIC AD-A101086/7.
20. J.Y. Tsao, D.J. Ehrlich, D.J. Silversmith, and R.W. Mountain, IEEE Electron Device Lett. EDL-3, 164 (1982).
21. D.J. Ehrlich, R.M. Osgood, Jr., and T.F. Deutsch, J. Vac. Sci. Technol. 21, 23 (1982).
22. H.M. Kim, S.S. Tai, S.L. Groves, and K.L. Schuegraf, in Proceedings of the Eighth International Conference on Chemical Vapor Deposition (Electrochemical Society, Pennington, New Jersey, 1981), Vol. 81-7, p. 258.
23. G.A. Roche, P.K. Boyer, and G.J. Collins, Technical Digest of the Conference on Laser and Electro-Optics, CLEO '82 (Optical Society of America, Washington, DC, 1982), p. 20, paper WE-2.
24. T.F. Deutsch, D.J. Silversmith, and R.W. Mountain (to be published in Proceedings of the 1982 Materials Research Society Meeting, Symposium I).

3. MATERIALS RESEARCH

3.1 TOTAL-DOSE RADIATION EFFECTS ON SOI/CMOS INVERTERS FABRICATED IN ZONE-MELTING-RECRYSTALLIZED Si FILMS

Silicon-on-insulator (SOI) devices fabricated in thin Si films on SiO₂-coated Si substrates are of great interest as potential elements for high-density and high-speed integrated circuits. Because of their isolation from the Si substrate, such devices are less affected than bulk Si devices by transient currents due to ionizing radiation, and they are also less susceptible to radiation-induced latch-up and soft errors. Therefore, SOI devices should be useful as components for radiation-hardened integrated circuits. However, like bulk MOS devices, SOI/MOS devices still confront the problem of threshold shifts produced by ionizing radiation. In addition, SOI devices can be degraded by radiation-induced leakage current, which is caused by back-channel conduction due to positive charge trapping at the interface between the Si film and the SiO₂ layer underneath.

For n-channel SOI/MOSFETs, it has recently been demonstrated^{1,2} that the effects of charge trapping in the lower SiO₂ layer can be largely suppressed by applying a negative bias to the Si substrate during irradiation. In experiments with a bias voltage of -15 V, subthreshold leakage currents of less than 0.2 pA/μm (channel width) were obtained¹ for n-channel SOI/MOSFETs subjected to ionizing doses up to 10⁶ rad(Si). In the present investigation, we have extended the study of radiation effects to SOI/CMOS devices, which were tested in the inverter configuration. Optimum results were obtained with a -5-V substrate bias, which yielded low subthreshold leakage currents for both n- and p-channel devices.

Applying a negative bias to the Si substrate during irradiation of SOI/MOSFETs can reduce the quantity of radiation-induced positive charge trapped at the lower Si-SiO₂ interface and also counteract the tendency of this charge to induce an n-type inversion layer in the Si film.^{1,2} Therefore, the effect of ionizing radiation on the leakage current of n-channel devices can be greatly reduced. For p-channel SOI/MOSFETs, however, a

negative substrate bias can have two adverse effects on device characteristics in the absence of radiation. First, a depletion region will be formed at the back channel, which can result in space-charge interaction with the front channel and cause a shift in threshold voltage. Second, for sufficiently large negative substrate bias, a weak inversion layer will be formed at the lower Si-SiO₂ interface that can lead to an increase in subthreshold leakage current. Furthermore, irradiation actually tends to improve the performance of p-channel devices because their leakage current is decreased by positive charge trapped at the lower Si-SiO₂ interface; applying a negative substrate bias can reduce this beneficial effect. Consequently, to utilize negative substrate biasing for protecting SOI/CMOS devices against ionizing radiation, we must determine an optimum bias voltage for the combined performance of the n- and p-channel devices.

Our CMOS devices were fabricated in 0.5- μm -thick Si films obtained by using the graphite strip-heater technique³ for zone-melting recrystallization of poly-Si on 1- μm -thick SiO₂ layers on Si substrates. The fabrication process has been described elsewhere.⁴ The devices have a poly-Si gate and self-aligned ion-implanted source and drain. The gate width is 20 μm , the gate length 5 μm , and the gate oxide thickness 80 nm. No attempt was made to prepare radiation-hardened oxide. Before irradiation the individual n- and p-channel devices were well behaved, with field-effect mobilities of ~ 600 and 250 cm²/V-s for electrons and holes, respectively, and subthreshold leakage currents of less than 0.05 pA/ μm (channel width).

For radiation testing, pairs of n- and p-channel devices were connected in the CMOS inverter configuration, as shown in Fig. 3-1, and exposed to doses of 1.5-MeV electrons corresponding to ionizing doses from 10³ to 10⁶ rad(Si). The bias voltages during irradiation were $V_{DD} = 5$ V, $V_{IN} = 0$ or 5 V, and $V_B = 0, -5, -7.5, \text{ or } -10$ V, where V_{DD} is the supply voltage and V_{IN} is the input voltage. Subthreshold leakage current and threshold voltage measurements were performed within 20 min. after exposure. In all cases, the V_B value was the same during the measurements as during irradiation.

For inverters with $V_B = 0$, large n-channel leakage currents ($> 10^{-8}$ A) were observed after irradiation to doses of 10⁵ rad(Si) or above, while

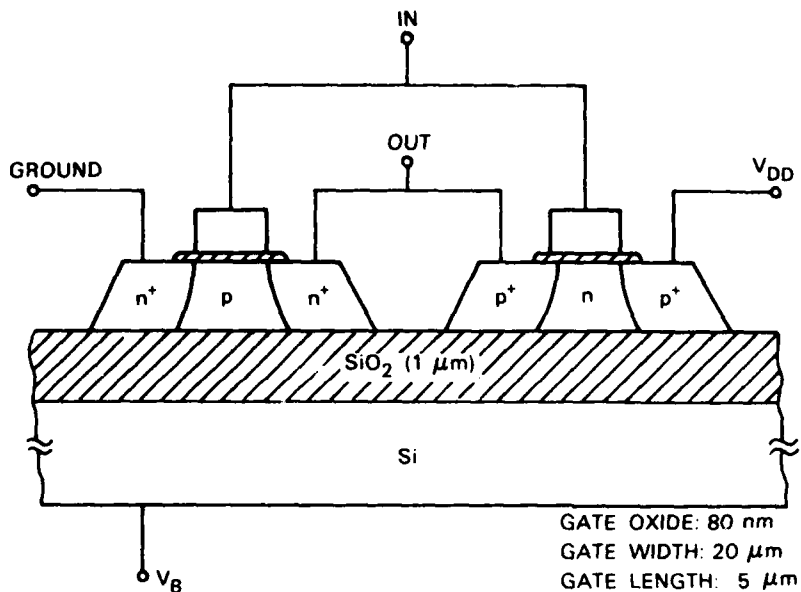


Fig. 3-1. Schematic structure of SOI/CMOS inverter fabricated in zone-melting-recrystallized Si film on SiO_2 -coated Si substrate.

there was no increase in p-channel leakage current. On the other hand, for $V_B = -7.5$ or -10 V, the n-channel leakage current remained low after irradiation but the p-channel leakage current was 2 to 3 orders of magnitude higher than for $V_B = 0$. Best results were obtained with $V_B = -5$ V. Figure 3-2 shows the subthreshold characteristics of n- and p-channel devices with $V_{IN} = 0$ V and $V_B = -5$ V before and after irradiation. Leakage currents of less than 0.1 pA/ μm (channel width) were observed for both devices up to 10^6 rad(Si) dose. For inverters with $V_{IN} = 5$ V and $V_B = -5$ V, so that the n-channel devices were in the ON state and the p-channel devices were in the OFF state, the results are shown in Fig. 3-3. Both n- and p-channel leakage currents remained low after 10^5 rad(Si); after 10^6 rad(Si), there was a large increase in n-channel leakage current but hardly any change in p-channel leakage current.

Another effect of ionizing radiation is a shift of threshold voltage (V_T) to a more negative value due to charge trapping in the gate oxide. In

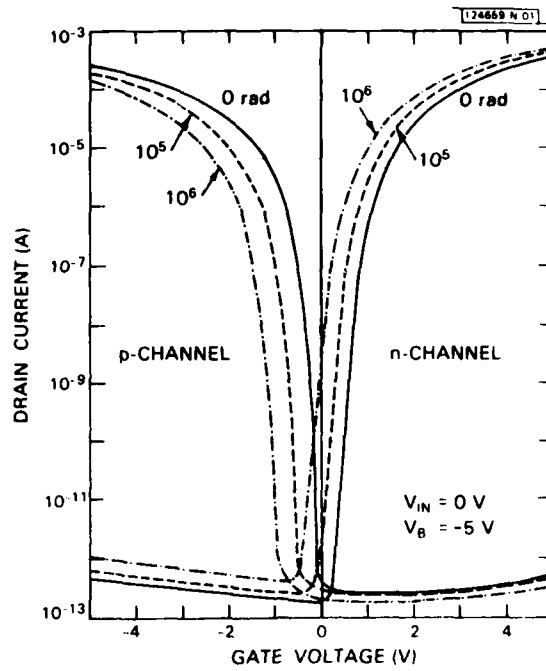


Fig. 3-2. Subthreshold characteristics of n- and p-channel devices biased with $V_{IN} = 0\text{ V}$ and $V_B = -5\text{ V}$ before and after irradiation of SOI/CMOS inverters.

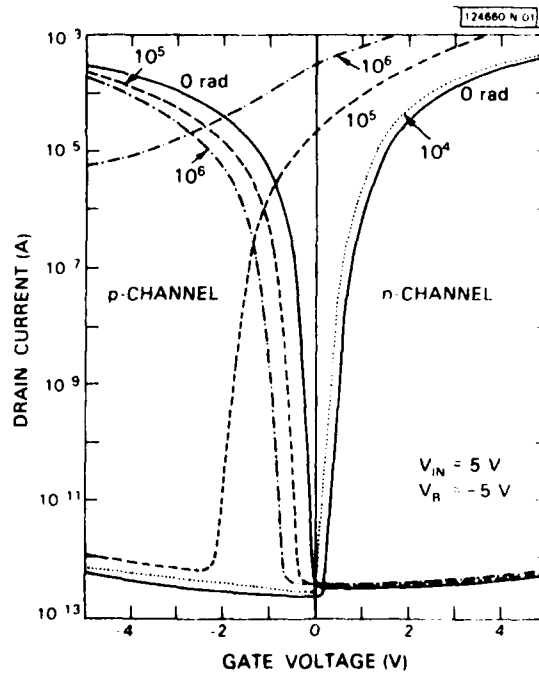


Fig. 3-3. Subthreshold characteristics of n- and p-channel devices with $V_{IN} = 5\text{ V}$ and $V_B = -5\text{ V}$ before and after irradiation.

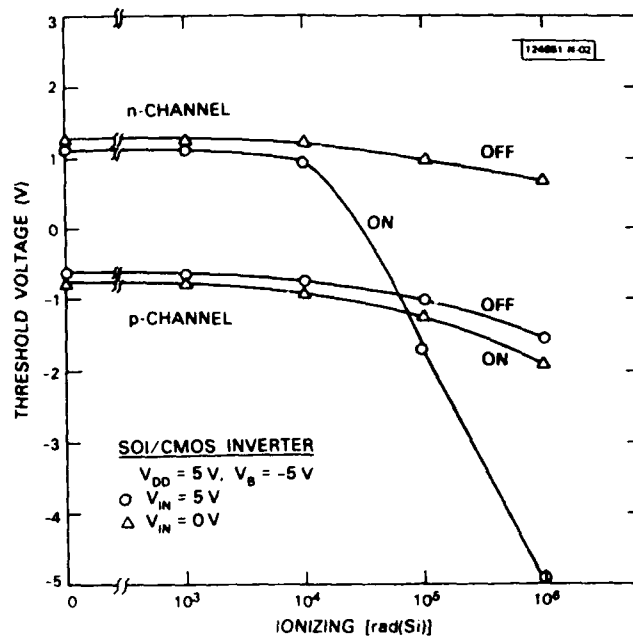


Fig. 3-4. Threshold voltage of n- and p-channel devices as a function of ionizing dose.

Fig. 3-4, V_T is plotted as a function of ionizing dose for n- and p-channel devices with $V_B = -5V$. After 10^6 rad(Si), the p-channel devices show a shift in V_T of approximately -1 V regardless of their input state during irradiation. For n-channel devices, the V_T shift was only $\sim 0.6V$ when the devices were in the OFF state. However, a dramatic shift in V_T occurred for n-channel devices in the ON state ($V_{IN} = 5V$). This shift results from the trapping of positive charge at the gate SiO_2 -Si interface due to the positive gate bias.

The sensitivity of V_T to ionizing radiation depends on the properties of the gate oxide. The very large V_T shift observed for n-channel devices in the ON state is believed to be a consequence of degradation of the oxide during device fabrication, since penetration of phosphorous ions through the poly-Si gate into the gate oxide frequently occurs during the n-channel source and drain implant.^{5,6} By decreasing the ion-implantation energy and/or increasing the poly-Si thickness it should be possible to reduce or

eliminate the oxide degradation and, thus, to markedly reduce the shift in V_T . If a negative substrate bias is applied, the other characteristics of the present SOI/MOS devices are relatively insensitive to ionizing radiation. We therefore believe that a radiation-hardened SOI/CMOS technology based on zone-melting recrystallization can be developed for achieving high packing density and high-speed operation.

B-Y. Tsaur D.J. Silversmith
J.C.C. Fan R.W. Mountain
G.W. Turner

3.2 DOUBLE-CRYSTAL X-RAY DIFFRACTOMETRY FOR CHARACTERIZING III-V MATERIALS

Double-crystal x-ray diffractometry utilizes successive Bragg reflections from two single crystals to achieve much higher angular resolution than can be obtained by conventional diffractometry employing only one crystal. In initial experiments with a recently installed double-crystal diffractometer, we have been taking advantage of this increased resolution to examine two aspects of the liquid-phase epitaxy (LPE) of GaInAsP layers on InP substrates: the surface quality of InP wafers and the epilayer-substrate lattice mismatch.

For surface characterization, two (100)-oriented InP crystals in the nondispersive configuration (i.e., with their diffracting planes parallel) are aligned to maximize the (400) diffraction peak for CuK radiation. With one crystal fixed in the optimum position, a rocking curve is obtained by measuring the angular dependence of the diffracted intensity as the other crystal is rotated. For two perfect InP crystals, the theoretical width (full width at half maximum) of the rocking curve for the CuK (400) peak is about 9" (see Ref. 7). The measured width is sensitive to surface damage because the penetration depth for Bragg reflection is very small - only about 8 μm for this peak. In most of our experiments a sample that has been heavily etched to remove surface damage is used as the fixed crystal, and the sample to be characterized is rotated.

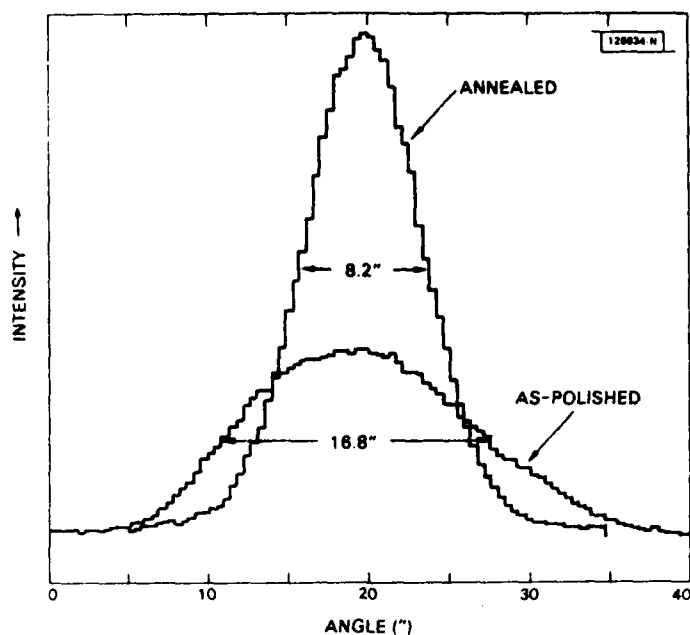


Fig. 3-5. Rocking curves for CuK (400) peak obtained by double-crystal diffractometry for an InP crystal before and after thermal annealing.

Figure 3-5 shows the rocking curves obtained before and after thermal annealing for an InP wafer that had been sliced with an I.D. diamond saw, lapped with 2- μm Al_2O_3 grit, and chemi-mechanically polished with bromine-methanol, the usual procedure for preparing LPE substrates. For the as-polished sample, the width is nearly twice the theoretical value, indicating strong surface damage. After the sample was annealed at 650°C for 1 h in a phosphine atmosphere in the LPE growth system, within experimental uncertainty the width of the peak was equal to the theoretical value, showing that the surface damage had been removed. In another experiment, the width was reduced from 45" for an as-polished sample to 25" after annealing at 350°C for only 2 min. in a N_2 atmosphere. By means of rocking-curve measurements made on repeatedly etched samples, it was found that the surface damage of as-polished wafers generally extends 20 to 40 μm below the surface, although in one case the peak width was reduced from 60" to 10" by etching off 4 μm .

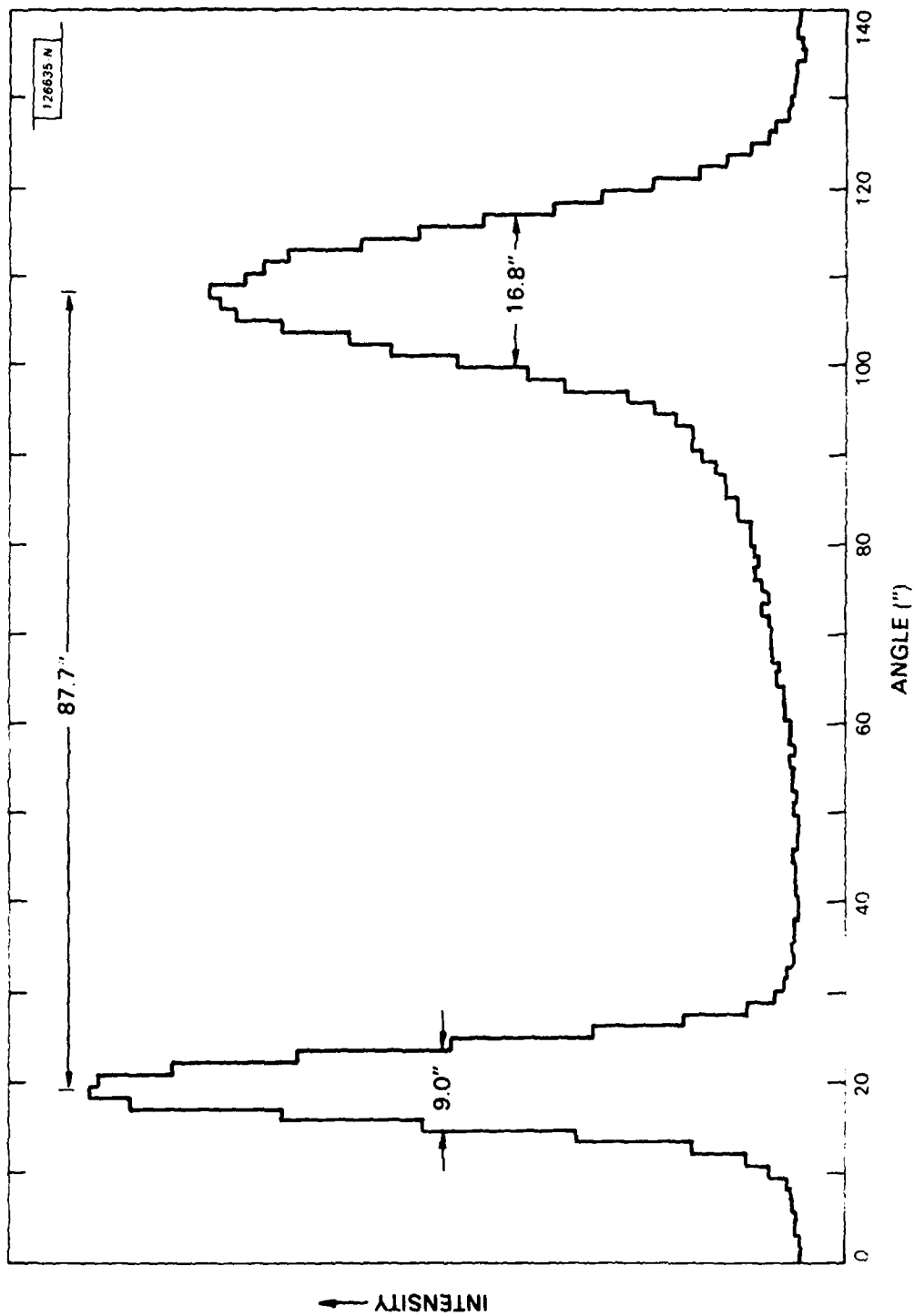


Fig. 3-6. Rocking curve for CuK (400) peak obtained by double-crystal diffractometry for a sample prepared by LPE growth of a GaInAsP layer on an InP substrate.

Matsui, Watanabe, and Seki⁷ have reported that the width of experimental rocking curves for the $\text{CuK}\alpha_1$ (400) reflection from InP shows a marked dependence on the dislocation density. Their measured widths increased from 12 to 13" for negligible etch-pit density to 32" for an etch-pit density of $5 \times 10^4 \text{ cm}^{-2}$. However, we have obtained half-widths of 9 to 10" for heavily etched samples with etch-pit densities even greater than 10^5 cm^{-2} . We conclude that double-crystal diffractometry is not an effective method for characterizing dislocation density in InP. However, we believe that double-crystal x-ray topography should be useful for this purpose, and we have initiated experiments using this technique. (Since Matsui, Watanabe, and Seki⁷ did not measure widths below 12", their results could be explained by assuming that they did not etch their samples sufficiently to remove all the work damage and that the work damage increased with increasing dislocation density.)

To determine the lattice mismatch between an LPE GaInAsP layer and its InP substrate, one can obtain a double-crystal rocking curve with a heavily etched InP sample again used as one crystal and the GaInAsP/InP sample used as the other. The curve will contain separate peaks for the epilayer and the substrate if the mismatch - defined as $(a_{\text{GaInAsP}} - a_{\text{InP}})/a_{\text{InP}}$ - is greater than the change in lattice spacing corresponding to the width of the broader peak. Figure 3-6 shows such a rocking curve, which was obtained for the $\text{CuK}\alpha$ (400) diffraction from a sample with an epilayer about 2 μm thick whose composition was determined by luminescence measurements to be $\text{Ga}_{0.27}\text{In}_{0.73}\text{As}_{0.63}\text{P}_{0.37}$. The narrower peak is due to diffraction from the substrate. Within experimental uncertainty its width is equal to the theoretical value for InP, presumably because any work damage was removed by thermal annealing during the LPE growth run. According to a simplified calculation, which neglects local differences in lattice spacing associated with alloying, the theoretical peak width for the GaInAsP alloy is close to the value for InP. The measured peak for the epilayer is considerably broader, perhaps because of compositional inhomogeneity in the layer or possibly because of the inaccuracy of the theoretical calculation.

If no correction is made for strain in either the epilayer or the substrate, the lattice mismatch calculated from the separation between the two diffraction peaks in Fig. 3-6 is -6.8×10^{-4} . Since the thermal expansion coefficient is larger for the GaInAsP alloy than for InP, the mismatch at the LPE growth temperature (650°C) was only about one-fourth this value. For the epilayer peak width shown in Fig. 3-6, a lattice mismatch as small as 1×10^{-4} could be measured by double-crystal diffractometry using the $\text{CuK}\alpha$ (400) reflection.

For comparison with the double-crystal results, Fig. 3-7 shows the $\text{CuK}\alpha_1$ and $\text{CuK}\alpha_2$ (600) peaks obtained with a conventional single-crystal diffractometer for the GaInAsP/InP sample of Fig. 3-6. The resolution, which is typical of single-crystal instruments, is insufficient to separate the epilayer and substrate peaks or even to yield asymmetrical broadening of the joint peaks. The smallest lattice mismatch that could be detected by this technique is greater than 10^{-3} .

M.S. Taylor
G.W. Iseler
S.H. Groves

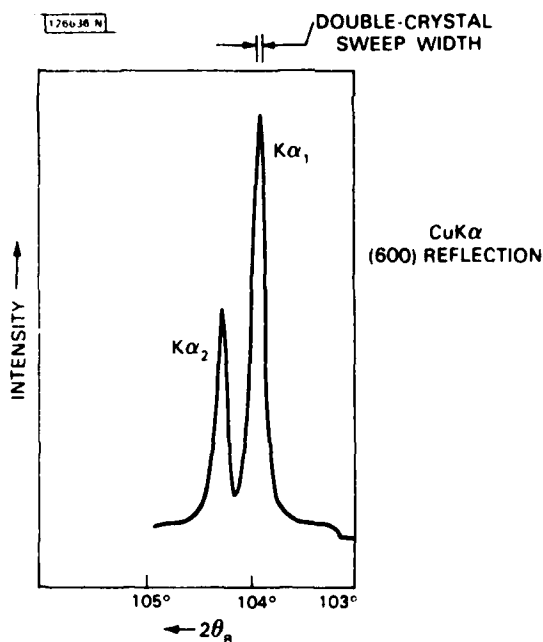


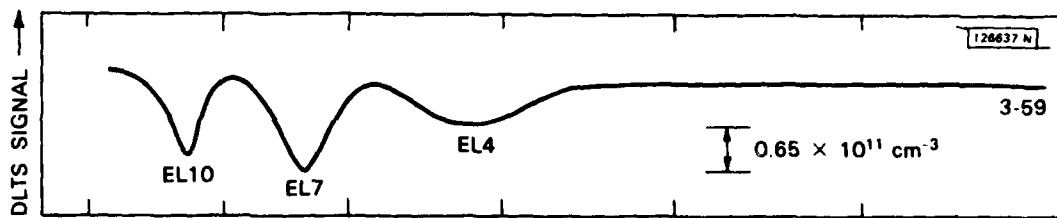
Fig. 3-7. $\text{CuK}\alpha_1$ and $\text{CuK}\alpha_2$ (600) peaks obtained by single-crystal diffractometry for GaInAsP/InP sample of Fig. 3-6.

3.3 HOLE TRAPS IN TUNGSTEN-DOPED GaAs GROWN BY MOLECULAR-BEAM EPITAXY

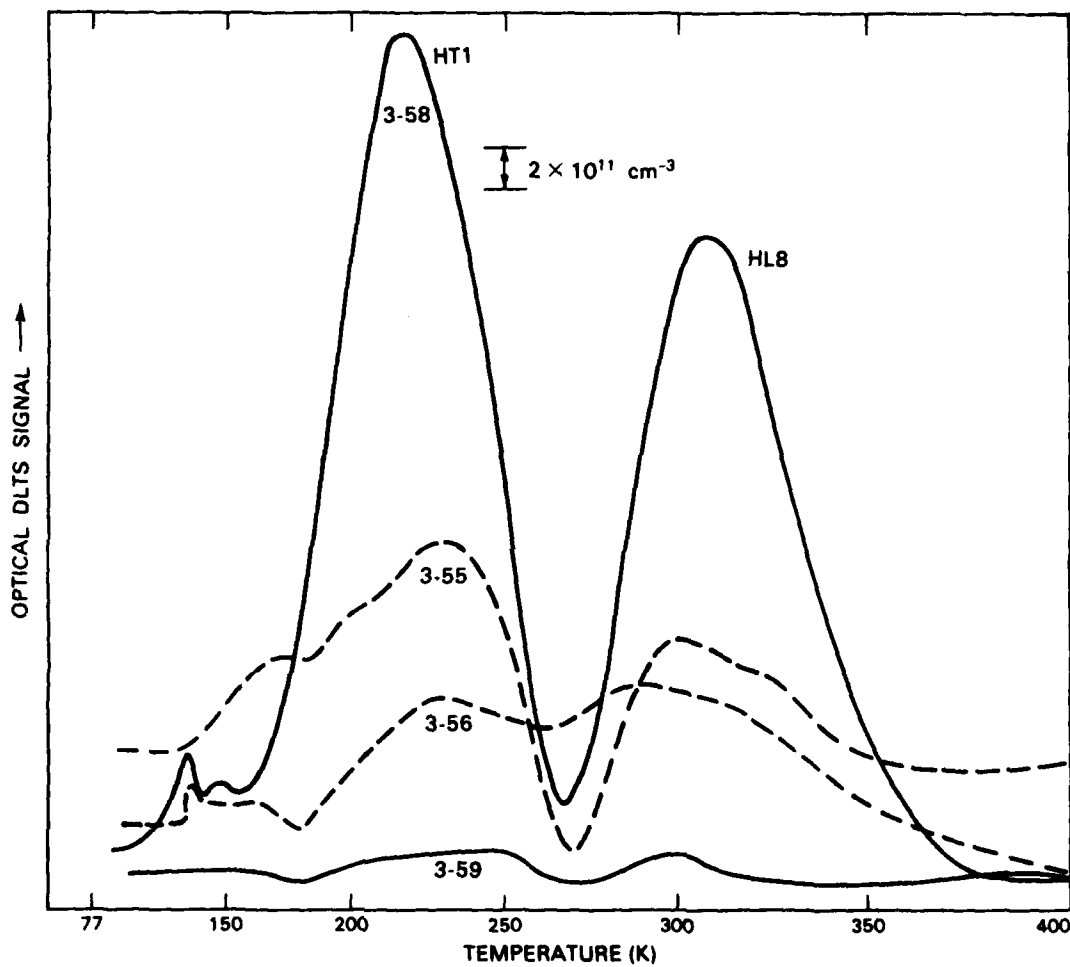
In the GaAs permeable base transistor (PBT), the base consists of a metal grating of submicrometer dimensions that is embedded in the semiconductor. In the present fabrication procedure, a tungsten base grating is formed on a single-crystal GaAs substrate and a layer of GaAs is then grown over the grating by vapor-phase epitaxy or molecular-beam epitaxy (MBE). There is a possibility that W is being incorporated into the GaAs during the overgrowth process, with deleterious effects on device performance. To investigate this possibility, a study using transient capacitance techniques has been undertaken to determine whether trapping centers due to W are being introduced into the overgrown GaAs. As the first step in this study, these techniques have been used to examine GaAs layers deposited by MBE under conditions expected to result in the incorporation of W.

The MBE GaAs layers were grown on semi-insulating <100>GaAs substrates in a vacuum chamber fitted with a W filament mounted in a liquid-N₂-cooled shroud. The substrate temperature during growth was 590°C. During three growth runs the W filament was heated electrically to temperatures of 1800° to 2200°C, as monitored with an optical pyrometer. Table 3-1 lists these temperatures and the corresponding vapor pressures of W at the filament surface. A control run was then made without heating the filament. All the layers were made n-type by doping with Si to obtain carrier concentrations close to 10¹⁴ cm⁻³.

Carrier traps in the GaAs layers were characterized by monitoring transient capacitance changes in the depletion layer of Schottky barriers prepared by Au evaporation. Deep-level transient spectroscopy (DLTS), which employs voltage pulses for trap filling, was used to detect majority-carrier (electron) traps. Both electron and hole traps were detected by optical DLTS, which employed trap-filling light pulses from an incandescent tungsten source that had been passed through an interference filter with a wavelength bandpass of 9 nm centered at 1.05 μm.



(a)



(b)

Fig. 3-8. Transient capacitance vs temperature spectra taken for MBE GaAs layers with emission time of 21.7 ms. (a) DLTS trace for control sample, showing electron traps; (b) optical DLTS traces, showing mainly hole traps.

TABLE 3-1 GROWTH CONDITIONS AND MOBILITIES FOR MBE GaAs LAYERS			
Sample	W Filament Temperature (°C)	W Vapor Pressure (Torr)	μ at 77 K (cm ² /V-s)
3-55	1800	1×10^{-11}	5.4×10^4
3-56	2000	7×10^{-10}	6.6×10^4
3-58	2200	4×10^{-8}	4.4×10^4
3-59	-	-	5.8×10^4

A typical DLTS spectrum of transient capacitance vs temperature for the control sample, obtained for an emission time of 21.7 ms, is shown in Fig. 3-8(a). It contains three peaks, which are tentatively attributed to the electron traps EL10 (0.17 eV), EL7 (0.30 eV), and EL4 (0.52 eV). The same peaks appear in the traces for the layers grown in runs made with the heated W filament; the differences in trap density from sample to sample are relatively small.

Much larger differences in trap density were revealed by the optical DLTS measurements. Representative traces for the four samples, also obtained for an emission time of 21.7 ms, are shown in Fig. 3-8(b). Although the spectra are rather broad, two principal peaks arising from hole emission appear in each trace. The peak at lower temperature is due to a hole trap with activation energy and emission cross section close to the values of HT1 (0.44 eV, 1.2×10^{-14} cm²), while the parameters for the other trap are similar to those of HL8 (0.52 eV, 3.5×10^{-16} cm²).

The most striking feature of Fig. 3-8(b) is that the three samples grown in runs when the W filament was heated have much higher densities of both principal traps than the control sample. Furthermore, trap densities are by far the highest for sample 3-58, for which the filament temperature was highest. These data strongly suggest that W was incorporated into these three samples and that its incorporation resulted in a marked increase in trap density. It should be noted, however, that the trap densities are not perfectly correlated with the filament temperature, since the densities are higher for sample 3-55 than for sample 3-56, although the filament temperatures were 1800° and 2000°C, respectively. To investigate whether this discrepancy might be due to an error in the trap-density measurements, we have examined the relationship between these densities and the electron mobilities measured at 77 K, which are listed in Table 3-1. The results are shown in Fig. 3-9, where the reciprocal of the mobility μ is plotted against the total density N_t of the two principal traps. For the three W-doped

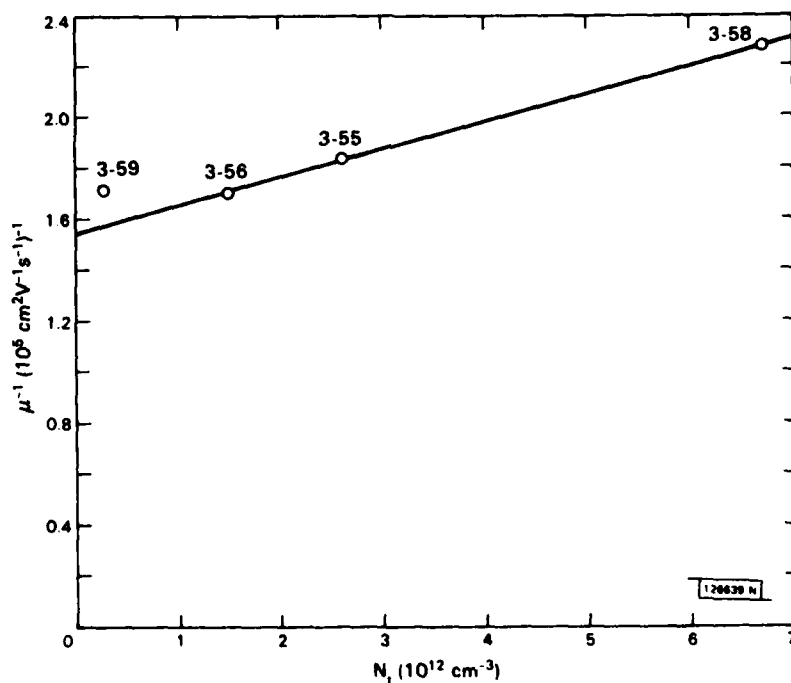


Fig. 3-9. Reciprocal of electron mobility at 77 K as a function of hole trap density for MBE GaAs layers.

samples, the data points fall on a straight line that can be represented by the expression

$$\frac{1}{\mu} = \frac{1}{\mu_0} + \frac{N_t}{C} \quad (3-1)$$

where μ_0 and C are constants. Thus, it appears that the trap-density measurements are at least relatively correct. (The expression used to determine the densities of the hole traps from the optical DLTS spectra is derived on the assumption that for these traps the optical emission rate for holes is small compared with the rate for electrons, and that the effect of free carriers near the edge of the depletion layer is negligible. Use of this expression may result in either significantly overestimating or underestimating the absolute trap densities.⁸⁾)

The results of this study indicate that the incorporation of W into GaAs can be detected by optical DLTS measurements of the densities of hole traps HT1 and HL8. Such measurements on PBT device structures could prove useful in determining whether W is incorporated during the fabrication of these devices.

J.G. Mavroides B.A. Vojak
A.R. Calawa D.F. Kolesar

REFERENCES

1. B-Y. Tsauro, J.C.C. Fan, G.W. Turner, and D.J. Silversmith, IEEE Electron Device Lett. EDL-3, 195 (1982).
2. G.E. Davis, H.L. Hughes, and T.I. Kamins, IEEE Trans. Nucl. Sci. NS-29, 1685 (1982).
3. M.W. Geis, H.I. Smith, B-Y. Tsauro, J.C.C. Fan, E.W. Maby, and D.A. Antoniadis, Appl. Phys. Lett. 40, 158 (1982), DTIC AD-A121757.
4. B-Y. Tsauro, J.C.C. Fan, R.L. Chapman, M.W. Geis, D.J. Silversmith, and R.W. Mountain, IEEE Electron Device Lett. EDL-3, 398 (1982).
5. R.K. Smeltzer, Appl. Phys. Lett. 41, 849 (1982).
6. C.P. Chang, IEEE Trans. Nucl. Sci. NS-29, 1702 (1982).
7. J. Matsui, H. Watanabe, and Y. Seki, J. Cryst. Growth 46, 563 (1979).
8. A. Mitonneau, G.M. Martin, and A. Mircea, Institute of Physics Conference Series No. 33a (Institute of Physics, London, 1977), p. 73.

4. MICROELECTRONICS

4.1 FABRICATION OF SUBMICROMETER-SIZE STRUCTURES IN Si USING SiCl_4/O_2 REACTIVE-ION ETCHING

Submicrometer-size structures have been reactive-ion etched in Si with SiCl_4/O_2 gas mixtures. Using a process first suggested by Horwitz,¹ we have found that SiCl_4/O_2 offers several advantages over Cl_2 and CF_4 as an etching gas: masking capabilities are improved, Si/SiO₂ selectivity is higher, Si etch rates are greater than 1000 Å/min., and surface damage to the Si is reduced.² Gratings of 3200-Å period, which form the active region of the Si permeable base transistor (PBT),³ have been etched with a SiCl_4/O_2 ratio of 1:1.

Figure 4-1 shows <1000-Å-wide gaps etched in Si with a SiO₂ mask. Anisotropic profiles can be achieved, and Si etches quickly (>1000 Å/min.) with the etched surfaces remaining smooth and clean. Cr, Ni, and Al may also be used as etch masks. Cr and Ni etch very slowly, while Al does not appear

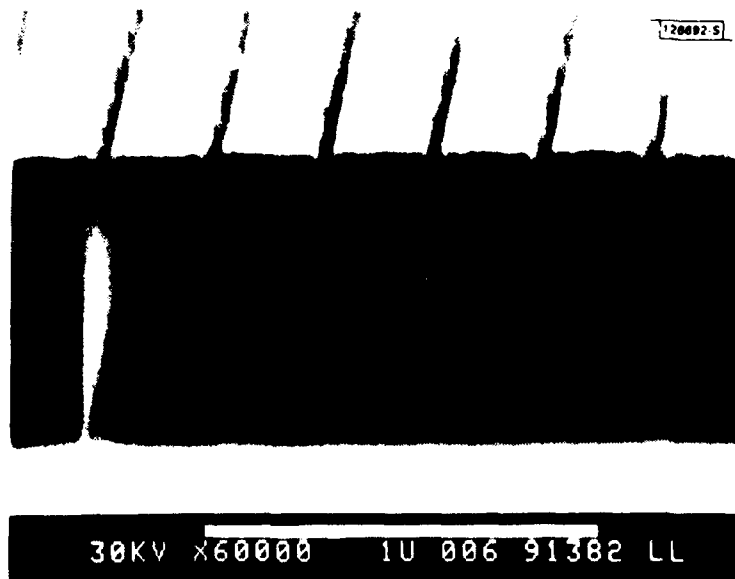


Fig. 4-1. 3200-Å-period grating reactive ion etched in 1:1 SiCl_4/O_2 .

to etch at all with 1:1 SiCl_4/O_2 , even though pure SiCl_4 has been used as an Al etching gas.^{4,5} The Si/SiO_2 selectivity is greater than 10:1 which is necessary in the fabrication of the Si PBT.

Some problems have been encountered in fabricating such small structures. When Al is used as an etch mask, a redeposition occurs on the Al surface. Because this redeposition is seen only with Al, we believe the material to be a Si-O-Al compound, rather than SiO_2 as suggested by Horwitz.¹ Figure 4-2 shows the problem caused by this redeposition. The mask gets wider during etching, causing a narrowing of the etched groove. This effect can be detrimental in the fabrication of submicrometer-size structures. However, with larger geometries ($>1 \mu\text{m}$) this effect is not significant, as shown in Fig. 4-3. In fact, the redeposition on the Al surface enhances the masking capabilities of the Al. Since Al is easier to remove than Cr or Ni, it is desirable as an etch mask for submicrometer geometries as well as for

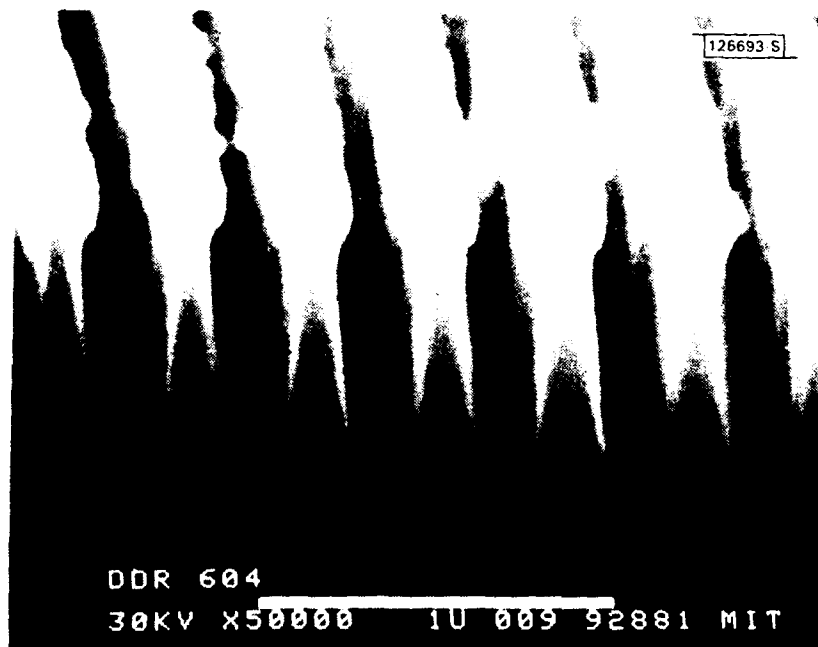


Fig. 4-2. Al-masked, 3200-Å-period grating reactive ion etched in 1:1 SiCl_4/O_2 . Redeposition on Al mask caused widening of base. Etched surface is clean and smooth.

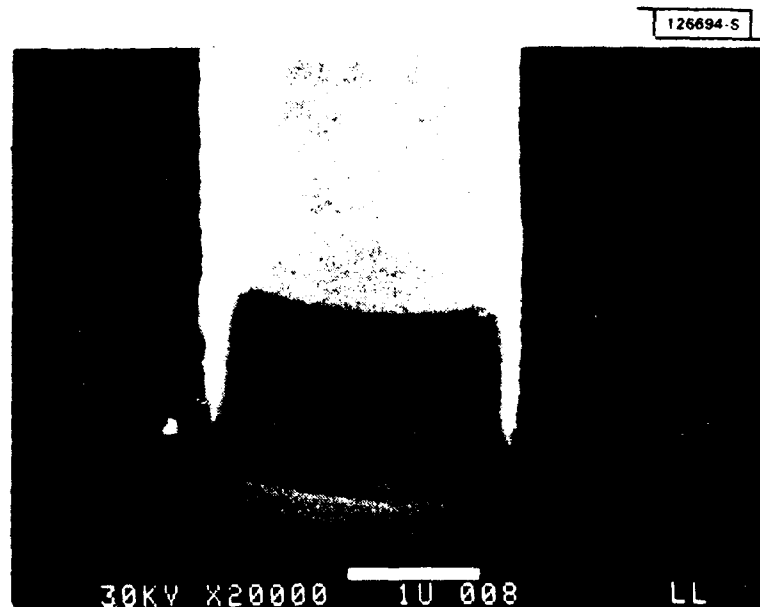


Fig. 4-3. 2- μ m-wide line reactive ion etched in 1:1 SiCl_4/O_2 . SiO_2 layer and Al mask still intact.

larger structures. Therefore, attempts are now being made to minimize this mask-widening effect by decreasing the O_2 content of the SiCl_4/O_2 etching gas.

Another difficulty with submicrometer geometry structures is encountered when etching n^+ -on- n Si. Figure 4-4 shows the excellent profile of a 3200-Å-period grating etched in n^+ Si. However, Fig. 4-5 shows the undercut profile of a larger grating etched into a substrate consisting of approximately 1 μm of n^+ Si on an n -type substrate. The undercutting is caused by the fact that the n^+ layer etches faster than the n -type substrate, and is therefore undercut when the n region is reached by the SiCl_4/O_2 etching gas. Further investigations are under way to understand and minimize this effect.

S.M. Cabral
D.D. Rathman
N.P. Economou

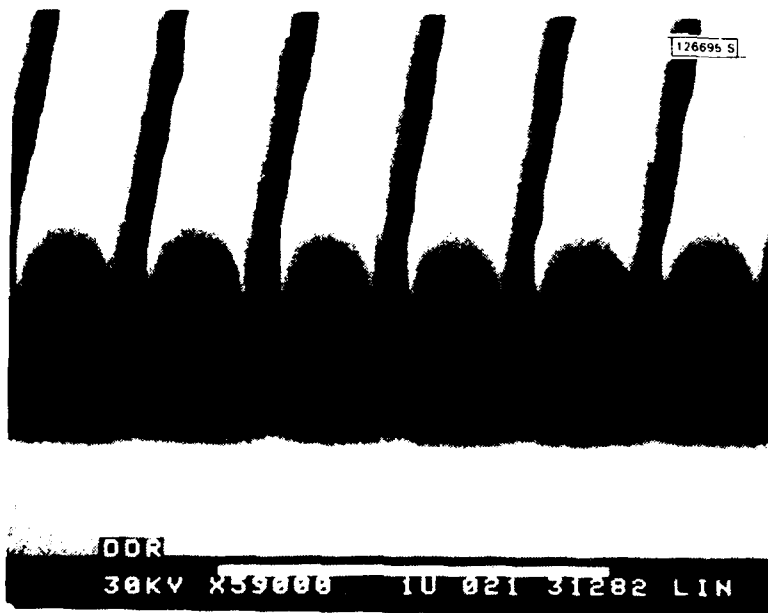


Fig. 4-4. 3200-Å-period grating reactive ion etched in 1:1 SiCl_4/O_2 with Cr mask on 1500-Å SiO_2 on n^+ -type Si. Cr mask is gone, and SiO_2 layer is rounded at edges.

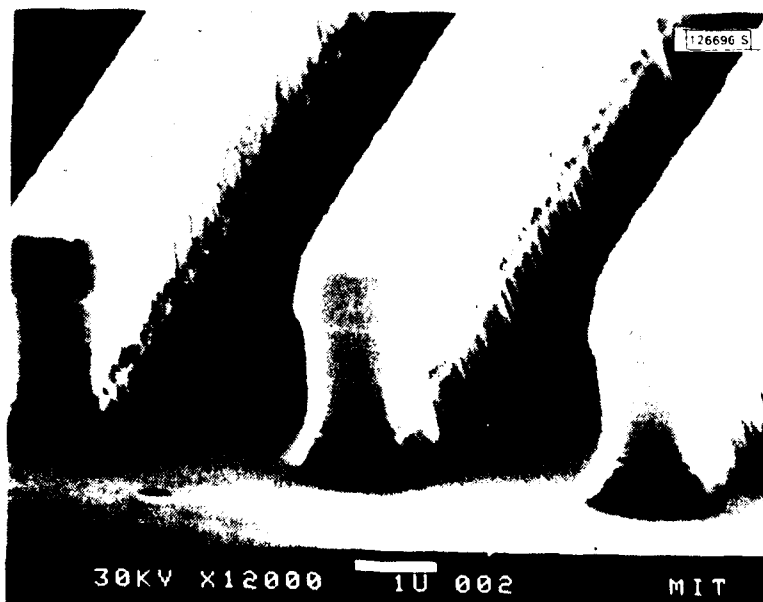


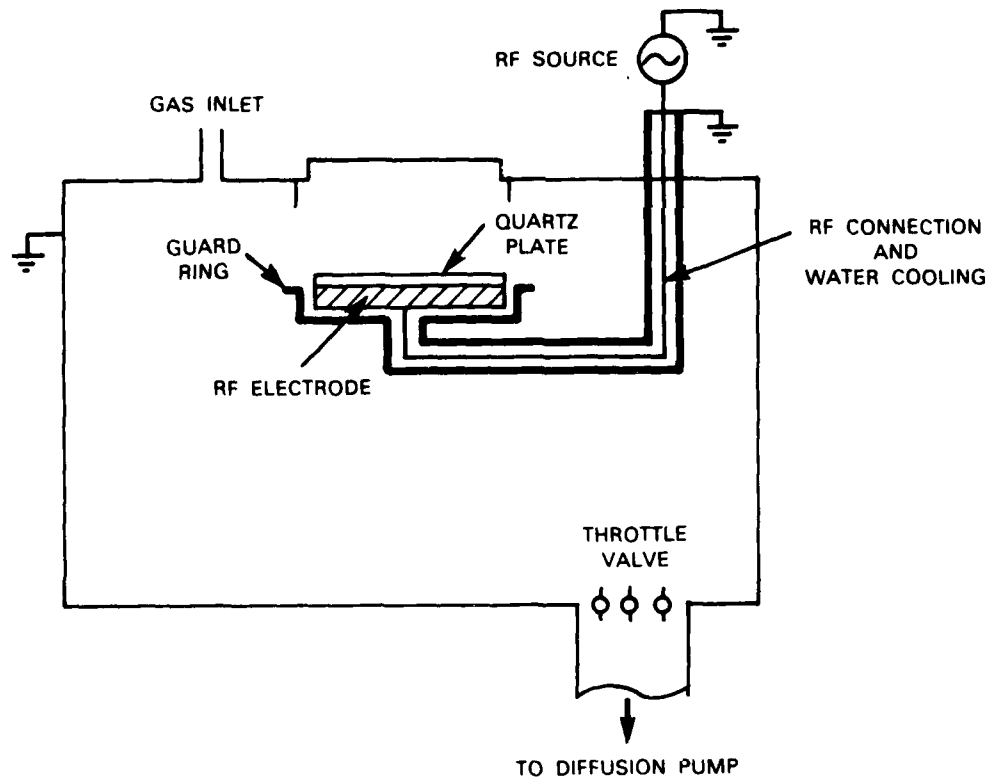
Fig. 4-5. 4- μm -period grating reactive ion etched in 1:1 SiCl_4/O_2 with SiO_2 mask on 1500-Å SiO_2 on $\sim 1\text{-}\mu\text{m}$ n^+ -on-n-type Si. Undercut of n^+ layer occurs.

4.2 THE EFFECT OF CHAMBER CONFIGURATION AND BIAS VOLTAGE ON DAMAGE INDUCED IN Si BY REACTIVE-ION ETCHING

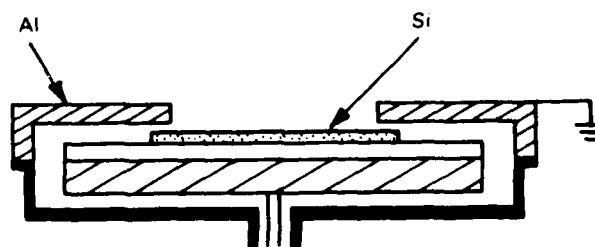
Reactive-ion etching (RIE) of a wide variety of materials such as semiconductors, dielectrics, metals, and silicides has been developed extensively during recent years.^{6,7} In addition to selectivity, etching profile, throughput, and reproducibility, an important consideration for utilizing RIE in device fabrication is the minimization of damage effects on etched materials. Our previous results² indicate that damage induced in Si by RIE or ion milling is dependent on the bias voltages and gases used during etching. Si substrates etched in carbon-containing gases (CF_4 , CHF_3) have more interface states than those etched in carbon-free gases (Cl_2 , SiCl_4 , SiF_4). Also, the degree of damage increases with bias voltage. We have recently explored the sources of RIE-related damage, in particular the effects of RIE chamber configuration and of bias voltage.

The RIE chamber used was a modified Perkin-Elmer single-target sputtering system.⁸ The basic chamber configuration, shown in Fig. 4-6(a), consisted of a stainless-steel chamber with a quartz plate on the powered electrode which was 20 cm in diameter. In a second series of experiments, contamination from nonvolatile compounds sputtered from the chamber walls was eliminated by coating the entire chamber with a layer of amorphous SiO_x by use of an RF discharge in $\text{SiCl}_4 + \text{O}_2 + \text{Ar}$. A third chamber configuration is shown in Fig. 4-6(b) where a small Si target was used. The powered electrode was reduced to an effective 10-cm diameter by placing a grounded aluminum annulus over the electrode. This change in the area ratio between the powered and the grounded electrodes also reduced the energy of ion bombardment on the chamber wall.⁹ Typically, the pressure was maintained around 10 to 20 mTorr during etching, and about 2000 Å of Si was etched in each case.

Si samples were n-type (100) substrates with resistivity of 5 to 10 Ω -cm. The samples were subjected to a standard H_2O_2 clean before and after etching. Thermal oxide about 1000 Å thick was grown on the etched Si substrates. Al was used for front and back contacts to form MOS capacitors.



(a)



(b)

Fig. 4-6. (a) Schematic diagram of reactive-ion etching chamber which consists of stainless steel with a quartz plate on powered electrode (20-cm diameter). (b) Powered electrode covered by Si and reduced to 10-cm diameter by placing a grounded aluminum annulus on top.

Interface-state densities (N_{it}) of the MOS capacitors were calculated from the measured high- and low-frequency capacitance-voltage (C-V) curves.¹⁰ In our previous study, we found that N_{it} measurements were correlated to the surface damage induced by RIE in spite of the high oxidation temperature and the Si consumption during oxide growth.

Figure 4-7 shows the generated interface-state densities as a function of bias voltage for samples etched in CF_4 , SiF_4 , and $SiCl_4$ in a stainless-steel chamber. The interface states generated on the etched surfaces increase with the bias voltage. The surface properties of the etched Si also depend on the etching gas. Samples etched in CF_4 showed higher densities of interface states compared with those etched in SiF_4 and $SiCl_4$. The differences may result from the deposition of carbon-related polymers on the Si surfaces for samples exposed to etching gases containing carbon.

Samples etched by RIE are subjected to ion bombardment, radiation damage due to UV photons, high-energy electrons and x-rays, contamination by nonvolatile compounds (mostly heavy metals) sputtered from the chamber, and

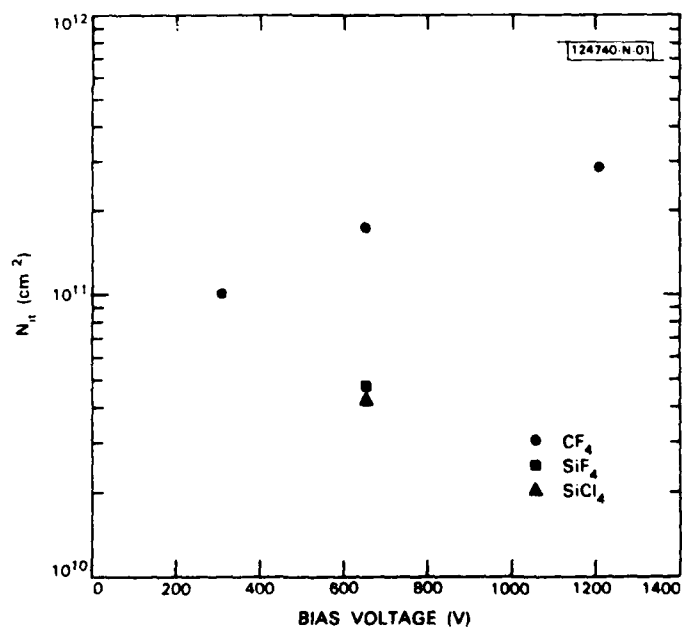


Fig. 4-7. Number of interface states induced as a function of etching voltage in CF_4 , SiF_4 , and $SiCl_4$.

polymer formation by the reactive gases. To eliminate the effect of chamber contamination, the etching chamber was coated with a 1- μm -thick layer of amorphous SiO_x by an RF discharge in $\text{SiCl}_4 + \text{O}_2 + \text{Ar}$. Figure 4-8 shows the low-frequency C-V curves for samples etched in CF_4 at 600 V in a stainless-steel chamber and in a SiO_x -coated chamber. The calculated interface-state densities for the samples etched in a coated chamber are four times less than for the samples etched in a stainless-steel chamber. This suggests that a significant amount of RIE-related damage originates from the nonvolatile compounds sputtered from the chamber.

The effect of etching-chamber contamination was investigated by varying the area ratio between the powered and the grounded electrodes. As the area of the powered electrode was reduced by one-half as shown in Fig. 4-6(b), the ion energy bombarding the chamber was also reduced.⁹ Samples etched in such a

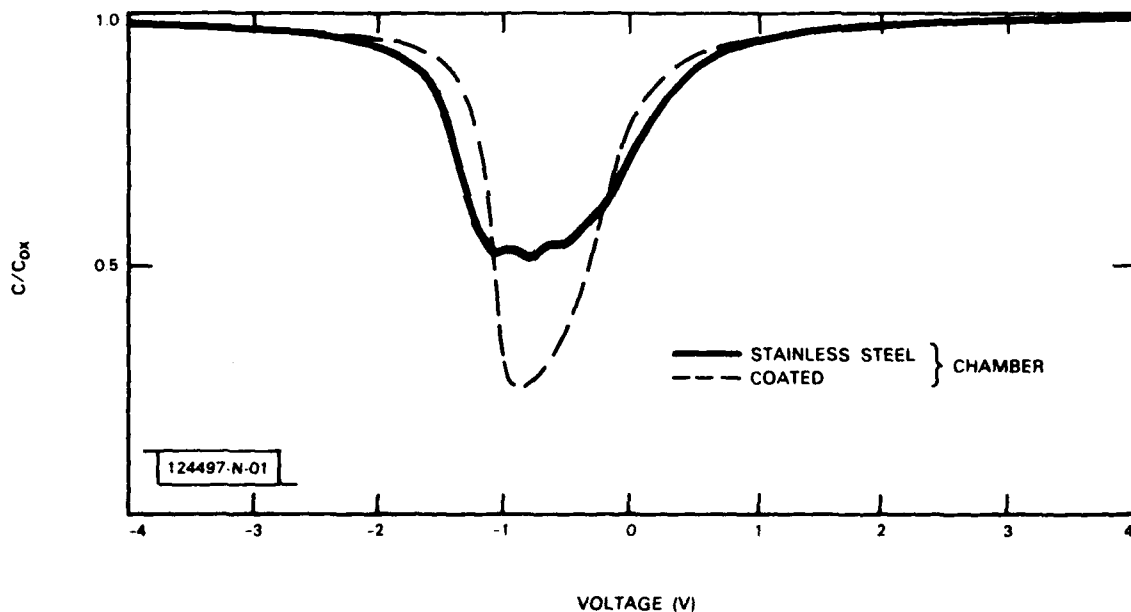


Fig. 4-8. Low-frequency C-V curves showing difference in interface-state generation for samples etched in a stainless-steel chamber and in a coated chamber. Samples were etched in CF_4 at 600 V.

confined chamber configuration showed less interface-state generation than samples etched in a chamber with a powered electrode of larger area.

S.W. Pang	D.J. Silversmith
D.D. Rathman	R.W. Mountain
S.M. Cabral	

4.3 HIGH-RESOLUTION ION-BEAM LITHOGRAPHY AT LARGE GAPS USING STENCIL MASKS

Masked ion-beam lithography (MIBL) has shown great potential as a high-resolution pattern transfer technique.¹¹⁻¹⁸ One of the principal attractions of ion lithography is the very short exposure times (<1 s) even for low-sensitivity, high-resolution resists such as polymethylmethacrylate (PMMA). The fast exposures are made possible by the availability of high-brightness ion sources and the efficiency of resist exposure by ions.¹⁹ Linewidths less than 40 nm have been demonstrated in PMMA resists with protons using masks in contact with the resist.^{15,16} Here, we describe the fabrication of two new types of membrane stencil masks and demonstrate 160-nm resolution in PMMA at 275- μ m gap between mask and substrate. The two masks are respectively composed of a single-layer, Si-rich, silicon nitride (SiN) and a Si_3N_4 - SiO_2 - Si_3N_4 (N-O-N) sandwich structure.

Figure 4-9 shows a schematic illustration of our N-O-N stencil mask. The 1- μ m thickness is sufficient to stop 100-keV protons, since the energy loss in the membrane is approximately 100 keV/ μ m (Ref. 20). The profile of the transmission holes is important since nonvertical walls will allow ions to penetrate the edges of the holes and be scattered. The pattern consists of a 320-nm-period grating with a perpendicular 12- μ m-period grating which acts as a support structure. Masks with this type of pattern were fabricated from SiN as well as N-O-N films.

In order to minimize the distortion of the mask during exposure, the membrane should have inherent tensile stress.¹² However, as the stress approaches the tensile strength of the membrane material, the mask becomes very fragile. For these reasons, we have adopted deposition procedures for

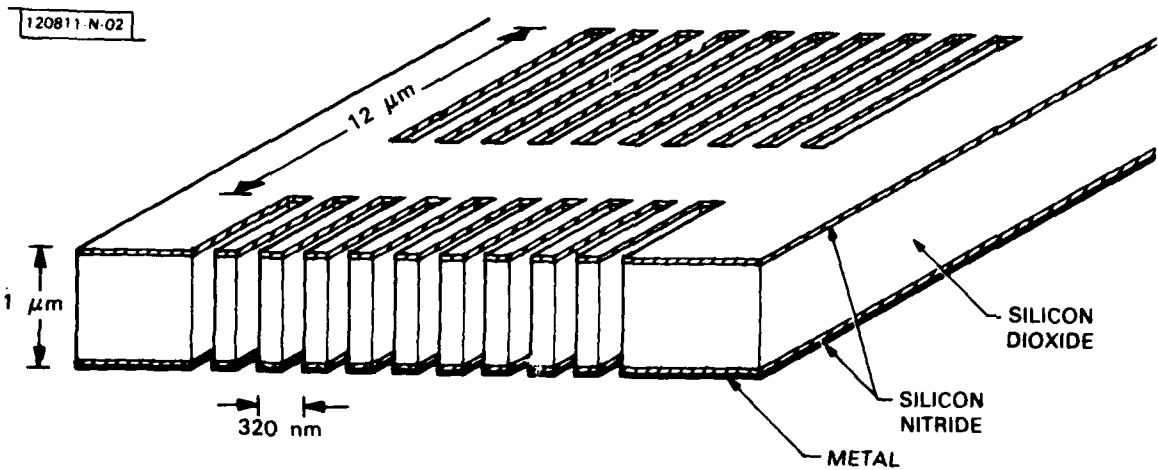


Fig. 4-9. Schematic illustration of a section of a $\text{Si}_3\text{N}_4\text{-SiO}_2\text{-Si}_3\text{N}_4$ (N-O-N) ion lithography stencil mask.

both the SiN and the N-O-N films which allow the amount of stress to be adjusted to achieve a compromise between these conflicting requirements.^{21,22} Patterns in the SiN films were etched by RIE using CF_4 gas, and the N-O-N films were etched in CHF_3 (Ref. 23). The RIE masks were fabricated by patterning PMMA using contact x-ray lithography and then lifting off an 80-nm-thick layer of evaporated Ni. Although the single-layer SiN masks are easier to fabricate and appear to be more robust than the N-O-N masks, the profile of the etched N-O-N film is superior. This can be seen clearly in Fig. 4-10(a-b) which shows SEM micrographs of both the SiN and N-O-N structures. An improved RIE process for the SiN film would eliminate this advantage of the N-O-N mask, making SiN the preferred material.

To complete the masks, 1-mm-square openings were defined in an Si_3N_4 layer on the back of the wafer. The Si in the openings was removed and 40-nm-thick Ni was evaporated at normal incidence onto the back side of the mask to render it conducting and prevent charging in the ion beam. Figure 4-11 shows an SEM micrograph of a cleaved section of a completed SiN mask.



(a) (b)

Fig. 4-10. SEM micrographs of 320-nm-period grating etched by RIE into ion lithography stencil mask materials: (a) a SIN structure produced by CF_4 RIE, (b) an N-O-N structure produced by CHF_3 RIE.

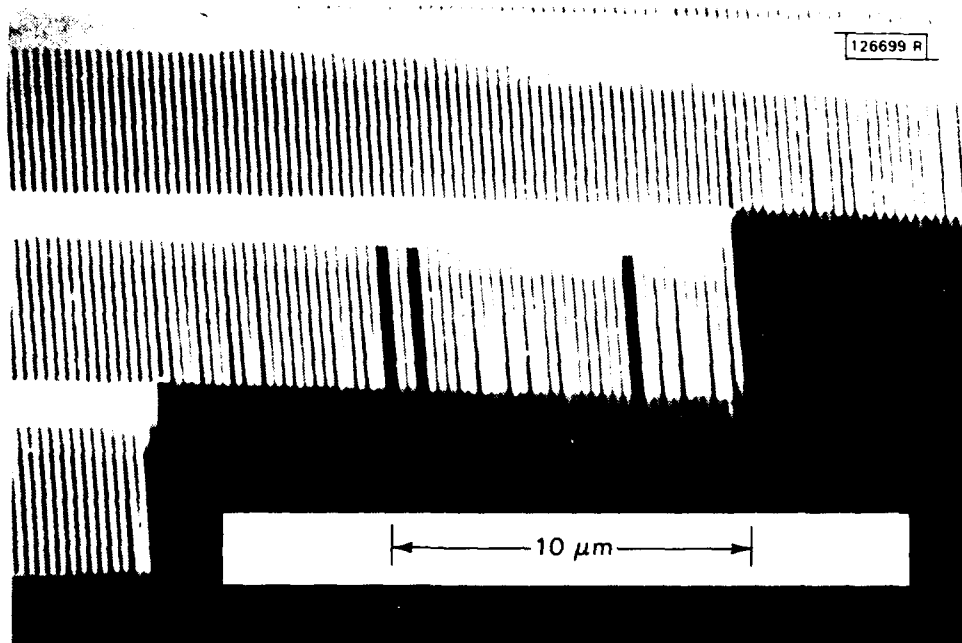


Fig. 4-11. SEM micrograph of a cleaved section of a completed N-O-N stencil mask. Mask is 1 μm thick, period of grating is 320 nm, and period of support structure is 12 μm .

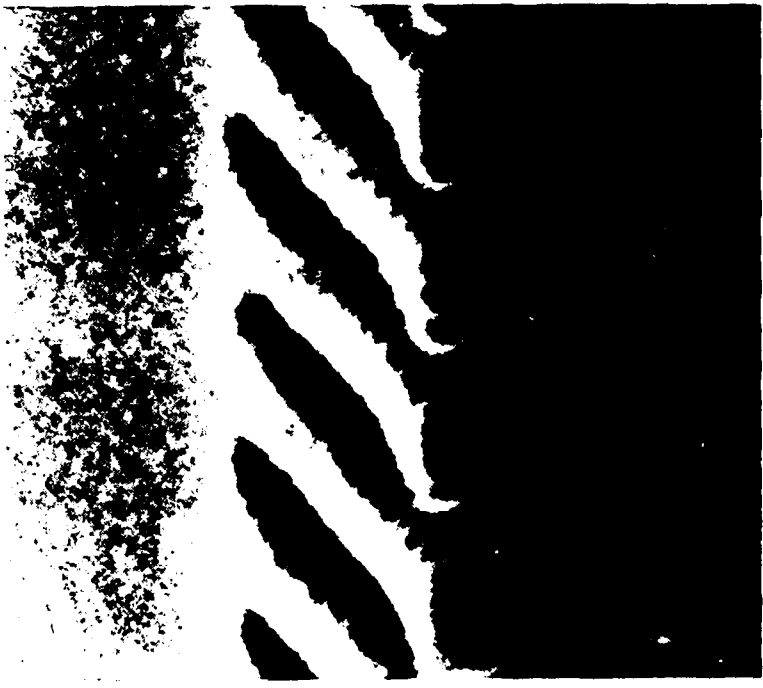
The ion-beam system used for resist exposure experiments was an in-house-built system based on a modified 400-kV Van de Graaff generator. All the exposures reported here were made with 100-keV protons and a total beam current of 1 to 4 μA . The resist in each case was 0.5- μm -thick, 950,000 molecular weight PMMA developed in a mixture of 40% methyl isobutyl ketone and 60% isopropyl alcohol. During exposures, the mask and sample were held at a fixed gap by stacking a silicon wafer coated with PMMA, an annular spacer, and the mask and clamping them to the sample holder with spring clips. Figure 4-12 shows SEM micrographs of the PMMA structure resulting from a $3 \times 10^{13} \text{ H}^+/\text{cm}^2$ exposure made with a SiN mask at (a) 25- μm and (b) 275- μm mask-to-sample gaps. From these micrographs, the divergence of

126700 R



320 nm

(b)



320 nm

(a)

Fig. 4-12. SEM micrographs of PMMA structures resulting from 100-key proton exposures through a SiN stencil mask at a dose of $3 \times 10^{13} \text{ H}^+/\text{cm}^2$: (a) at a 25- μm and (b) at a 275- μm mask-to-sample gap.

the beam can be conservatively estimated to be less than 0.6 mrad. Figure 4-13 shows an exposure at $5 \times 10^{14} \text{ H}^+/\text{cm}^2$ through a SiN mask at a 25- μm gap. The PMMA has acted as a negative resist at this dose.

There are a number of problems inherent in the use of stencil masks. The most obvious is the inability to reproduce arbitrary patterns since geometries which close on themselves are not permitted. Furthermore, patterns with large openings or long spans of very fine lines are permitted, but are often impractical because of instability of the structure. For simple patterns of these types, multiple exposures with a mask containing support structures can circumvent these problems. An example is shown in Fig. 4-14 which is an SEM micrograph of the result of two exposures made through an N-O-N mask. The exposures were done as previously described with an $\sim 60\text{-}\mu\text{m}$ -thick spacer. Between exposures, the mask remained clamped to the substrate and the sample holder was tilted $\sim 6^\circ$ with respect to the beam in a direction parallel to the 320-nm-period grating lines. Because of the gap, there was a 6- μm shift in the image such that the second exposure filled the

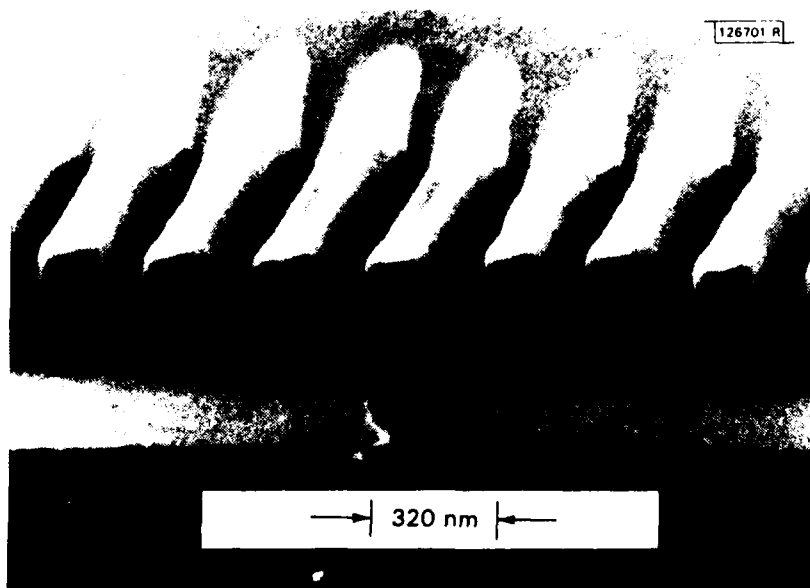


Fig. 4-13. SEM micrograph of a PMMA structure where PMMA has acted as a negative resist. Exposure was done with 100-keV protons through a SiN stencil mask at a dose of $5 \times 10^{14} \text{ H}^+/\text{cm}^2$.

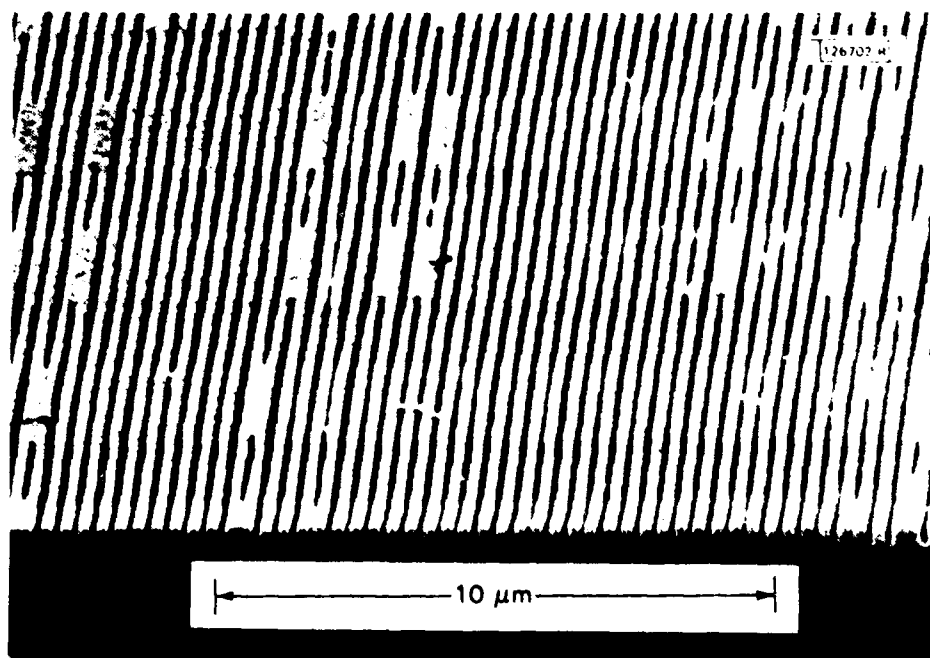


Fig. 4-14. SEM micrograph of a double exposure through type of mask depicted in Fig. 4-9. Exposures were done at 100 keV at a dose of $3 \times 10^{13} \text{ H}^+/\text{cm}^2$ with an $\approx 60\text{-}\mu\text{m}$ gap between mask and substrate. Between exposures, mask and sample remained clamped while they were tilted 6° with respect to ion beam in a direction parallel to 320-nm-period grating.

area previously masked by the support structure, resulting in a large-area grating composite exposure. The variation in linewidth is due in part to a slight angular difference between the direction of the grating lines and the image shift. The unconnected lines are due to opaque mask defects. Another possible method of overcoming the stencil mask problem is by using multiple aligned exposures with complementary masks.²⁴

J.N. Randall
D.C. Flanders
N.P. Economou

J.P. Donnelly
E.I. Bromley

126703 S

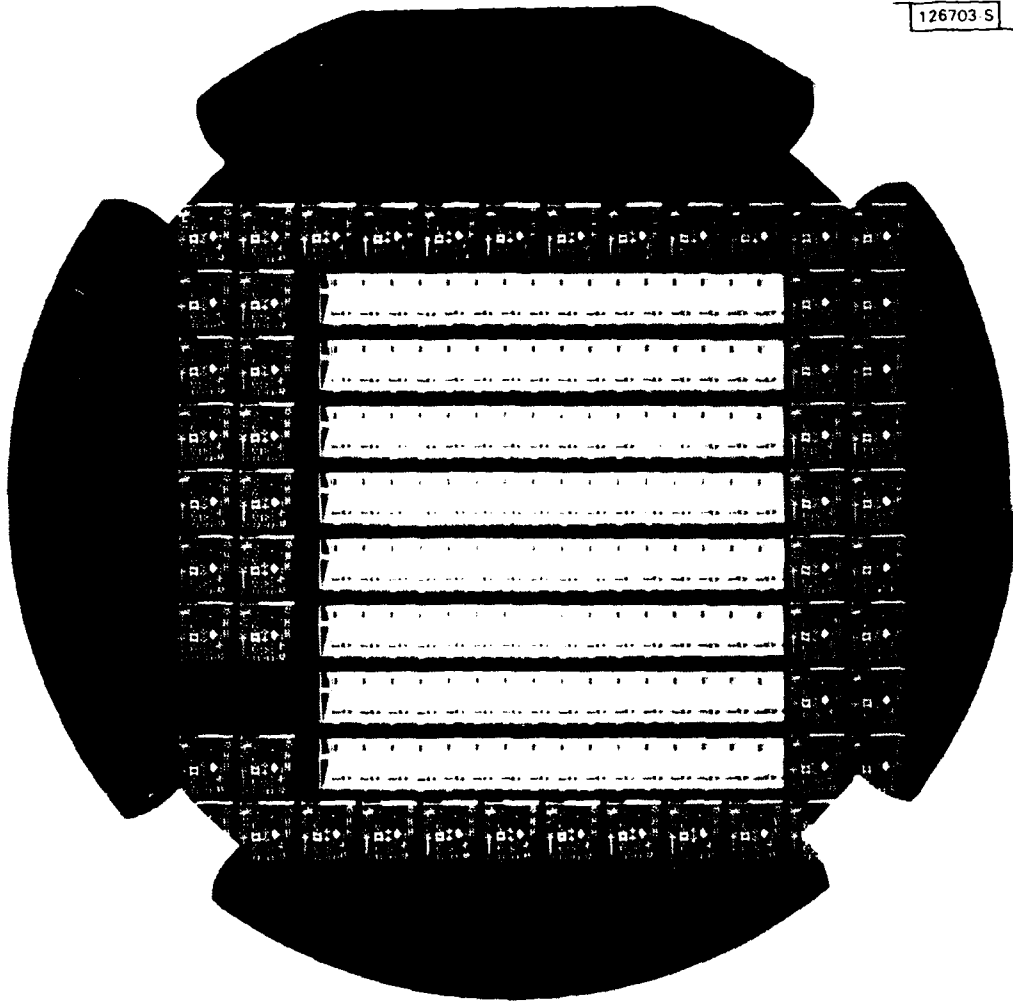


Fig. 4-15. A 128-kbit EBROM. Eight rows in center of wafer are 16K modules. Each 16K module consists of sixteen 1K subsystems which are interconnected by metal lines running across wafer. Bonding pads are located on left edge of memory array. Test chips surround memory system.

4.4 ELECTRON-BEAM PROGRAMMABLE 128-KBIT WAFER-SCALE EPROM

MOS transistors with floating, oxide-encapsulated, polysilicon gates can act as electron-beam-controlled nonvolatile switches.²⁵ Floating-gate transistors are commonly used in UV-erasable, electrically programmable read-only memories (EPROMs),²⁶ but in these devices a transistor is programmed by forcing charge onto the floating gate using hot-electron injection from a junction in breakdown or by applying high fields across an oxide layer. Thus, conventional EPROMs require electrical access circuitry to select a specific FET for programming. The electron-beam technique eliminates the requirement for access circuitry since the submicrometer-size beam is merely deflected over the transistor to be programmed and unblanked, directly charging the gate. Electron-beam programming is attractive for customizing circuits which do not have the simple, regular access paths found in ROMs, and is also appropriate for making fault-avoiding interconnections on wafer-scale circuits where it is difficult to provide low-overhead, defect-free access circuits.

A wafer-scale, 128-kbit, electron-beam-programmable ROM (EBPROM) has been fabricated as a test vehicle to demonstrate the feasibility of programming large numbers of nonvolatile switches using an electron beam. Figure 4-15 is a photograph of a completed ROM, which consists of eight 16K x 1-bit modules covering a 23 x 26-mm area in the center of a 50-mm-diam Si wafer. Test chips surround the memory. The wafer requires only +5 V, and operation is fully static. A simple 5-mask nMOS process (single-level metal and polysilicon) with 6- μ m design rules was used.

Figure 4-16 is a block diagram of a 1K subsystem, which contains 34 row selectors, 34 column selectors, a 34 x 34 memory plane, and a "chip-select" circuit. Each row and column selector contains 10 electron-beam programmable links, the memory plane contains 1156 links, and the chip select has 8 links. A 1K subsystem cannot respond on the output bus until 4 of the 8 links in the chip-select have been programmed to give the subsystem a 4-bit select code. Similarly, 5 links must be programmed in each row and column selector to

AD-A128 894

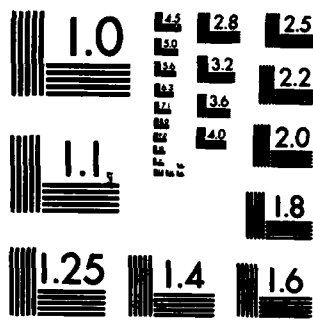
SOLID STATE RESEARCH(U) MASSACHUSETTS INST OF TECH
LEXINGTON LINCOLN LAB A L MCWHORTER 15 FEB 83 1983:1
ESD-TR-83-001 F19628-80-C-0002

2/2

UNCLASSIFIED

F/G 5/1 • NL





MICROCOPY RESOLUTION TEST CHART
NATIONAL BUREAU OF STANDARDS-1963-A

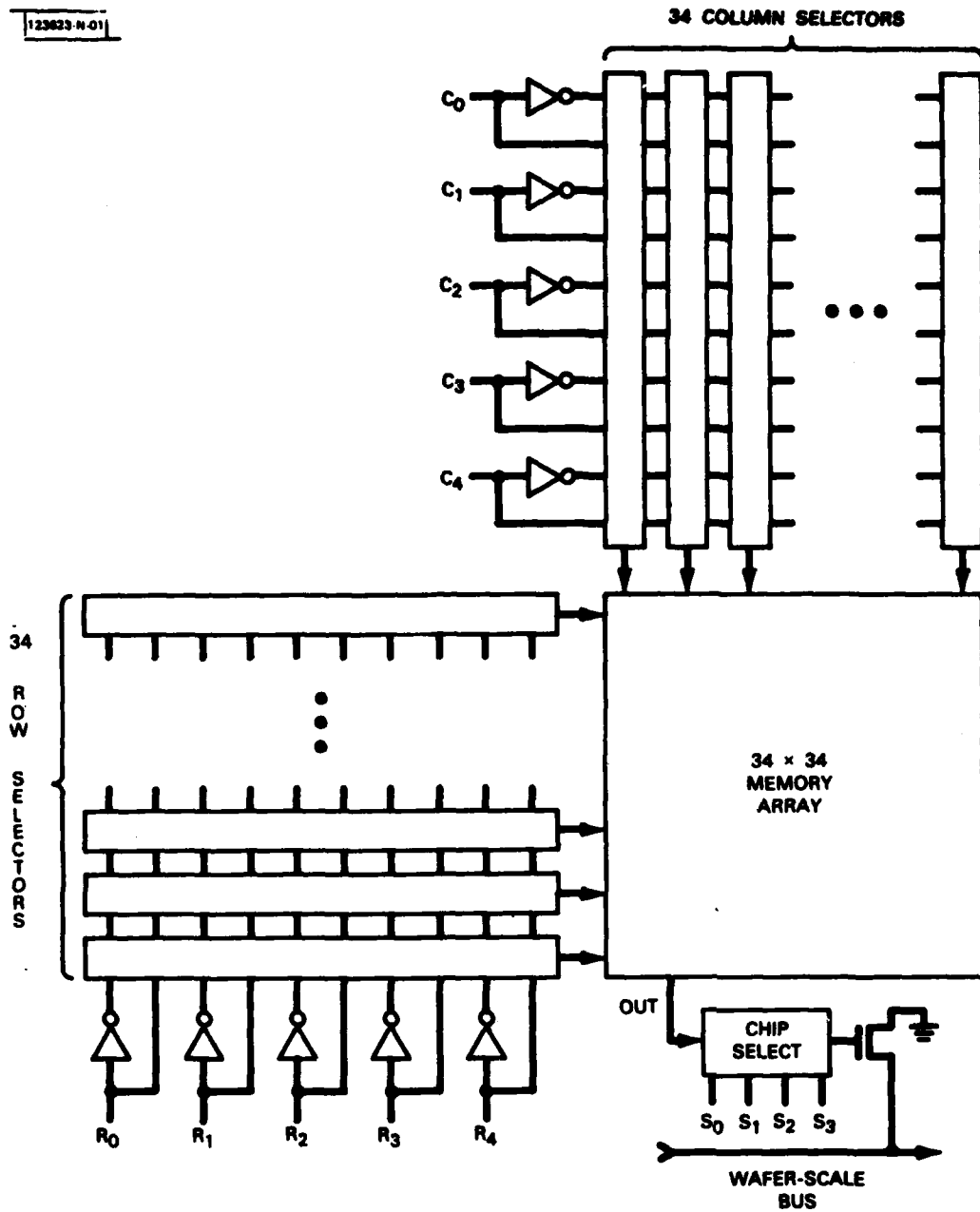


Fig. 4-16. Block diagram of 1-kbit subsystem. A 10-bit address provides row (R_0 to R_4) and column (C_0 to C_4) selection. Each row or column selector, shown as a rectangular box, contains 5 programmable links. Output of memory, if enabled by chip select, can pull a wafer-scale output bus to ground.

allow that row or column to respond to a given 5-bit address. A 5-bit address is used to select one of 32 rows (or columns), but 34 rows (or columns) are provided so that spares are available for substitution. It is worth noting that no difference exists between "spare" and "original" rows since all rows are initially deselected and must be electron-beam programmed; for this reason, the EBPROM is equivalent to an e-beam programmed PLA. Because of this flexibility in assigning rows and columns, the spatial mapping of the data pattern can even be made to conform to the wafer's defect pattern.

The floating-gate links used were depletion-mode nMOS FETs with nominal channel areas of $6 \times 6 \mu\text{m}$. Each memory bit has an area of $27 \times 33 \mu\text{m}$, and includes a floating-gate link and an enhancement-mode select transistor. In the initial "erased" state, the FETs are "ON" with a drain-source sheet resistance (at low V_{ds}) of $\sim 30 \text{ k}\Omega/\square$. An FET is turned "OFF" ($I_{ds} < 10 \text{ nA}$ at $V_{ds} = +5 \text{ V}$) by injecting $\sim 2 \times 10^{-13} \text{ C}$ of charge from the incident 5-kV electron beam. Presently, a 0.5-nA beam with a spot diameter of $\sim 0.5 \mu\text{m}$ is used, so the link programming time is 0.4 ms. Only a few minutes are required to program the ROM ($>10^5$ links). Even faster programming is possible by increasing the beam current, and a 5-nA beam is readily obtained in the ETEC LEBES electron-beam-lithography system used for these experiments.

Though larger deflection fields are possible, we deflect the beam over only a $2 \times 2\text{-mm}$ area. This puts about 2000 links within the deflection field. The wafer can also be moved beneath the electron beam, allowing any point on the wafer to be accessed by a combination of beam deflection and X-Y table motion. After registration to the wafer, any coordinate on the wafer can be located with $\pm 0.5\text{-}\mu\text{m}$ accuracy.

Preliminary data indicate that the nonvolatility of the electron-beam programmed floating gates can be excellent, and will probably be comparable with that for conventional FAMOS devices. Data on one wafer ($>200,000$ floating gates) reveal no data loss after accelerated life testing at 190°C for 10 h. Erasure of the links is possible using UV flood exposure to erase

the entire wafer, or a 20-kV electron beam to remove the charge stored on individual floating-gate FETs.

D.C. Shaver
R.W. Mountain
D.J. Silversmith

4.5 TUNNELING IN QUANTUM-WELL STRUCTURES

Tunneling is an exceedingly fast process. Since energy is not conserved while the particle is traversing the energy barrier, the tunneling time is given by the energy-time uncertainty relation $t < h/E$, where E is the barrier height. For barrier heights usually encountered in semiconductors, devices based on tunneling should respond to frequencies well into the far-infrared. That is, devices with nonlinear DC current-voltage relations in which the charge transport mechanism is tunneling can be expected to have the same nonlinear behavior at very high frequencies.

We have been exploring the possibility that tunneling between quantum wells may produce nonlinear I-V curves similar to those produced by superconducting tunnel junctions; the latter have been demonstrated to have very low noise and conversion loss, and even conversion gain.²⁷ We have taken theoretical I-V curves from the literature²⁸ for a GaAs quantum well 50 Å wide enclosed by barriers of GaAlAs 20 Å wide, and to these we have applied the quantum theory of mixing²⁹ to calculate the effects of submillimeter radiation. This quantum mixing theory is required when the slope of the I-V curve changes significantly in a voltage interval $h\nu/e$. Regular features induced on the I-V curve by incident radiation within this voltage interval are called photon steps. The results of these calculations show photon steps in the I-V curves with incident radiation at microwatt power levels, and downconversion gain under appropriate impedance matching conditions of the embedding network. Figure 4-17 shows the conversion efficiency as a function of DC bias voltage. (There is an uncertainty in the calculated values of approximately 3 dB at the higher voltages.)

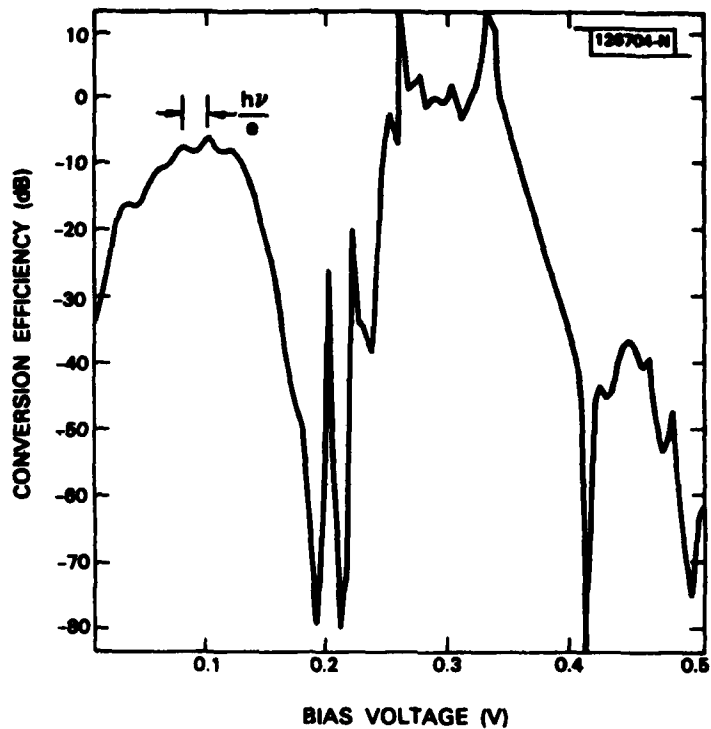


Fig. 4-17. Computed conversion efficiency of a quantum-well structure as a function of bias voltage. Local oscillator frequency is 5 THz at a power of 10 μ W. Note spikes which are separated in voltage corresponding to photon steps $h\nu/e$.

Fabrication and evaluation of quantum-well structures similar to those used as the basis for these calculations is currently under way to provide experimental tests for these promising theoretical results.

T.C.L.G. Sollner

REFERENCES

1. C.M. Horwitz, IEEE Trans. Electron Devices ED-28, 1320 (1981).
2. S. Pang, D.D. Rathman, D.J. Silversmith, R.W. Mountain, and P.D. DeGraff, Electrochemical Society Extended Abstracts, Detroit, Michigan, 17-22 October 1982, p. 289.
3. D.D. Rathman, N.P. Economou, D.J. Silversmith, R.W. Mountain, and S.M. Cabral, Proc. Intl. Electron Devices Mtg., San Francisco, 13-15 December 1982, pp. 650-653.
4. M. Sato and H. Nakamura, J. Vac. Sci. Technol. 20, 186 (1982).
5. G. Herb, R. Porter, P. Curzon, J. Agraz-Guetena, and B. Soller, Electrochemical Society Extended Abstracts, Denver, 11-16 October 1981, p. 710.
6. J.W. Coburn, "Semiconductor Technology," in Electrochem. Soc. Proc. 82-5, 177 (1982).
7. D.L. Flamm and V.M. Donnelly, Plasma Chemistry and Plasma Processing 1, 315 (1981).
8. C.M. Horwitz and J. Melngailis, J. Vac. Sci. Technol. 19, 1408 (1981).
9. H.R. Koenig and L.J. Maissel, IBM J. Res. Dev. 14, 168 (1970).
10. M. Kuhn, Solid-State Electron. 13, 873 (1970).
11. D.B. Rensch, R.L. Seliger, G. Csanky, R.D. Olney, and H.L. Stover, J. Vac. Sci. Technol. 16, 1897 (1979).
12. J.L. Bartelt, C.W. Slayman, J.E. Wood, J.Y. Chen, C.M. McKenna, C.P. Minning, J.F. Coakley, R.E. Holman, and C.M. Perrygo, J. Vac. Sci. Technol. 19, 1166 (1981).
13. G. Stengl, R. Kaitna, H. Loschner, P. Wolf, and R. Sacher, J. Vac. Sci. Technol. 16, 1883 (1979).
14. R. Speidel and U. Behringer, Optik 54, 439 (1980).
15. L. Karapiperis and C.A. Lee, Appl. Phys. Lett. 35, 395 (1979).
16. N.P. Economou, D.C. Flanders, and J.P. Donnelly, J. Vac. Sci. Technol. 19, 1172 (1981), DTIC AD-A117801/1.

17. H. Ryssel, K. Habberger, and H. Kranz, *J. Vac. Sci. Technol.* 19, 1358 (1981).
18. I. Adesida, J.D. Chinn, L. Rathbun, and E.D. Wold, *J. Vac. Sci. Technol.* 21, 666 (1982).
19. M. Komuro, N. Atoda, and H. Kawakatsu, *J. Electrochem. Soc.: Solid-State Sci. & Technol.* 129, 483 (1979).
20. B. Smith, *Ion Implantation Range Data for Silicon and Germanium Device Technologies* (Research Studies Press, Forrest Grove, Oregon, 1977).
21. M. Sekimoto, H. Yoshihara, T. Ohkubo, and Y. Saioh, *Jpn. J. Appl. Phys.* 20, 669 (1981).
22. K. Suzuki, J. Matsui, T. Kadota, and T. Ono, *Jpn. J. Appl. Phys.* 17, 1447 (1978).
23. H.W. Lehman and R. Widmer, *J. Vac. Sci. Technol.* 15, 319 (1978).
24. H. Bohlen, J. Greschner, W. Kulcke, and P. Nehmiz, *Proceedings of the Symposium on Electron and Ion Beam Science and Technology Eighth International Conference* (Electrochemical Society, Inc., Princeton, New Jersey, 1978), p. 406.
25. D.C. Shaver, *J. Vac. Sci. Technol.* 19, 1010 (1981), DTIC AD-A117826/8.
26. D. Frohman-Bentchkowsky, *Solid-State Electron.* 17, 517 (1974).
27. See, for example. G.J. Dolan, R.A. Link, D.P. Woody, T.C.L.G. Sollner, and T.G. Phillips, *IEEE Trans. Microwave Theory Tech.* MTT-29, 87 (1981); T.G. Phillips, D.P. Woody, G.J. Dolan, R.E. Miller, and R.A. Linke, *IEEE Trans. Magn.* MAG-17, 684 (1981); L. Olsson, S. Rudner, E. Kollberg, and C.O. Lindstrom, *Proc. 12th European Microwave Conf.*, Helsinki, September 1982.
28. R. Tsu and L. Esaki, *Appl. Phys. Lett.* 22, 562 (1973).
29. J.R. Tucker and M.F. Millea, *Appl. Phys. Lett.* 33, 611 (1978).

5. ANALOG DEVICE TECHNOLOGY

5.1 SUPERCONDUCTIVE PULSE COMPRESSOR

The realization of multigigahertz-bandwidth analog-signal-processing devices as superconductive tapped electromagnetic delay lines has been discussed,¹ pulse compression over a limited (800-MHz) bandwidth has been demonstrated,² and trade-offs in the choice of dielectric substrates have been presented.³ We describe here the performance of a device with a 2.6-GHz bandwidth and 35-ns dispersion, and compare it with the prediction from a theoretical model.

The tapped-delay-line structure is a cascade of backward-wave couplers of variable coupling strength and length, as shown schematically in Fig. 5-1. The weights and lengths are specified by using a design procedure which synthesizes the desired linear-group-delay characteristics and amplitude-weighting function.

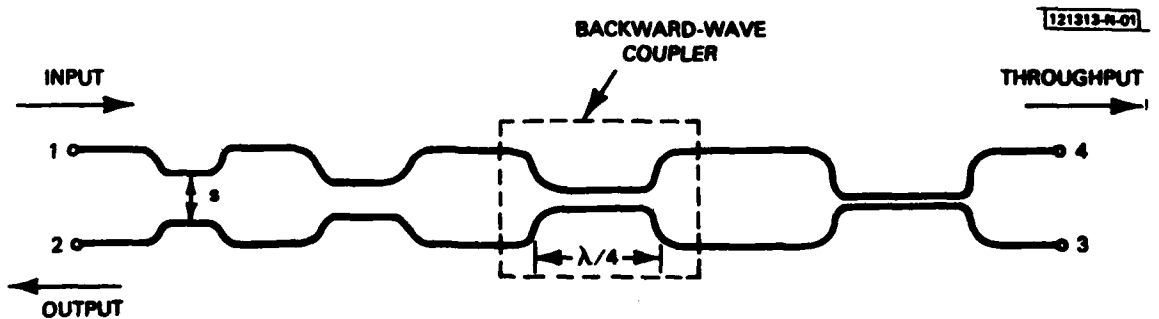


Fig. 5-1. Chrip filter formed by cascading backward-wave couplers.

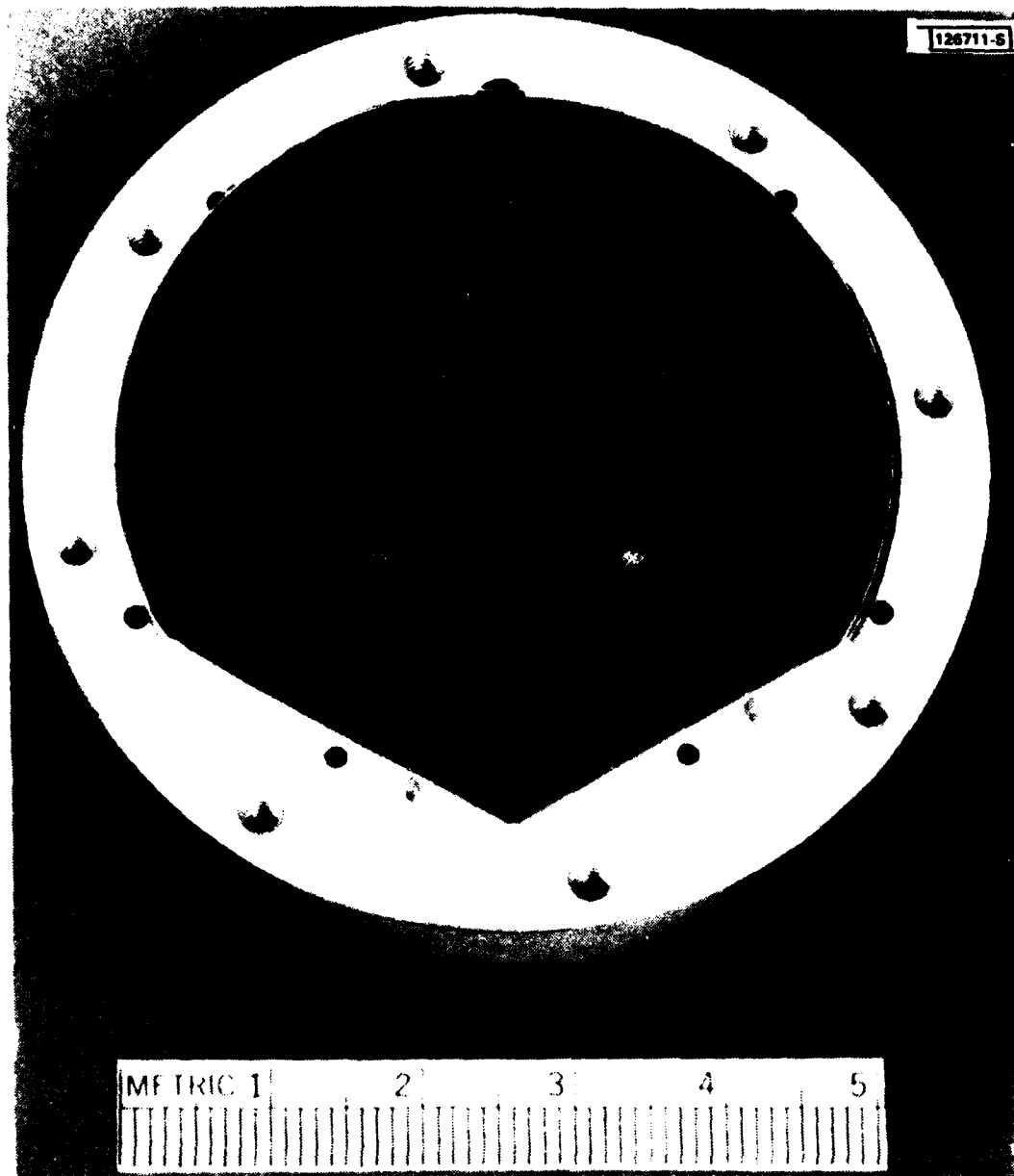


Fig. 5-2. Photograph of a superconductive tapped delay line just prior to final assembly.

The structure is wound into a quadruple-spiral pattern so that it fits on a 5-cm-diam substrate (Fig. 5-2). Note that all four RF ports are brought to the edge of the wafer for the attachment of leads. The device is fabricated by the reactive-ion etching of RF-sputtered niobium on a sapphire substrate. The stripline structure is completed by placing a second sapphire wafer, with a superconducting ground plane, atop the patterned wafer shown in Fig. 5-2.

The chirp filter of Fig. 5-2 is a coupled pair of striplines, each 1.59-m long to give a total dispersion of 35 ns. The linewidth is a constant 42 μm , designed for 50- Ω impedance on the 125- μm -thick sapphire. The separation between lines (s in Fig. 5-1) is 279 μm in the couplers and 406 μm outside the couplers and between adjacent spiral turns of the coupled pair. These dimensions give a predicted coupling coefficient 2Γ of 10^{-2} , i.e., all couplers are 40 dB in strength. (Such a device with all taps of the same strength is called "linear-weighted." The increasing number of taps per unit length as the high-frequency end of the device is approached results in an insertion loss which decreases linearly with frequency.)

The designed chirp response begins at 2.7 GHz and ends at 5.3 GHz, for a time-bandwidth (TB) product of 91 and chirp slope of 74.2 MHz/ns.

Using a 10-VDC impulse of 135-ps width as input, the down-chirp response in the upper trace of Fig. 5-3(a) was obtained. This expanded pulse was amplified and applied to the up-chirp end of the same device. The matched-filter response is presented in the lower trace of Fig. 5-3(a).

This compressed pulse is shown on an enlarged time scale in Fig. 5-3(b). The theoretically predicted response has a nearly $\sin x/x$ envelope. The envelope of the actual response is difficult to discern, because the nearly octave bandwidth of the device results in only a few half-cycles of carrier within each lobe. Nevertheless, the main lobe clearly has a null-to-null width of slightly less than 800 ps, consistent with the designed 2.6-GHz bandwidth.

With the use of an automatic network analyzer, the CW phase and amplitude responses of both the up- and down-chirp ends of the device were

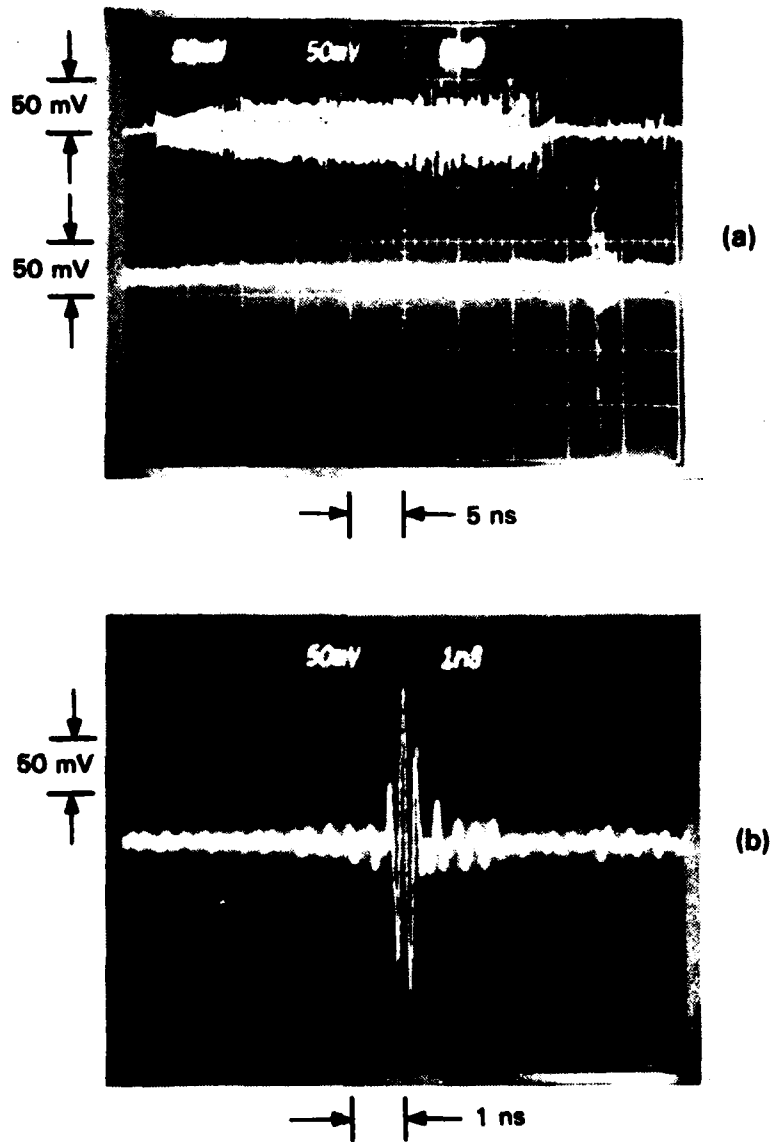


Fig. 5-3. Pulse expansion and compression with superconductive tapped delay line of Fig. 5-2. (a) Upper trace: expanded down-chirp pulse; lower trace: compressed pulse output of up-chirp end of device after application of expanded pulse. (b) Enlarged view of compressed pulse output, clearly demonstrating 2.6-GHz bandwidth.

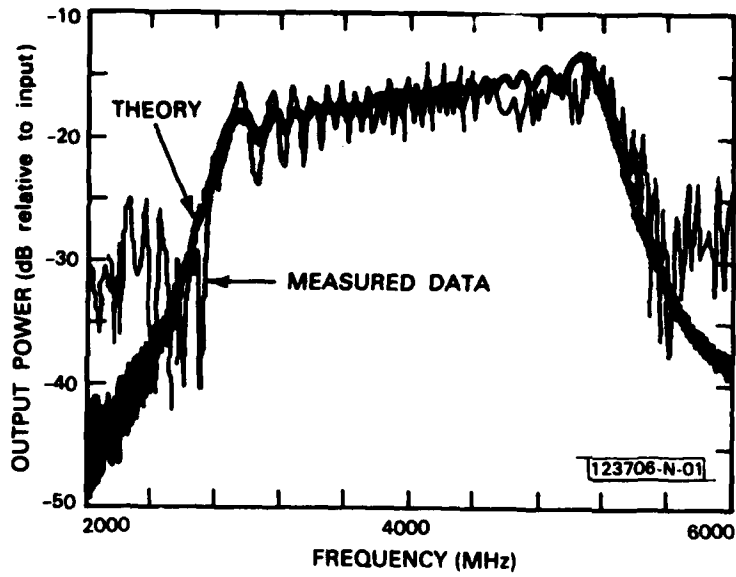
obtained from 2 to 6 GHz. Figure 5-4(a) shows the measured and predicted amplitudes of the down-chirp pair. The predictions were made with the first-principles theory used to design the device and are based on the physical design parameters of the device. Except for the fine-scale deviations (attributed to spurious reflections), the agreement across the passband (2.7 to 5.3 GHz) is very good, theory and experiment being in agreement within about 2 dB.

The measured phase spans a range of more than $25,000^\circ$ across the passband and is essentially a quadratic function, as expected. The measured and theoretical deviations from a best-fit quadratic are plotted in Fig. 5-4(b). The difference between measured and predicted response is dominated by distortions which probably result from spurious reflections. The rms value of the deviation of the measured response from quadratic phase is 12.0° . The theoretical deviation from quadratic phase is dominated by the Fresnel ripple resulting from the asymmetry of the integral near the band edges.

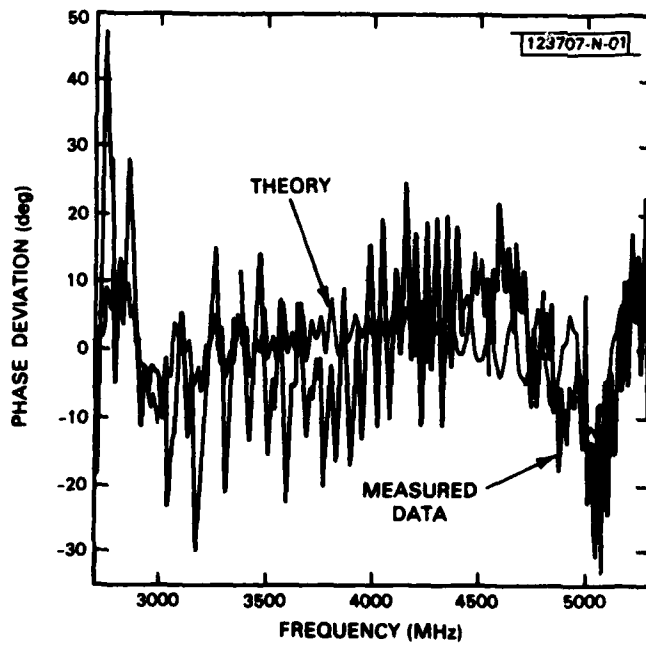
The least-squares-fit quadratic coefficient of phase for the measured data is $2.361 \times 10^{-3} \text{ deg/MHz}^2$, which implies a chirp slope of 76.24 MHz/ns. The up-chirp phase was also measured and gave a least-squares value implying a chirp slope of 76.40 MHz/ns, which is in excellent agreement and indicates well-matched filters. The design value is 74.2 MHz/ns for both up- and down-chirp. This error of less than 3 percent could be caused by a comparable overestimation of the effective dielectric constant of the substrate.

The measured phase and amplitude responses of the up- and down-chirp ends of the device were multiplied and Fourier transformed to give the compressed pulse response envelope shown in Fig. 5-5. The response predicted by the theory is plotted alongside the measured data. Except for the 2-dB shift, the agreement is excellent, especially the side-lobe levels and positions. This augurs well for the amplitude-weighted devices now being fabricated.

R.S. Withers A.C. Anderson
P.V. Wright S.A. Reible



(a)



(b)

Fig. 5-4. (a) Predicted and measured amplitude response of tapped delay line of Fig. 5-2. (b) Predicted and measured deviations from quadratic phase for this device.

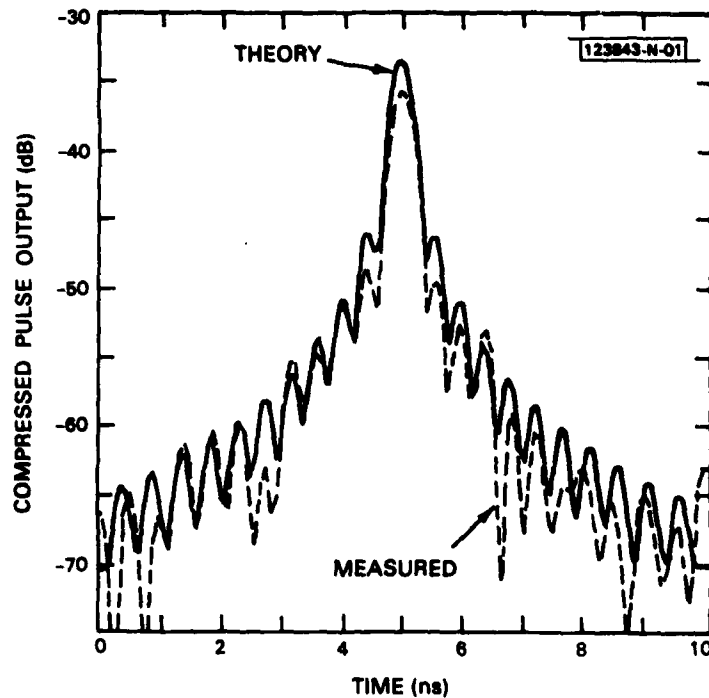


Fig. 5-5. Measured and predicted compressed-pulse response envelopes, obtained by multiplying up- and down-chirp frequency responses and Fourier transforming.

5.2 SUPERCONDUCTIVE CONVOLVER

The response of the first superconductive convolver⁴ to gated-CW input tones is described and compared with design expectations. A schematic diagram of the superconductive convolver is shown in Fig. 5-6. The device employs a niobium delay line for the relative shifting and temporary storage of signal and reference waveforms, taps for local sampling, superconductive-insulator-superconductive (SIS) junctions for the local multiplication of the sampled waveforms, and a short output transmission line for the coherent summation of the local products. Results on the responses of the separate delay line, tap, and mixer components of this device have been discussed in a previous report.⁵

In the device demonstration, signal and reference input waveforms (consisting of 14-ns duration, gated-CW tones within the 2- to 4-GHz band)

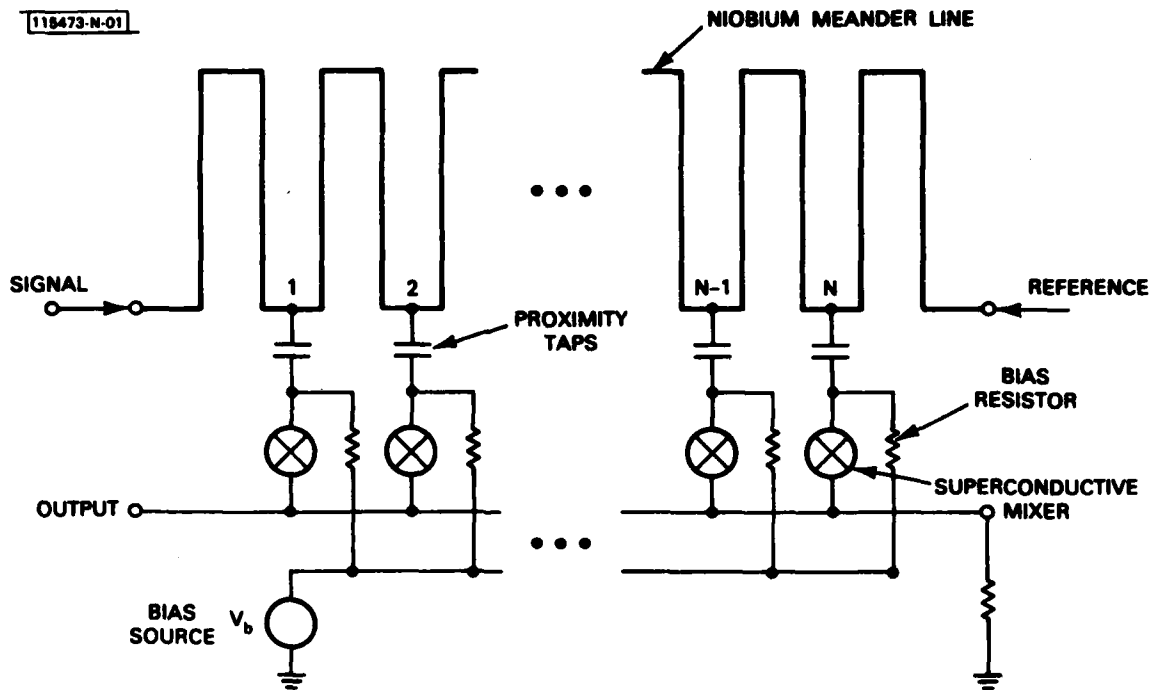


Fig. 5-6. Schematic of a superconductive convolver.

were entered into opposite ends of the 50- Ω meander delay line. The envelopes of the two input tones are shown in the upper traces of Fig. 5-7(a). The counterpropagating signal and reference waveforms were periodically sampled at 0.67-ns intervals by proximity taps having an electrical length of 40° at the 3-GHz center frequency. Each of the 19 taps, integrated with 4- μm -diam SIS junctions, formed the product of local signal and reference waveforms. Bias currents to optimize the mixing interaction were distributed through an array of normal-metal resistors. The output products from the individual mixers were collected on a low-impedance (12- Ω) output line.

The real-time output of the convolver with the gated-CW input tones is shown in the bottom trace of Fig. 5-7(a). The output waveform was amplified and band-limited to 4 to 8 GHz by a room-temperature amplifier chain which also set the thermal-noise floor. Because of the low dynamic range in the measurement, repetitive output waveforms were coherently detected and averaged. The result is shown in Fig. 5-7(b); the envelope of the convolver

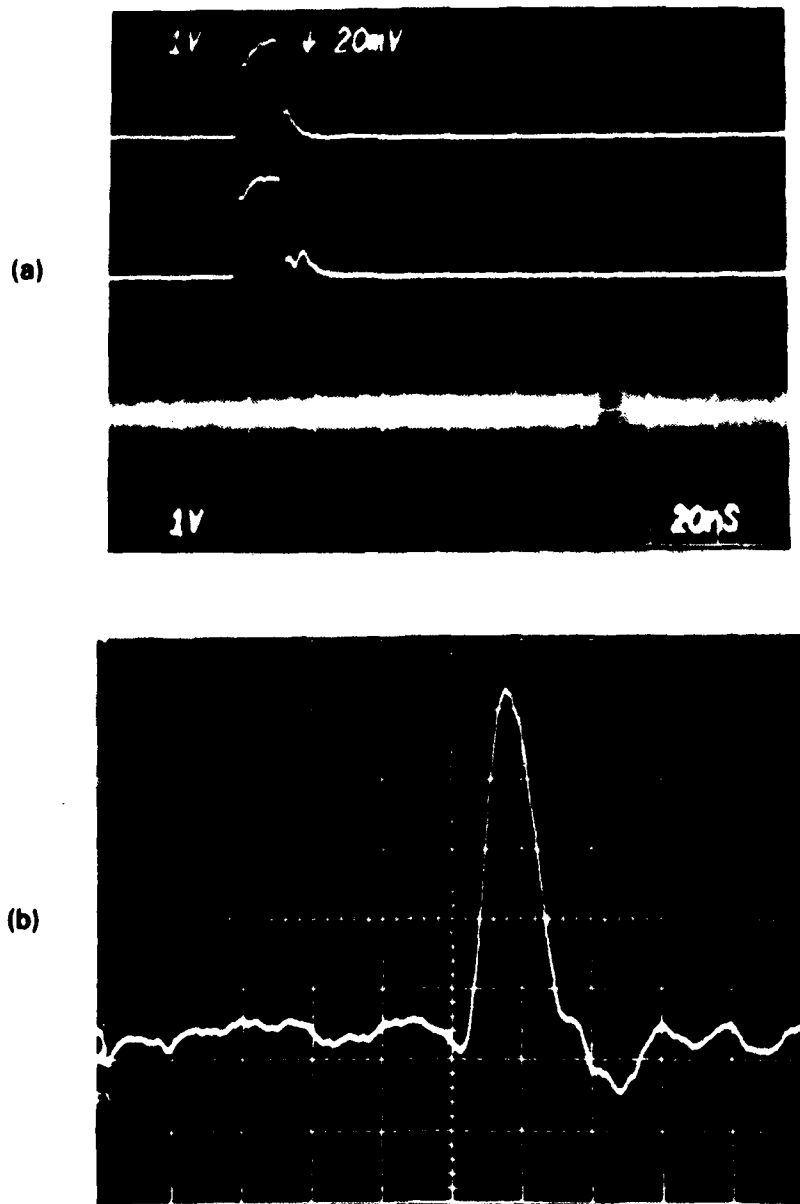


Fig. 5-7. Output of superconductive convolver. (a) Upper traces: envelopes of gated-CW input pulses; lowest trace: real-time output, horizontal scale 20 ns/div. (b) Output envelope after signal averaging, horizontal scale 10 ns/div.

output approximates the triangular shape expected for the convolution of the two nearly rectangular (~ 1 -ns risetime) input envelopes.

In order to achieve the desired coherent combining of the local products, the linear-phase distortion caused by the spacing of the collection nodes on the output line was compensated by offsetting the center frequency of the reference (ω_r) relative to the center frequency of the signal (ω_s) according to the relationship,⁶

$$\omega_r = \omega_s \frac{\tau_i + \tau_o}{\tau_i - \tau_o}$$

where τ_i and τ_o are the delay spacings on the input and output transmission lines, respectively. Half the output power propagates to each of the ports at opposite ends of the output line; since the output phase distortion can only be compensated for one direction of propagation, one port is selected as the output and the second port is terminated.

A plot of the output power from the 19-tap convolver as a function of input signal level is shown in Fig. 5-8. The data shown in this figure include an estimated 5 dB of loss in the output coaxial cable of the cryogenic probe. The device is linear, to within measurement accuracy, from input-power levels of -22 to at least -43 dBm. Output-power measurements could not be made at output levels below -100 dBm. Saturation of the superconductive nonlinearity occurs at input-power levels above -22 dBm. In order to realize a higher dynamic range, it is necessary to address the issues of efficiency and saturation.

The efficiency factor for convolvers is commonly defined by

$$F = \frac{P_c}{P_s P_r}$$

where P_s and P_r are the signal and reference input powers, and P_c is the output power of the desired product. The F factor of the superconductive convolver can be expressed as

$$F = 10 \log (A_i) (C_i^2) (M^2) (T_o^2) (R_L)$$

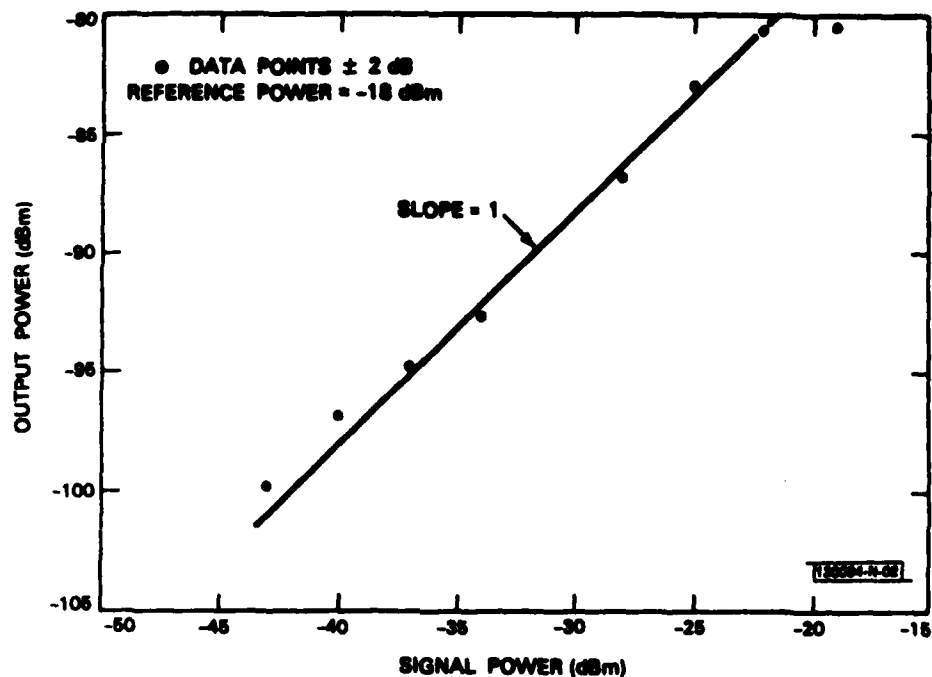


Fig. 5-8. Output power of convolver as a function of signal level.

where A_i is the attenuation and signal depletion on the input delay line, C_i is the weight of an individual proximity coupler, M is the mixer efficiency, T_o is the output current transfer function for the combined mixers, and R_L is the load impedance. Transmission-line and circuit models have been developed to predict these parameters. Predicted and measured values for the preliminary convolver design are listed in Table 5-1. The uncertainties in the measured values for A_i and C_i are because of frequency ripple in the measurement of the proximity coupler response and the cumulative effects of reflections within the meander line and the test set. It is noted that agreement between the model and the device is reasonable.

For the convolver to be a practical signal-processing device, its linear dynamic range must exceed its signal-processing gain. The dynamic range of a convolver is defined by the ratio of the output-power level at which the device begins to saturate to the power level of the spurious signals or system thermal-noise floor, whichever is greater. To meet the requirement

TABLE 5-1
CONVOLVER PARAMETERS

Parameter	Predicted	Measured
A_i	~ -1 dB	-2 ± 2 dB
C_i	-25 dB	-24 ± 4 dB
M	10 A/W	-
T_o	7.8 dB	-
MT_o	60 A/W	32 A/W
F	-38 dBm	-41 dBm

for higher output-power levels and spurious product suppression, a superconductive diode-ring structure is being developed. The maximum output power which can be obtained from an individual mixer is limited by the saturation of the tunneling nonlinearity as the RF potential impressed across the superconductive junction is increased about ~ 1 mV. Stacking a number N_j of SIS junctions in series can increase the input saturation power P_s by N_j^2 . A diode ring which has four individual junctions in each leg has been fabricated and tested; as expected, the ring increases P_s a nominal 12 dB. Equally as important, the balanced nature of the ring can be used to suppress undesired product terms which would contaminate the desired convolution output. These issues will be described in a later report dealing with an improved convolver of 2-GHz bandwidth.

S.A. Reible

REFERENCES

1. Solid State Research Report, Lincoln Laboratory M.I.T. (1981:2), p. 57, DTIC AD-A110947/9.
2. Ibid. (1982:2), p. 89, DTIC AD-A122252.
3. Ibid. (1982:3), p. 74.
4. S.A. Reible, A.C. Anderson, P.V. Wright, R.S. Withers, and R.W. Ralston, in 1982 Applied Superconductivity Conference Proceedings, IEEE Trans. Magn. (in press).
5. Solid State Research Report, Lincoln Laboratory, M.I.T. (1982:1), p. 93, DTIC AD-A118847.
6. E.L. Adler, in 1980 Ultrasonics Symposium Proceedings (IEEE, New York, 1980), p. 82, DTIC AD-A107060/6.

UNCLASSIFIED

SECURITY CLASSIFICATION OF THIS PAGE (When Data Entered)

REPORT DOCUMENTATION PAGE		READ INSTRUCTIONS BEFORE COMPLETING FORM
1. REPORT NUMBER ESD-TR-83-001	2. GOVT ACCESSION NO. AD-A128894	3. REPORT'S GAINING NUMBER
4. TITLE (and Subtitle) Solid State Research	5. TYPE OF REPORT & PERIOD COVERED Quarterly Technical Summary 1 November 1982 - 31 January 1983	6. PERFORMING ORG. REPORT NUMBER 1983:1
		7. CONTRACT OR GRANT NUMBER(s) F19628-80-C-0002
7. AUTHOR(s) Alan L. McWhorter	8. PERFORMING ORGANIZATION NAME AND ADDRESS Lincoln Laboratory, M.I.T. P.O. Box 73 Lexington, MA 02173-0073	9. PROGRAM ELEMENT, PROJECT, TASK AREA & WORK UNIT NUMBERS Program Element No. 63250F Project No. 649L
11. CONTROLLING OFFICE NAME AND ADDRESS Air Force Systems Command, USAF Andrews AFB Washington, DC 20331	12. REPORT DATE 15 February 1983	13. NUMBER OF PAGES 122
		15. SECURITY CLASS. (of this report) Unclassified
14. MONITORING AGENCY NAME & ADDRESS (if different from Controlling Office) Electronic Systems Division Hanscom AFB, MA 01731	16. DISTRIBUTION STATEMENT (of this Report) Approved for public release; distribution unlimited.	
17. DISTRIBUTION STATEMENT (of the abstract entered in Block 20, if different from Report)		
18. SUPPLEMENTARY NOTES None		
19. KEY WORDS (Continue on reverse side if necessary and identify by block number)		
solid state devices	photodiode devices	surface-wave transducers
quantum electronics	lasers	charge-coupled devices
materials research	imaging arrays	acoustoelectric devices
microelectronics	LIDAR system	waveguide structures
analog device technology		
20. ABSTRACT (Continue on reverse side if necessary and identify by block number)		
<p>This report covers in detail the solid state research work of the Solid State Division at Lincoln Laboratory for the period 1 November 1982 through 31 January 1983. The topics covered are Solid State Device Research, Quantum Electronics, Materials Research, Microelectronics, and Analog Device Technology. Funding is primarily provided by the Air Force, with additional support provided by the Army, DARPA, Navy, NASA, and DOE.</p>		

END

DATE
FILMED

6 - 83

DTIC